NASA TECHNICAL NOTE

NASA TN D-7964

ANALYTICAL AND EXPERIMENTAL
VIBRATION STUDIES OF A 1/8-SCALE
SHUTTLE ORBITER

Larry D. Pinson, Coordinator

Langley Research Center
Hampton, Va. 23665

1. Report No. NASA TN D-7964	2. Government Accession No.	3. Recipient's Catalog No.
4. Title and Subtitle ANALYTICAL AND EXPERIMENTAL VIBRATION STUDIES OF A 1/8-SCALE SHUTTLE ORBITER		5. Report Date December 1975
		6. Performing Organization Code
7. Author(s) Larry D. Pinson, Coordinator		8. Performing Organization Report No. L-9806
9. Performing Organization Name and Address NASA Langley Research Center Hampton, Va. 23665		10. Work Unit No. 506-17-32-01
		11. Contract or Grant No.
12. Sponsoring Agency Name and Address National Aeronautics and Space Administration Washington, D.C. 20546		13. Type of Report and Period Covered Technical Note
		14. Sponsoring Agency Code

15. Supplementary Notes

16. Abstract

Theoretical and experimental results for vibration of a 1/8-scale shuttle orbiter model are reported. Natural frequencies and mode shapes for four symmetric vibration modes and four antisymmetric modes are compared with predictions based on NASTRAN finite-element analyses. Initial predictions gave poor agreement with test data; an extensive investigation revealed that the major factors influencing agreement were out-of-plane imperfections in fuselage panels and a soft fin-fuselage connection. Computations with a more refined analysis indicated satisfactory frequency predictions for all modes studied, within 11 percent of experimental values.

17. Key Words (Suggested by Author(s)) Shuttle structural dynamics Vibration modes Scaled orbiter model Imperfect panels NASTRAN analyses	18. Distribution Statement Unclassified — Unlimited Subject Category 39

19. Security Classif. (of this report) Unclassified	20. Security Classif. (of this page) Unclassified	21. No. of Pages 150	22. Price* $5.75

CONTENTS

ANALYTICAL AND EXPERIMENTAL VIBRATION STUDIES
OF A 1/8-SCALE SHUTTLE ORBITER

Larry D. Pinson, Coordinator
Langley Research Center

SUMMARY

Theoretical and experimental results for vibration of a 1/8-scale shuttle orbiter model are reported. Natural frequencies and mode shapes for four symmetric vibration modes and four antisymmetric modes are compared with predictions based on NASTRAN finite-element analyses. Initial predictions gave poor agreement with test data; an intensive investigation revealed that the major factors influencing agreement were out-of-plane imperfections in fuselage panels and a soft fin-fuselage connection. Computations with a more refined analysis indicated satisfactory frequency predictions for all modes studied, within 11 percent of experimental values.

INTRODUCTION

Knowledge of the structural dynamic characteristics of launch vehicles is fundamental to the prediction of such dynamics problems as pogo, control, flutter stability, and the response to gusts and staging transients. Early in the development cycle, dynamic characteristics usually are defined by analysis, but verification by full-scale tests is not possible due to lack of prototype hardware. Confidence in analytical procedures may be established early in the design through the use of subscale structural models, and, in addition, full-scale dynamic behavior may be approximated through application of principles of similitude. The concept was developed by the NASA Langley Research Center (LRC) using a 1/5-scale model of the Saturn I vehicle (refs. 1 to 5) and was applied extensively in the development of a large Air Force launch system (refs. 6 to 8). Early data from a 1/10-scale replica model were used to improve analytical methods applicable to the Apollo/Saturn V launch vehicle (refs. 9 to 16) and to approximate full-scale behavior. The 1/10-scale Apollo/Saturn V model subsequently was used as a troubleshooting tool when anomalous behavior occurred in an early flight (ref. 17).

During the technology development phase, the space shuttle was recognized as having more complex structural dynamic characteristics than previous launch vehicles because four separate large elements are joined asymmetrically at a few discrete

interfaces. This multielement configuration will have high modal density at low frequencies, and the dynamic response will have a high degree of directional coupling. Thus, early verification of the ability to analyze adequately the various vehicle elements and subsequently to couple the element characteristics for prediction of total vehicle characteristics is of great importance. In addition, if confidence in this ability is sufficient, a reduction in full scale testing could be effected with consequent cost reduction. Studies of a greatly simplified multielement configuration are reported in references 18 and 19.

To provide a better assessment of analytical modeling procedures and data with which to understand the dynamic behavior of shuttlelike configurations, a 1/8-scale dynamic model of an early shuttle configuration was built for structural dynamics investigations at the Langley Research Center. Because of the lack of detailed definition at the time of construction, only overall dimensions were scaled according to principles of similitude. Stock sizes of materials were used to approximate varying thickness and nonstandard scaled dimensions. The model was designed by the Grumman Aerospace Corporation (GAC) under contract to LRC; subsequently, GAC built the solid rocket boosters and the external tank. The orbiter element was constructed at LRC.

The purpose of the present paper is to report the results of investigations of the vibration behavior of the 1/8-scale orbiter model. During initial vibration tests of the orbiter model, natural frequencies were found to be significantly different from those predicted by a preliminary NASTRAN finite-element model. For example, for the first mode the analytical natural frequency was 22 percent higher than the test natural frequency. Detailed studies of the orbiter were conducted to understand and reconcile these differences. The studies included free vibration tests, vibration tests under static preload, static-load deflection tests, and detailed analytical and experimental investigations of structural panels and joints. Results of the investigation are presented in this report.

The work reported herein was accomplished through a team effort consisting of several LRC, GAC, and Rockwell International Corporation (RIC) personnel. On-site support was provided by the Lyndon B. Johnson Space Center through RIC. Thus, various sections of this report have different authors and, where appropriate, the authorship is so designated. These authors are Leadbetter (LRC), Sewall (LRC), Blanchard (LRC), Flynn (GAC), Durling (LRC), Miller (GAC), Bernstein (GAC), Housner (LRC), Stein (LRC), Barrett (RIC), Herr (LRC), and Robinson (LRC). In addition, off-site analytical support was provided by Philip W. Mason, J. Zalesak, and H. G. Harris of GAC.

2

SYMBOLS AND ABBREVIATIONS

Measurements and calculations were made in the U.S. Customary Units. They are presented herein in the International System of Units (SI) with the equivalent values given parenthetically in the U.S. Customary Units. The following symbols apply to all parts of the report except appendix D, which has its own list of symbols.

A effective skin area (see eq. (E13))

A_B, A_C, A_T effective skin areas in direct stress for fuselage along bottom of sidewall, orbiter center line, and top of sidewall, respectively (see sketch (E1))

A_p cross-sectional area of cabin-to-payload bay splice plate (see eq. (C16))

A_1, A_2, A_3, A_4 cross-sectional areas of fuselage longerons in sketch (E1)

A_1, A_2 cross-sectional areas of wing-spar caps in sketch (E3)

a moment arm for simulated fin-root joint flexibility (see eqs. (C8))

B, C, D half-width of fuselage, keel height, and height of fuselage sidewall, respectively (see sketch (E1))

b fin-root width (see sketch (C4))

b_p length of cabin-to-payload bay lower splice plate (appendix C)

c/c_{cr} damping coefficient (see table II)

E Young's modulus

f circular frequency, $\omega/2\pi$, Hz

G shear modulus

h fin height (see sketch (C4))

I_A flexural moment of inertia of fuselage or wing cross section about neutral surface based on initial analysis (see eq. (E2))

$I_{A,X}$ total area moment of inertia of wing cross section about neutral surface (parallel to xy-plane) of wing (see eq. (E10))

I_F area moment of inertia of fin-fuselage spar clip about its cross-sectional neutral axis (see appendix C)

I_X required area moment of inertia of wing cross section about neutral surface (parallel to xy-plane) for analytical model revised by static test data (see eq. (E10) and sketch (E3))

I_Y required area moment of inertia in pitch of fuselage about neutral axis for analytical model revised by static test data (see eq. (E5) and sketch (E1))

I_Z required area moment of inertia in yaw of fuselage about vertical axis through orbiter center line for analytical model revised by static test data (see eq. (E6) and sketch (E1))

I_c area moment of inertia of wing spar caps about neutral surface (parallel to xy-plane) of wing cross section (see eq. (E11))

I_p area moment of inertia of cabin-to-payload bay splice plate about its cross-sectional neutral axis (see eq. (C17))

I_s area moment of inertia of reduced skin for wing (see eq. (E11))

$[K]$ stiffness matrix (see eqs. (1) and (2))

$K_{F1}, K_{F2}, K_{F3},$ spring constants representing fin-root stiffness (see fig. 24
$K_{F1,F}, K_{F1,A}$ and appendix C)

K_u, K_l spring constants representing cabin-to-payload bay joint stiffness (see fig. 25 and eqs. (C20) and (C21))

l_1, l_2 spar-clip length and splice-plate length, respectively (see sketch (C2))

$[M]$ mass matrix (see eq. (1))

4

M_1, M_2 bending moments in fin-root spar clip (see eqs. (C1) to (C4))

P   load

$\{P\}$ load vector (see eq. (2))

R   reaction (see sketch (C2))

t_l, t_s, t_u skin thicknesses of lower cover panels, fuselage sidewall, and wing upper cover panels, respectively (see table XVII) and sketch (E3))

U   strain energy defined by equation (C1)

$\{u\}$ displacement vector (see eqs. (1) and (2))

W   total effective skin width, $\sum w_i$ (see eq. (E12))

W_F full skin width (see sketch (E3))

w_i effective skin width in direct stress for ith spar cap (see sketch (E3))

w_o displacement at center of panel (see appendix E)

X, Y, Z   Cartesian coordinates

x_1, x_2 axial coordinates in fin-root joint analysis (see sketch (C2))

z_l, z_u vertical distances between wing neutral surface and midplanes of lower and upper covers of wing, respectively (see sketch (E3))

$\bar{z}$ vertical distance from bottom of fuselage to neutral axis (see eq. (E4))

α angle between spar-clip plates or splice plates (see sketch (C2))

β supplement to α for splice plates (see sketch (C5))

$\Delta = \delta_{e,s} - \delta_{a,s}$

δ static deflection

δ_A maximum static deflection from original analysis (see eq. (E2))

δ_T maximum static test deflection (see eq. (E2))

$\delta_{a,s}, \delta_{e,s}$ analytical and measured fin fore-and-aft static deflections (see sketch (C3))

ϵ strain due to static loading (see figs. 17 and 18)

λ eigenvalue (see eq. (1))

$\{\phi\}$ eigenvector (or mode shape)

ω angular frequency, $2\pi f$, radius per second

Subscripts:

dyn   dynamic (see fig. 24)

m   model (see table I)

p   prototype (see table I)

Abbreviations:

RS1   rod-shear panel model with fuselage and wing carry-through skins 33-percent effective in direct stress, fully effective in shear; fully effective wing skins; joint flexibilities in fin root (model F1, fig. 24) and cabin-to payload bay joint (fig. 25)

RS2   rod-shear panel model with fuselage and wing carry-through skins 46-percent effective in direct stress; wing skins 80-percent effective in direct stress; all skins fully effective in shear; same joint flexibilities as RS1

RS3   rod-shear panel model with wing skin 80-percent effective in direct stress and shear; original fuselage (i.e., fully effective skins) and original joints

6

RS4   rod-shear panel model of same direct-stress effectiveness as RS2 with fuse-
            lage skins 46-percent and wing skins 80-percent effective in shear, model F2
            fin-root joint flexibility, and same cabin-to-payload bay joint flexibility

RS5   rod-shear panel model same as RS4 with both fuselage and wing skins
            80-percent effective in shear

RS6   rod-shear panel model same as model II of reference 21

RM1   reduced-membrane model with all exterior fuselage and wing skins
            60-percent effective in direct stress and shear with same joint flexi-
            bilities as in RS4 and RS5 except for model F3 fin-root joint flexibility
            replacing F2 in the antisymmetric model

RM2   reduced-membrane model same as RM1 with membrane panels in door,
            also 60-percent effective in direct stress and shear

F1,F2,F3   fin-fuselage interface models shown in figure 24

GAC   Grumman Aerospace Corporation

LRC   Langley Research Center

NASA   National Aeronautics and Space Administration

RIC   Rockwell International Corporation

CPB   cabin-to-payload bay

CPU   central processing unit

MPC   multiple-point constraints

OPS   orbiting propulsion system

SPC   single-point constraints

TPS   thermal protection system

S.S.   simply supported (see fig. 50)

ORBITER TEST MODEL

Sumner A. Leadbetter and Ulysse J. Blanchard

This section presents results of vibration tests of the orbiter element of the 1/8-scale space shuttle dynamic model. The tests were conducted to provide data for the verification of the NASTRAN finite-element representation of the subscale orbiter model. A description of the experimental model, description of apparatus and procedures used to conduct tests, and a discussion of results are presented.

Model Description

The general arrangement of the 1/8-scale shuttle model is shown in figure 1. The design was based on a GAC configuration developed in the space shuttle studies for NASA in 1972. The parallel-burn configuration had a gross lift-off weight of 21.35 MN $(4.8 \times 10^6$ lb) and was 55.5 m (182 ft) long. The complete model consists of four major elements: the orbiter, external tank, and two solid rocket boosters. The orbiter model, which was constructed at LRC and is the subject of the present investigation, is shown in figure 2 without the cargo-bay door and in figure 3 with the door installed. Figure 4 is a drawing of the general arrangement of the orbiter model, and figure 5 shows the fuselage under construction. The orbiter model is primarily a riveted 2024-aluminum structure consisting of thin nontapered skins over supporting frames and longerons and with minimum use of intermediate skin stiffeners. The bottom and sides of the fuselage are flat, as are surfaces of the fin stub and wing. In simplifying the design, a major objective was to keep the model fabrication cost within target while retaining as many of the significant structural dynamic characteristics as possible. Hence, only the general characteristics of the major orbiter components were simulated. No attempt was made to model local details. A more detailed description of the model is presented in references 20 and 21.

Scaling.- The scaling relationships that must exist between the model and the prototype are shown in table I, and they are based upon the determination of the major factors, presented in reference 22, which influence the response of the prototype being studied. These relationships follow directly from a dimensional analysis of the various parameters that influence the dynamic behavior of the structure and from the choice of the model material. Extrapolating prototype behavior from model test data is accomplished by directly using these scaling relationships. It should be noted, however, that because of design expediency some of the scaling rules have been compromised. For example, the local skin stiffness on the model is less than the required scaled value of the prototype for preventing buckling. Some liberty has also been taken in modeling the stiffness characteristics by some necessary lumping in order to avoid the large expense of exact

scaling of very small dimensions. If local stiffeners (e.g., stringers) are completely eliminated, then the local stiffness of the skin is not duplicated and premature buckling will occur.

While accurate modeling of the prototype was desirable for extrapolating basic shuttlelike dynamic behavior, a prime object of the study was the correlation of a NASTRAN dynamic analysis with model test data. A complete static and dynamic analysis was made using NASTRAN with the structure modeled to a degree of refinement considered sufficient for preliminary design purposes. Thus, the need for direct scaling of the prototype design to obtain an exact model in every detail was not considered to be crucial. Also, the shuttle design was still in a state of flux at the beginning of this study; hence, any attempt to model the then current vehicle exactly would not be greatly beneficial to the shuttle project.

Fuselage.- The fuselage is 3.543 m (11.625 ft) long, contains 21 frame stations, and is constructed of 2024 aluminum. The bottom skin of the fuselage is 0.635 mm (0.025 in.) thick, and the sidewall and top skins are 0.508 mm (0.020 in.) thick. The fuselage frames in the region of the cargo bay (fig. 5) are constructed of aluminum sheet that has been bent to form channel sections. The tapered sidewall channel section and the lower portion are attached back-to-back to form a U-shaped frame. The major bulkheads located in the forward and aft sections of the fuselage are of stiffened sheet construction.

Fin.- The model fin structure, which represents only the structure from the fuselage to the center of gravity of the orbiter fin, contains three spars and a closure rib at the tip. The webs are 0.8128 mm (0.032 in.) thick while the covers are 0.5080 mm (0.020 in.) thick. During tests, a 26.69-N (6-lb) ballast weight representing the remaining fin structural weight was attached to the tip closure rib (location indicated in fig. 2). The fin structure is riveted onto the fuselage structure. Simple center-line clips connect the fore and aft fin spars to fuselage frames, and the center fin spar is connected by a clip and gusset combination at each side of the fin.

Cargo-bay door.- The fuselage cargo-bay door (fig. 3) is comprised of seven segments of 0.4064-mm (0.016-in.) aluminum sheet attached to semicircular frames to form a semicylindrical shell. The design of the eight door frames (V-shaped angles) allows expansion in the longitudinal direction, thereby offering little resistance to fuselage bending but allowing the fuselage-door combination to resist torsion. When attached to the fuselage, the model door simulates structural properties of a prototype door in a closed and locked position. The door has four keystone-shaped straps riveted to each side longeron which connect to the fuselage upper longeron by means of a single screw fastener each, as shown in figure 6. Five fasteners attach the door skin to the fuselage at each end of the door.

Wings.- The delta wings shown under construction in figure 7 consist of six spars and four ribs that are formed from 0.8128-mm (0.032-in.) 2024 aluminum sheet. The covers are 0.508 mm (0.020 in.) thick. The proper scaled wing weight, including items such as thermal protection system (TPS) panels and landing gear, is simulated by ballast installations shown in the figure.

Ballast.- Locations of other concentrated mass representations are indicated in figure 2. These masses include the orbiting propulsion system (OPS) ballast attachment, the crew-cabin area ballast, and the cargo-bay payload ballast. The payload simulation shown in figure 2 is representative of an intermediate-sized cargo; however, the present vibration investigation was conducted using a maximum payload simulation unit which extends the entire length of the cargo bay and represents a prototype weight of 289 kN (65 000 lb). The model payload is a box beam with brackets simulating orbiter payload attachment points. Appropriate ballast is attached to the beam to provide desired scaled payload mass.

Apparatus and Test Procedure

Suspension system.- The orbiter model was suspended in an inverted horizontal attitude during most of the vibration tests, as shown in figure 8. Steel cables with in-line soft coil springs were attached at the two fuselage interstage fittings and provided essentially free-free constraints. Rigid-body natural frequencies on this suspension system (f < 1.0 Hz) were much lower than the lowest structural frequency (f = 43 Hz) for all tests. Symmetric and antisymmetric resonances were excited by applying appropriate shaker forces, as shown in figure 8, for example.

Limited vibration tests also were conducted with the model suspended vertically as illustrated by the sketch in figure 9. During these tests, tension loads were applied to the model fuselage by means of a shock cord arrangement attached to the lower surface skin and the two lower main engine fittings. This test setup was used to study the effect of fuselage-panel stresses on resonant frequencies. The model was excited in the z-direction, xz-plane, while under various tension preloads ranging from 0 to 2670 N (600 lb).

Instrumentation.- The instrumentation of the 1/8-scale orbiter model was designed to provide continuous electronic signals to define the dynamic response of the model to sinusoidal force inputs. The instrumentation provided a means of monitoring exciter force inputs and transducer (acceleration) output signals, recording these signals for subsequent in-depth analysis, and performing on-site data analysis. The locations of fixed transducers, piezoelectric accelerometers, are shown in figure 10. In general, the accelerometers were mounted at the lower corners of the fuselage frames (stations), at available stiff locations such as the juncture of wing spars and ribs, and on ballast

10

masses. At all fuselage instrument locations, at least two accelerometers were mounted with one having its sensitive axis oriented parallel to the Z-axis (normal) and the other parallel to the Y-axis (lateral). At selected stations, a third accelerometer was oriented in the X-axis (longitudinal) direction. On the wings, all accelerometers were alined with the Z-axis. Whenever supplementary data were required, additional measurements were made with a vacuum-mounted movable accelerometer or by installing additional transducers in particular areas and on specific substructures. Strain gages were installed on selected skin panels of the fuselage midsection (sidewalls and bottom) and on the cargo-bay and cargo-door longerons (see fig. 6) in order to monitor panel stress conditions during longitudinal preload tests. The gages were mounted on opposite sides of the skin and near the center of the panel of interest. Each gage of the back-to-back pair was electronically independent of the other. Strain gages were mounted only on the outboard flanges of the longerons.

Data acquisition system.- A schematic of the data acquisition system is shown in figure 11. Data signal cables from the transducers were connected to data group switches in prearranged combinations so that a group of 14 selected channels of information could be monitored or recorded simultaneously. Four data channels were common to all groups: the force-gage output, input acceleration (exciter), oscillator (reference) output, and time code. The data were also recorded on analog tape for subsequent data reduction. The group of instruments designated "On-site analysis" permitted preliminary, quick-look evaluation of either real-time or tape-recorded data signals.

Test procedure.- The experimental data were obtained in basically the same manner for all test conditions. The input-force exciter supplied a constant-amplitude sinusoidal force to the model at slowly increasing frequency. Selected transducer outputs were plotted as diagrams of response amplitude and frequency (unfiltered). These signals were also simultaneously displayed as Lissajous patterns of force relative to acceleration on an oscilloscope, and peak response frequencies and phase shifts were noted. Examination of several diagrams of response amplitude relative to frequency served to identify individual peak response frequencies, which were then examined by manually tuning the frequency of excitation to obtain peak amplitude, dwelling at that frequency, and recording the output of all transducers. Apparent modes were also examined more closely by using the Kennedy-Pancu method described in reference 23 in order to reveal the existence of proximate resonant frequencies and modes. Damping values were calculated by using the phase-change method outlined by Mead in reference 24.

Description and results of subsequent static-load deflection measurements of the 1/8-scale orbiter model are presented in appendix A. These extensive load tests were conducted to evaluate the flexibility of various substructures and areas of the model

and to provide flexibility influence coefficients for guiding revisions to analytical representations which are also discussed subsequently.

Test Results and Discussion

The measured natural frequencies in the vertical (±Z) direction of seven responses and lateral (±Y) direction of three responses obtained during vibration tests in the low frequency range are listed in table II along with frequencies obtained with the initial finite-element analysis (ref. 21). A description of each of the identified modes and the damping coefficient obtained for the first mode are included. Initially, wing first bending (symmetric mode 2) appeared to be at a different frequency for the left and right wing components. Subsequent investigation indicated that local responses of wing skin panels were masking the response of primary structure and causing each wing component to respond differently, due to asymmetries in skin panel conditions. Lightweight angle stiffeners were attached diagonally across all rectangular panels (44) between ribs and spars to suppress only local skin responses, thereby permitting the identification of the normal-mode frequencies which were then found to be nearly coincident. The added stiffener weight was 2.4 percent of the original wing weight.

The resonant frequencies obtained from the initial NASTRAN finite-element model were in considerable disagreement with experimental frequencies for all the modes (up to 46 percent). Generally, the mode-shape characteristics were similar, as shown by comparison of the first four symmetric modes in figures 12, 13, 14, and 15. These results indicated that perhaps the experimental model was more flexible than the initial analytical representation, that mass distributions were improperly represented analytically, or that a combination of these existed. There were many possible sources of additional flexibility in the physical model such as weak structural joints, soft connections between major substructures or masses (e.g., payload simulation) and supporting structure, and model design characteristics such as large-aspect-ratio panels and lack of panel stiffening. The investigation of these problems is reported in the section comparing analytical and experimental results.

Results of vibration tests with tension preloads applied to the fuselage are shown in table III. With increase of load to 2670 N (600 lb), there was a small increase in first-mode frequency for the experimental model. The results suggested that the fuselage skin panels, which were observed to have out-of-plane deflections, were not fully loaded and hence had reduced stiffness in the model. This possibility was verified by strain-gage static data obtained during these preload tests and shown in figures 16 and 17. The variation of strain with longitudinal tension load for three typical skin panels is shown in figure 16. As applied load increases, the strain increases on both the inside and outside (opposite) gages of each skin panel. However, the level of strain is different on

12

each side of each panel, which indicates that the skin of the panel is bending and therefore is not fully effective. The differences in strain are quite large except for the left-hand sidewall panel. Similar results were obtained from all of the seven panels instrumented.

Figure 17 presents the data obtained from the strain gages on the fuselage cargo-bay longerons and the corresponding cargo-door longerons on both sides of the model. The differences in strain between door and fuselage longerons throughout the loading range indicate that the load paths are not those intended by design. The door longerons are not as effective as the fuselage longerons. The door attachment fittings to the fuselage were suspect in this case.

Other preliminary test parameter variations were conducted to explore and identify suspected flexibility anomalies between the experimental and finite-element models. These included the following brief vibration tests: (1) with and without the cargo-bay door, (2) with modified experimental boundary conditions at the payload simulation beam aft connection to the fuselage, (3) with an increased number of wing-to-fuselage attachment fasteners (doubled), and (4) with and without the fin ballast. The first three variations resulted in little or no change of the first-mode frequency. However, removal of the fin ballast increased the first-mode frequency from about 43 to 48 Hz. The amplitude of longitudinal motion at various elevations along the aft fin-fuselage surface is plotted in figure 18 for the ballast-on and ballast-off conditions. In both cases there is an abrupt change in magnitude of motion at the point of fin attachment to the fuselage. Fin motion relative to the fuselage is large, which indicated considerable flexibility in this model joint. These brief tests indicated that the disagreement in model frequencies between experiment and analysis was due to greater flexibility of the physical model. Probable sources of reduced stiffness in the physical model were initial out-of-plane imperfections in skin panels and several suspected structural joints (tail-fuselage and forward cabin-cargo bay junctures were prime suspects). Because of the anticipated cost in time of modifying the experimental model and the lack of data needed to positively ascertain the major problem areas, as well as the extent of their contribution to the overall correlation problem, it was decided that the analytical model should be revised to more accurately represent the existing test structure. The following sections and appendixes present discussions and results of both experimental and analytical work conducted to achieve better agreement.

ANALYTICAL MODELS

John L. Sewall

The analytical representation of the 1/8-scale orbiter vibration model is a finite-element model sufficiently detailed to reproduce overall dynamic behavior. No deliberate

effort has been made to simulate local motions, such as panel vibrations. The following sections contain brief descriptions of the analytical model, the solution procedure, and some experience in its application. The analytical results are compared with experimental vibration data for the physical model in the concluding section. Further information and related peripheral studies are detailed in appendixes B to E.

The finite-element analysis used for this model is the NASTRAN Level 15.5 system. Development of the analytical model is based on reference 25 and is fully detailed in references 21 and 26.

NASTRAN Model

The analytical orbiter model is made up of five substructures as shown in figure 19. Four substructures — fuselage, wing, door, and fin — appear in figure 19(a) and are each represented by combinations of panel, beam, rod, and concentrated-mass elements. The fifth substructure — payload — is simulated by an eight-element beam and concentrated masses located along the orbiter center line as shown in figure 19(b). Most of the external surfaces are modeled by membrane elements, which allow in-plane deformations in tension, compression, and in-plane shear. Membrane elements are also used for the forward cabin ballast, forward keel, and the top cover of the wing carry-through structure (see fig. 19(a)). Some panels in the cargo-door surface are modeled by plate elements, which allow both in-plane and out-of-plane (or bending) deformations. Longitudinal and bending stresses are carried by beam elements along the fuselage-door interface. Longitudinal stresses along the fuselage center line and lower outer edge are carried by rod elements. Rod elements are also used, along with shear panels, to model the main keel, ribs, and spars in the wing and fin, the aft-engine support structure, the accordionlike door frames, and the fuselage cross-sectional frames. The door-frame simulation is shown in figure 19(a) and is intended to prevent transmission of longitudinal stresses through the door surface. Typical fuselage frames are shown in figure 20 for the cabin area, payload bay, and engine-support area.

Solution Strategy

The analytical natural frequencies and mode shapes were calculated by solution of the general eigenvalue equation

$$\left([K] - \lambda [M] \right) \{u\} = \{0\} \tag{1}$$

where $[K]$ is the stiffness matrix, $[M]$ is the mass matrix, λ is the eigenvalue, and $\{u\}$ is the displacement vector, from which the eigenvectors are obtained. The mode shape (or eigenvector) $\{\phi_i\}$ is a set of relative, or normalized, displacements.

In this investigation, the mode shape was normalized to the maximum relative dynamic displacement in the structure (i.e., $\phi_i = u_i/u_{max}$ for every point i of a given mode). The sizes of $\begin{bmatrix} K \end{bmatrix}$ and $\begin{bmatrix} M \end{bmatrix}$ are governed by the number of unconstrained degrees of freedom at grid points in the structure.

The large number of degrees of freedom associated with the grid selected to represent the entire orbiter-model structure precluded a solution of equation (1) in a single NASTRAN computer execution on the NASA Langley Research Center CDC computer. Instead, the complete analytical model was divided into five major substructures as shown in figure 19. An adaptation of the current operational substructuring procedure was used, as described in reference 26. The adapted substructuring procedure detailed in reference 26 is contained in a single computer-program alteration in each phase of the calculation.

As indicated in the simplified block diagram of figure 21, there are four sequential operations involved. In phase I of the calculation, stiffness and mass matrices are generated for each substructure and stored on tapes. This information is then recopied onto a single tape in the so-called tape-copy operation and is used in phase II to generate the natural frequencies and mode shapes of the assembled orbiter. Phase II is designated "pseudo-structure" because its grid network includes only enough of the complete orbiter network to properly define structural dynamic behavior of the interfaces between substructures and overall orbiter mode shapes. More detailed mode-shape distributions could be obtained in phase III of the calculation, but this is an optional operation and was not executed in this investigation. Substructuring is discussed further in appendix B and in reference 21, vol. II, and reference 26, and the relation of substructuring to analytical modeling philosophy is also discussed in references 21 and 26.

Operational Experience

As is evident in figure 21, a single calculation of orbiter frequencies and mode shapes by the substructuring procedure requires a total of seven separate computer executions (or runs), not including phase III. A measure of the size of each run is given by the typical central processing unit (CPU) time indicated in the figure for carrying out the eigenvalue analysis on the NASA Langley Research Center CDC-6600 series computers. The phase I fuselage and phase II orbiter runs used the most CPU time and required CDC 6600 machines with nearly all the available storage capacity (i.e., field length). A more complete listing of computer requirements is given in table IV. The phase II runs required a field length of 300 000 octal words. The other runs required less time and field length, and the smallest ones (tape copy and Phase I payload) could be processed on the CDC 6400 with small amounts of CPU time. The number of runs gives an indication of the scope of the investigation into factors affecting the correlation between analysis and experiment. More variations in parameters were made for the

analytical symmetric model than for the antisymmetric model. The cumulative CPU time of seven runs, resulting in an orbiter phase II run, was 7915 sec, as shown in figure 21.

Another measure of size in the calculated procedure is evident in the numbers of elements, grid points, and degrees of freedom listed in table V, which is taken from table 2 of reference 21, vol. I. The most numerous elements are rods, membranes, and shear panels − in that order. The maximum matrix size in equation (1) for any substructure or for the entire orbiter may be estimated by simply multiplying the number of grid points by the maximum number of degrees of freedom possible at each grid; this maximum number is six, three displacements and three rotations. For example, the phase I fuselage can have at most 3222 degrees of freedom, and the phase II orbiter can have a maximum of 5604 degrees of freedom. However, the imposition of constraints results in a reduced number of degrees of freedom. In NASTRAN, the constraints are of two kinds: (1) single point constraints (SPC) restricting certain degrees of freedom at grid points so as to satisfy boundary conditions and symmetric or antisymmetric conditions, and (2) multipoint constraints (MPC) relating motions between different parts of the structure, thereby altering the number of independent degrees of freedom. The numbers of degrees of freedom remaining in the present investigation after imposing SPC and MPC are so indicated in table V. Because of model symmetry, certain SPC restrict motions to vertical, longitudinal, and pitch in the vertical plane of symmetry through the orbiter center line, and other SPC allow only lateral, roll, and yaw motions along this center line; hence, the two models, symmetric and antisymmetric. For the phase I fuselage and Phase II orbiter, the reduction in maximum matrix sizes is well over half. This is also true for the phase I wing and door, but for the phase I fin and payload, the reductions were about three to one.

Table V also indicates another substantial reduction in the number of degrees of freedom through application of the Guyan reduction (ref. 27). In the present investigation, selected degrees of freedom were reduced out by this procedure from all substructures except the phase I payload. For phase II, the reduction in degrees of freedom was not so great as for the individual substructures but did result in dynamic matrices of order 339. This problem required from 3900 to over 4000 sec of CPU time to obtain nine natural frequencies and mode shapes by the inverse power method on the Langley Research Center CDC 6600.

Without the substructuring procedure, the NASTRAN solution of equation (1) for the orbiter was intractable. With substructuring, the limits of present computer capability were closely approached for practicable operation in the present investigation. Priorities at the Langley computer complex were essential for reasonable turn-around times (e.g., overnight). Further aspects of the operational experience with the present 1/8-scale dynamic model are discussed in appendix B and in reference 21, vol. I.

Static Analysis

In conjunction with the static test program described in appendix A for the physical model, a NASTRAN analytical model was formulated to compute displacements due to static loading from the relation

$$[K]\{u\} = \{P\} \tag{2}$$

where $\{P\}$ is a vector of static discrete loads P_j located in various parts of the model. Solutions for the displacements $\{u\}$ were obtained with $P_j = 4.45$ N (1 lb). These calculations were performed in a single computer execution having as input a simple combination of all five substructures and involving no substructuring operations. Over 2400 degrees of freedom were involved, as indicated by the totals for the columns entitled "After SPC and MPC" in table V. Each of these calculations took about 2800 sec of CPU time and were run at 300 000 octal words of core. In an effort to gain as much as possible in computational efficiency, the NASTRAN grid point resequencing feature was used to give well-banded matrices (i.e., matrices each with nonzero elements clustered about the main diagonal). The SEQGP data cards required for this operation were generated automatically by means of the BANDIT computer program described in reference 28. Results checked satisfactorily with static deflections calculated at GAC using the orbiter phase II pseudostructure (ref. 21, vol. II). Other aspects of the operational experience with the 1/8-scale static model are discussed in appendix B and reference 21, vol. II.

ANALYTICAL RESULTS AND COMPARISON WITH EXPERIMENT

John L. Sewall

Unacceptable discrepancies revealed in initial comparisons between analytical and measured frequencies (table II) prompted an investigation resulting in the identification of significant structural joint and panel behavior not accounted for in the initial mathematical modeling. The investigation involved studies of the effects of various modifications to the NASTRAN model: first, as reported herein, second, in supporting studies in appendixes A, C, D, and E, and third, in reference 21. Primary emphasis is given to symmetric model conditions, although some results are included for the antisymmetric model. These studies led to various revisions in the analytical model, and the frequencies of the best of these models are compared in table VI with measured frequencies.

Initial and Side Investigations

The initial and side investigations are listed as follows (where the tabulation deals with items which were found to be of minor importance to the analytical-experimental correlation):

Fuselage . . . . Satisfactory agreement between NASTRAN and section bending stiffness (ref. 21, vol II)

Generalized mass estimates . . . . Fuselage and ballasts are largest contributors (ref. 21, vol. II)

Cabin ballast modeling . . . . Negligible effect of replacing membrane by plate elements

Wing carry-through modifications . . . . Negligible effects of reducing panel thickness to simulate cutouts and shear connections

Door longeron effectiveness . . . . Negligible dynamic effects of reduced door longeron cross-sectional area to account for more bending flexibility (appendix C)

Fin ballast support . . . . Uncertain effects of local distortions

Panel modeling accuracy . . . . Satisfactory accuracy of NASTRAN membrane panels (appendix D)

High panel aspect ratio . . . . Could cause as much as 5-percent increase in frequency (appendix D) and ref. 21)

None of the items in the foregoing listing revealed the major cause of the experimental-analytical frequency discrepancy, although they did lead to a better understanding of both the physical and analytical models. Further elaboration of these items follows.

Fuselage.- Satisfactory agreement was obtained for bending stiffnesses extracted from the NASTRAN generated stiffness matrix compared with bending stiffnesses deduced from a NASTRAN generated deflection curve and calculated from section geometry of the physical model.

Generalized mass estimates.- Generalized mass estimates based on the first symmetric mode helped to identify areas of the model requiring further investigation.

18

Dominant portions of the generalized mass existed in the fin ballast, the orbiting propulsion system (OPS) ballast, cabin ballast, the remainder of the fuselage, and the wing.

Cabin ballast remodeling.- Negligible reductions in analytical frequencies were obtained by allowing more degrees of freedom in the cabin ballast and by attempting to simulate effective stiffnesses in the wing carry-through structure and door longeron. The ballast was in the form of a thick (0.95 cm (3/8 in.)) plate attached to the cabin structure, and its presence could conceivably change stiffnesses in this area. Replacing membrane elements with plate elements in the cabin ballast simply allowed additional pitch and roll degrees of freedom not permitted with the membranes.

Wing carry-through modifications.- Views of the wing carry-through structure including pertinent interface details are shown in figure 22. Figure 22(a) is an overall view of the four main wing-fuselage connections. Figure 22(b) is a closeup of the connection at fuselage station 144.75 and shows the cutout in the top-cover panel for the fuselage frame and also the vertical channel member to which the wing-fuselage shear pin connection is attached. Membrane panel thicknesses in the top cover of the NASTRAN model (fig. 19(a)) adjacent to the wing-fuselage interface were reduced to account for a possible loss in wing bending stiffness due to the cutouts. In the initial NASTRAN model, the thickness of each vertical shear panel in the wing root shear connection was arbitrarily chosen to be the same as the channel thickness (fig. 22(b)). In the present investigation, this thickness was reduced according to the cross-sectional area of the shear pin to approximate a more realistic shear flow between wing and fuselage.

Door longeron effectiveness.- A typical door-to-door fuselage longeron attachment is the door clip shown in figure 6, and there are four of these nearly equally spaced along the cargo bay. Longitudinal loads transmitted by shear pins through the clips from the fuselage longeron to the door longeron will result in a combined longitudinal and rotational (pitch) deformation of the door longeron. However, the bending flexibility in the door longeron due to this rotation had not been considered in the initial NASTRAN model. When it was considered, as shown in appendix C, the cross-sectional area of the door longeron was approximately halved to account for a reduced door longeron effectiveness.

Fin ballast support.- During vibration tests of the physical model, some local deflections of the fin-ballast support structure could be deduced from the vibration mode shape shown in figure 18. Attempts to reproduce these local motions by revisions to the analytical model involved refinements to the fin-ballast support structure as illustrated in sketches (a) and (b). These refinements consisted of a NASTRAN model of the channel-shaped support structure and alternative ways of connecting it to the fin ballast. In the initial model, the motions of the fin ballast were simply linked by MPC
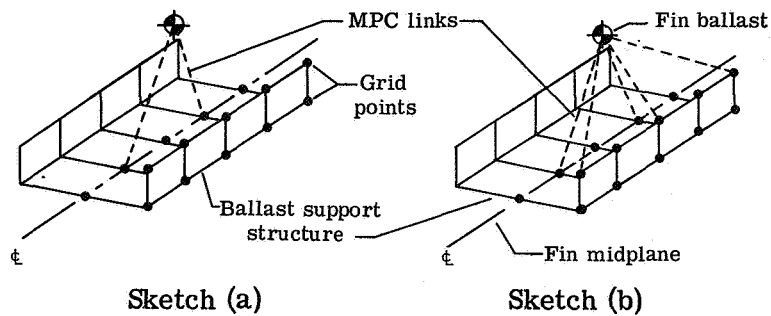
Sketch (a)   Sketch (b)

relations to the motions of the grid network of the fin-tip rib. Sketch (a) indicates one
model revision in which the MPC links are confined to two points along the midplane of
the fin. Two variations of this model resulted in drastic reductions in the phase I fin
frequencies and unrealistic mode-shape distortions along the fin-tip midplane. The other
revised model in sketch (b) allowed for additional MPC links, as indicated, to three points
along the channel flange but resulted in negligible phase I frequency reductions and mode-
shape changes compared with those of the initial model. Consequently, modifications to
the initial ballast support structure model were considered unwarranted.

Panel modeling accuracy.- The capability of NASTRAN to predict accurately the
dynamic response of a fuselagelike structure was evaluated in a side investigation
reported in appendix D. Frequencies, mode shapes, and dynamic shear stresses of
NASTRAN analyses of a simplified model of the cargo bay agree well with those obtained
in two closed-form solutions.

High panel aspect ratio.- As is evident in figure 19(a), many of the analytical mem-
brane panels in the fuselage sidewalls and bottom are long and narrow and, therefore,
possibly have too much in-plane stiffness. This characteristic is shown in reference 29
for in-plane load-displacement studies of NASTRAN quadrilateral plate elements. As
shown in reference 21, vol. II, and in appendix D, this high-aspect-ratio effect is esti-
mated to account for an approximately 10-percent increase in stiffness and thus an
approximate 5-percent increase in frequency for NASTRAN quadrilateral membrane
elements (QDMEM2).

Effects of Joints

The sensitivity of the model's vibration behavior to joint flexibility is indicated as
follows:

Fin-fuselage interface . . . . Accounted for about $13\frac{1}{2}$ percent of frequency
discrepancy (appendix C)

Cabin-cargo bay . . . . Negligible effect on frequency

Payload supports . . . . Small effect on lower mode frequencies
(ref. 21, vol. II)

20

As shown in appendix C, joint flexibility estimates were determined both by structural analysis of the actual connections in the physical model and by correlation of measured and calculated static deflections.

Fin-fuselage interface.- As shown in figure 23, the fin is attached to the fuselage at the front, center, and rear spars of the fin and by angle splices along the fin-fuselage junction. As previously described, the fin fore and aft spars are connected by metal clips (visible in fig. 23) to fuselage frames at the ends of the engine support structure, and the center fin spar is connected by a clip and a gusset (fig. 23(a)) to a fuselage frame in the middle of the engine support structure. In between these three fuselage frames, the fin-fuselage angle connection is fastened only to the skin without any underlying backup or support structure.

NASTRAN models of the fin-fuselage interface are shown in figure 24. In all cases, the actual connections were modeled by grid points along the fin center line and the outside edge, and the motions of both substructures were matched at these points. There were no springs in the initial NASTRAN model. Phase II orbiter initial analyses at GAC showed a 5-Hz frequency change due to altering boundary conditions of the forward fin-fuselage attachment and a negligible change due to altering the aft fin attachment (see ref. 26). In addition, deflections due to static loading measured along the fin trailing edge and aft end of the fuselage revealed considerable flexibility in the overall fin-root attachment not accounted for in the original NASTRAN model. This flexibility was modeled in different ways in terms of linear spring constants, as illustrated in figure 24. The $13\frac{1}{2}$-percent frequency discrepancy noted in the second of the foregoing tabulations applies to the first symmetric mode which was calculated with flexibility allowed in the forward fin attachments only (model F2, fig. 24) and based on the difference between measured and analytical static deflections, as shown in appendix C.

Cabin-cargo bay and payload supports.- Joint flexibilities were also investigated and simulated at the cabin-to-cargo bay juncture (appendix C), shown schematically in figure 25, and at the payload mounting points in the fuselage (see ref. 21, vol. II). Neither of these joints had as large an effect on fundamental frequency as the fin-root flexibility.

Panel Effectiveness

Panel load-carrying effectiveness is listed as follows (where the tabulation identifies the two types of modeling changes that accounted for the major part of the experimental-analytical frequency discrepancy, namely, partial effectiveness of exterior surface panels in transmitting inplane direct and shear stresses):

Rod-shear panel modifications . . . . Accounted for 53 percent to 80 percent of frequency discrepancy (appendix E and ref. 21, vol. II)

Reduced membrane-panel thicknesses . . . . Accounted for about 80 percent of frequency discrepancy (table VI)

In the first type of panel model, membrane elements were replaced by shear panels and bordered by rods. The second type of effective panel model was simply the membrane element with its thickness reduced according to criteria derived from independent studies described both in appendix E and reference 21. A thickness reduction in the membrane panel reduces direct and shear-stress effectiveness simultaneously, whereas these properties can be separately varied in the rod-shear panel model.

Rod-shear panel modifications.- As shown in appendix E, rod-shear panel modifications were made for the cargo-bay part of the fuselage and for top and bottom covers of the wing and wing carry-through structure. Sizing of rod cross-sectional areas to be effective in direct stress was based on correlation of orbiter measured and analytical static deflections, and the choice of shear-panel thickness was made independently, and arbitrarily, to represent partial effectiveness of the panels in shear. Six different models were investigated and are designated RS1 to RS6. The best rod-shear panel model is RS6, which is model II of reference 21. Results from this model are compared with those of the other rod-shear panel models in appendix E.

Reduced membrane panel thicknesses.- Reductions in membrane panel thicknesses were based on results of independent studies that included theoretical criteria based on reference 30 and tests and finite-element analyses of a simplified cantilever panel model approximately the same size as the cargo-bay sidewall (see also appendix E). In contrast to the rod-shear panel models, thickness reductions were made for all exterior surface membrane panels of the fuselage, wings, and the top cover panel of the wing carry-through structure. Further discussion of these modifications is also given in the following sections and in appendix E.

Symmetric Natural Frequencies and Mode Shapes

Symmetric natural frequencies showing the combined effects of joint flexibility and reduced panel effectiveness are listed in table VI(a) for the best analytical models. Measured frequencies are also included for the first four modes. Mode identifications are given in table II.

For the rod-shear panel model RS6, magnitudes of the reduced effectiveness in direct stress were obtained by application of the large-deflection equations for panel imperfections in reference 30 and amounted to 50 percent for the fuselage payload-bay region and 85 percent for the wing. The payload-bay panels were considered to be

two-thirds effective in transmitting shear and the wing panels were 85-percent effective. These values were chosen somewhat arbitrarily, and the choice of different values for fuselage and wing was influenced partly by different panel aspect ratios in wing and fuselage. Different joint flexibilities were used in reference 21 than in the models considered in the present paper, and additional flexibilities were introduced at the payload supports.

In the reduced membrane model RM1, a panel effectiveness of 60 percent was uniformly applied in both direct stress and shear to all exterior membranes of the fuselage and wings, including the wing carry-through cover panels. This value was based partly on the criteria used for model RS6 and partly on results of some simplified panel studies described in appendix E. Frequencies of the reduced membrane model are in close agreement with those of the rod-shear panel model RS6, and both sets of frequencies generally agree better with measured frequencies than do those of the other rod-shear panel models considered in this study.

Analytical symmetric mode shapes for model RM1 are compared with measured mode shapes in figures 26 to 29. In general, the agreement is about as good as that for the initial NASTRAN model in figures 12 to 15. Mode shapes of the wing and fuselage in the first mode are in somewhat better agreement for RM1 than for the initial model, but just the reverse is true for the payload and fin. Better agreement with experiment is also shown for RM1 in the outer wing for the third mode and in the fin for the fourth mode.

Antisymmetric Natural Frequencies and Mode Shapes

Analytical frequencies of the best antisymmetric models are included in table VI(b). Corresponding mode shapes are shown, together with experimental mode shapes, in figures 30 to 33. In addition to the 60-percent panel effectiveness in model RM1, joint flexibility is included for both the cabin-to-payload bay junction and for the fin-fuselage interface using a roll-spring model (F3 in fig. 24) similar to one derived in reference 21. The frequencies of the model are lower than those of the initial antisymmetric model by about the same amounts as those of the symmetric model; and the first antisymmetric frequency of model RM1 is in as good agreement with the measured first antisymmetric-mode frequency as are the symmetric-mode frequencies.

The fourth antisymmetric frequency (77.8 Hz in table VI(b)) is associated with a predominant roll (or torsional) response of the orbiter. Much of the torsional stiffness of this mode can be attributed to the closed doors of the orbiter. The presence of a low-frequency torsional mode in the phase I fuselage substructure listed in table VII(a) suggests the possibility of a low orbiter (phase II) torsion mode with the doors open, and this possibility is confirmed both by a phase II calculation with the doors off and by test, as shown in table VII(b) and figure 33. Modes 2 to 6 in table VII(b) correspond to modes 1

to 5 in table VI(b), and their frequencies are increased from 2.3 percent to 14.8 percent due to loss of door mass. A low-frequency torsion mode was also obtained for the highly simplified cargo-bay model of appendix D.

Experimental antisymmetric mode shapes with doors on are compared in figures 30 to 32 with corresponding analytical mode shapes for the first, second, and fifth modes. The agreement is generally good except for the large discrepancies evident in figures 30 and 32 for the lateral payload component. This disagreement may be due to inadequate analytical representations of payload stiffnesses and lateral flexibilities in the physical constraints at fuselage-payload interfaces. The boxlike structure of the payload beam is formed from two channels intermittently welded at the edges of their flanges in a series of discontinuous joints, each 5.34 cm (2.1 in.) in length, along the beam, with additional stiffness provided by plates attached to the vertical sides (or channel webs) of the box. Lateral bending and torsional stiffnesses of this beam for the analytical model are based on the assumption of continuous welds and may be too high. However, a realistic approximation of these stiffnesses is not readily available. Moreover, arbitrary reductions in stiffness have shown small reductions in phase II frequencies and negligible changes in the analytical payload lateral mode shape.

Another relatively minor mode-shape disagreement in the antisymmetric vibration modes exists along the door longeron. Here, in the range of about 93 to 105 Hz, the door longeron experienced numerous large lateral displacements that not only did not match the smoother overall deflections of the adjacent fuselage longeron, but also could not be reproduced in the present analysis. A closer analytical representation of these motions would require a finer grid network for the door, together with the allowance of a sufficient number of lateral degrees of freedom along the door longeron.

CONCLUDING REMARKS

Vibration tests and analysis of a 1/8-scale model of a preliminary design for a space shuttle orbiter have been reported. Test results for four symmetric vibration modes and four antisymmetric modes have been compared with finite-element predictions based on NASTRAN analyses. Initial analysis results using geometrically derived stiffnesses indicated poor agreement with test data.

An extensive analytical and experimental investigation of the structural response of the orbiter, consisting of parallel statics and vibration studies, revealed that the causes for the discrepancy were (1) out-of-plane initial imperfections of the panels in the fuselage (about 85-percent contribution) and (2) a soft connection between the model fin and fuselage (about 15-percent contribution). These characteristics of the physical model could not be defined prior to its construction. When these characteristics were

24

included in the mathematical model, satisfactory correlation was obtained; symmetric and antisymmetric frequencies could be predicted within 11 percent for the modes compared.

The conclusions from parallel studies contributing to this good correlation should be noted. The static test-analysis program was essential in determining realistic estimates of flexibility in various parts of the present structure where initial analytical predictions were overly stiff, such as in the fin-fuselage joint and the cargo-bay doors. Comparisons of analytical results for coarse and fine grid models of a simplified orbiter fuselage with closed-form solutions confirmed the NASTRAN accuracy in predicting natural frequencies and mode shapes of monocoque structures. This study also showed that the use of relatively high aspect ratio of the NASTRAN membrane elements does not result in a frequency increase of more than a few percent for the present structure. Analytical and experimental panel-effectiveness studies indicate that panels such as those forming the fuselage and wing skins are about 60-percent effective in carrying direct stress and in-plane shear over an aspect-ratio range of 0.5 to 2 and having initial out-of-plane imperfections of one fourth the skin thickness or greater.

The NASTRAN finite-element program is capable of satisfactorily predicting dynamic characteristics of structures similar to the space shuttle orbiter. However, even with the use of the substructuring capability of the program (in Level 15) and pitch-plane symmetry, a large structural dynamic mathematical model resulted which utilized most of the LRC computer storage capability and required long run times. Two and one-half hours were required on the CDC 6600 to obtain the lowest symmetric and antisymmetric modes (four each) after reduction of the assembled model (2500 degrees of freedom) by substructuring and Guyan elimination to 332 degrees of freedom. Thus, parametric studies may become time consuming and expensive.

Langley Research Center
National Aeronautics and Space Administration
Hampton, Va. 23665
July 21, 1975

APPENDIX A

STATIC-LOAD DEFLECTION MEASUREMENTS

Ulysse J. Blanchard and John E. Flynn*

Introduction

Initial experimental and analytical dynamic response data obtained for the 1/8-scale shuttle orbiter model showed a significant discrepancy in natural frequencies. Values obtained by analysis were higher than by experiment. The data also indicated that flexibility of the experimental model was greater than the originally formulated NASTRAN finite-element representation. It appeared that a combination of partially effective skin panels, due to deviations in flatness, and joint flexibilities could be contributors to the disagreement. Extensive static-load tests were conducted in order to evaluate the flexibility of various substructures and areas of the model and to provide flexibility influence coefficients for guiding revisions to analytical representations.

Apparatus and Procedure

The static-load tests were conducted with the model supported at interstage connection fittings. The photograph of figure 34 shows the model mounted on four pedestals which were attached to steel beams embedded in the concrete floor of the Langley structural dynamics research laboratory. Photographs of the orbiter interstage fittings and adapter brackets attached to the pedestals are shown in figures 35(a), 35(b), and 35(c). Support point constraints of the orbiter during static-load testing are illustrated in figure 36 and these essentially duplicate conditions for the orbiter mated to the external tank.

The points of application and the direction in which symmetric and antisymmetric loads were applied to the model are illustrated in figures 37(a) and 37(b). In all, 14 symmetric and 4 antisymmetric load conditions were investigated. Some of these conditions also were investigated with and without the cargo-bay doors. Incremental loads were applied with calibrated weights placed on various weight pans connected through cables to primary structural members. Some of these loading apparatus are shown in figures 34 and 38.

Dial indicators on support frames (figs. 38(a) and 38(b)) were used to measure deflections of the model resulting from the applied loads. The basic dial-indicator coverage of the model during the tests is illustrated in figure 39. Measurements were

---

*Grumman Aerospace Corporation.

made at points on the model having maximum stiffness such as the fuselage frames, longerons, juncture of wing spars and ribs, and ballast masses.

During the tests, several loading and readout procedures were employed to minimize error and to maintain acceptable data accuracy. As an example, consistency in the data was improved by cycling an intermediate load on and off the model several times prior to each test run. Early in the investigation a statistical check of measurement accuracy was made. Results are shown in table VIII. Nineteen on-off loads simultaneously applied at two weight pans at the nose of the model resulted in a 3-sigma deviation of about $12\frac{1}{2}$ percent from mean for deflection readings.

Results and Discussion

Typical load deflection data obtained during loading of the aft fuselage structure are shown in figure 40. Measurements obtained at the loading point, the fin tip, and the lower fuselage corner are shown for longitudinal loads applied to ballast masses representing the orbiting propulsion system (OPS). Data plotted above the zero-load line are for loads applied in the aft (+x) direction and the data below the line are for loads applied in the forward (-x) direction. As shown in the figures, straight line fairings of the data points were made whenever possible. Generally, the loading and unloading legs for each test run had to be treated separately due to various degrees of hysteresis. Also, the individual loading directions were faired separately since in most cases there was some nonlinearity going through zero load. The best data were consistently obtained in areas of maximum deflection such as the loading point. As distance of the measurement point from the load point increased or as total deflections decreased, the measurements became more erratic.

Slopes of the faired lines were determined and then averaged for each load application point. The values obtained are presented in table IX as measured flexibility coefficients at the load points. Also listed in the table for comparison are deflection coefficients calculated using the initial NASTRAN analysis (model I of ref. 21).

Concluding Remarks

In all test cases shown, the experimental model was more flexible than the original finite-element representation. The data for symmetric loading at midfuselage (bending) show that the experimental-model cargo door was less effective than predicted by analysis. This complements strain-gage data obtained during previous vibration tests (fig. 17). Also, a much larger flexibility in the experimental fin to fuselage joint is indicated by results for symmetric loading of the fin ballast. Another significant result is the greater-than-predicted torsional effectiveness of the experimental cargo door (antisymmetric nose loading case).

APPENDIX B

NASTRAN OPERATIONAL EXPERIENCE

Barbara J. Durling

This appendix presents various aspects of the operational experience with the CDC version of NASTRAN Level 15.5 during the dynamic and static analyses of the 1/8-scale shuttle orbiter model. The discussion records some of the user options selected and problems encountered and circumvented. In addition, several comments and suggestions are included to benefit the new or occasional user or programer of NASTRAN.

Substructuring

The analytical natural frequencies and mode shapes for the orbiter were obtained by coupling the five orbiter substructures in a substructure analysis procedure in the Normal Mode Analysis (Rigid Format 3) in NASTRAN. This procedure utilized an adapted DMAP (Direct Matrix Abstraction Program) alter packet in Rigid Format 3 and a DMAP tape copy program which were provided by the Grumman Aerospace Corporation (see refs. 21 and 26). The single alter packet is easier to use than the NASTRAN substructure analysis procedure described in section 1.10 of reference 25 which requires a separate alter packet for each phase of the substructuring process. Provisions for making equilibrium checks and for calculating substructure frequencies and mode shapes in phase I, either for the free-free boundary condition or with the substructure fixed at an interface and free elsewhere, are also included in this single alter packet. These additional features were particularly useful in the orbiter study to assess model changes.

The DMAP tape copy program was developed for this investigation under the rules of NASTRAN's DMAP (described in ref. 25) for creating special and analytical programs or routines within the NASTRAN system. This DMAP program is described in reference 26 and is executed in NASTRAN after the phase I executions have been completed (see fig. 21). It reads the stiffness and mass matrices from each of the tapes generated in the phase I runs and places these matrices on a single tape which will be read in the phase II execution.

During this analysis a coding error was discovered in the CDC version of NASTRAN Level 15.5 which precluded use of the INP9 user tape. This error was circumvented by changing INP9 to INP8 in the DMAP alter packet.

APPENDIX B

GINO Buffer Size

The GINO (General Input/Output) buffer is the storage reserved in open core for each GINO file opened. The default GINO buffer size in the CDC version of NASTRAN Level 15.5 is 666. When an increased buffer size is desired for CDC NASTRAN runs, it is recommended that multiples of 512 be added to the default buffer size. The increased buffer size used on some of the orbiter runs was 2202. It was obtained by inserting a NASTRAN card

NASTRAN BUFFSIZE = 2202, NLINES = 35

before the ID card (identification card which is the first card of the NASTRAN Executive deck) in the NASTRAN Data deck. The print control parameter modification was included so that only 35 lines of data would be printed on each page of 21.6-cm $\left(8\frac{1}{2}\text{-in.}\right)$ tabulating paper.

Buffer size on substructuring runs.- If an increased buffer size is required on any run in the sequence of runs for coupling the substructures, then all runs in the sequence must use the increased buffer size. This point is emphasized so that a new user will consider the need for an increased buffer size on phase II of the substructuring sequence before submitting phase I runs. (See fig. 21 and the section entitled "Solution Strategy" in the main body of this paper.)

Buffer size on the restarts.- It is mandatory that the GINO buffer size used on an initial checkpointed run be maintained on a subsequent run which utilizes as an Old Problem Tape (OPTP) any reel generated as a New Problem Tape (NPTP) on any run in the sequence of runs. Thus, either the default or modified GINO buffer size can be changed only by submitting an initial run for the configuration.

Working Core

NASTRAN efficiency should be maximized whenever possible. To achieve this end, sufficient working core must be allocated or excess core eliminated. In many applications, modules that perform symmetric matrix decompositions, such as RBMG2 and SMP1, require the largest amount of core. The core requirements for symmetric matrix decomposition are described in section 3.5.14 of reference 31 and also in section 2.2 of reference 32. The working core W required for single precision symmetric decomposition is given by equation (9) on page 2.2-4 in reference 32 as

$$W \geq BR - \frac{R^2}{2} + BC + \frac{C^2}{2} \qquad\qquad B \geq R \geq 2 \qquad\qquad (B1)$$

where B is the bandwidth, R is the number of columns of terms inside the band that will fit in core, and C is the number of active columns.

For efficient operation, sufficient core should be allocated so that a spill situation is avoided. The no-spill situation for symmetric decomposition is indicated from NASTRAN user information message 3023 (which prints values of B, C, and R) when R = B - 1. The working core W, as given in equation (B1), does not include the storage required for GINO buffers. As previously mentioned, space sufficient for three buffers is required when no spill occurs and space sufficient for five buffers is needed when spill occurs.

Diagnostics

Optional diagnostic output may be obtained by inserting DIAG cards in the NASTRAN Executive deck. The DIAG's used most frequently on the orbiter runs were 1, 8, 11, 13, 14, 15, 16, 19, 21, and 22. A description of the output triggered by these DIAG's is given in reference 25, page 2.2-4. Since the reason for selecting some of these DIAG's may not be apparent to the new NASTRAN user, brief comments will be given.

Open core length is printed in the dayfile (program chronology at the end of a computer printout on the CDC computers) when DIAG 13 is included. This information, used in conjunction with the location for the beginning of open core (see ref. 31, pp. 5.5-17 to 5.5-47), enables the user to determine more accurately the field length actually needed for the job.

Although included primarily so the systems programer can trace GINO OPEN/CLOSE operations, DIAG 15 can also serve the user. A significantly large number of these OPEN/CLOSE messages in the dayfile indicates that a larger field and/or an increased buffer size is needed for the job. When solving very large problems, these messages may be an indicator that solution of the given problem either is not feasible or perhaps, in the case of a job abort, is impossible due to excessively long run times or insufficient core on a given computer. It may be necessary to remodel part or all of the structure in order to reduce the number of degrees of freedom allowed and still maintain adequate representation of the structure.

Run times can be estimated more accurately for subsequent submittals by checking execution times for modules. These times can be computed from the BEGIN and END times printed in the dayfile for each functional module. Tabulations and plots of these run times against problem size for selected modules were useful in the present analysis.

Grid-Point Resequencing

A large percentage of the total computing time for structural analysis in NASTRAN is associated with triangular decompositions. The decomposition routines treat all

matrices as partially banded, that is, nonzero terms clustered near the diagonal are treated inside a band of constant width, and nonzero terms outside the band are treated separately and referred to as active columns. Since the structural matrices formed in NASTRAN are both symmetric and sparse, computational efficiency can be obtained best when using the displacement method by selecting the numbers assigned to grid points in such a manner that stiffness matrices will be created with relatively narrow bands. (See ref. 25, section 1.2.2. and ref. 32, section 2.2.)

External grid-point numbers may be selected in a convenient manner and then a NASTRAN option may be used to resequence the external grid points internally. This option is activated by the presence of a set of SEQGP cards in the Bulk Data deck. These cards provide the correspondence between the external grid-point numbers for the model and the internal grid-point numbers that will be used in the calculations.

Since selection of the internal grid-point numbers for optimizing the bandwidth can be difficult and time consuming, programs for automatically generating the SEQGP cards have been developed. The BANDIT computer program described in reference 28 was used to generate the SEQGP cards used in the static analysis of the orbiter model. This orbiter model contained all five substructures, but the substructuring procedure was not utilized in the Static Analysis (Rigid Format 1) executions in NASTRAN Level 15.5.

When the Guyan reduction (ref. 27) feature is being utilized in a Normal Mode Analysis run (Rigid Format 3) for a large problem, relatively inexpensive computer runs can be made to determine if resequencing reduces the bandwidth. One of these runs may involve no resequencing. Each of the runs should be checkpointed. Each run should be submitted with sufficient time to allow entry in the SMP1 module but insufficient time for completion of this module. The SMP1 module partitions the constrained stiffness matrix, solves for the transformation matrix, GO, and performs a matrix reduction to obtain the reduced stiffness matrix, KAA (see ref. 25, p. 3.4-7). User information messages are output with values for B, C, and R identified in equation (B1) and the decomposition time estimate in seconds. These messages are followed by a system fatal message which states that there is insufficient time remaining for RSPSDCM and gives the time estimate in seconds (RSPSDCM is the routine used for a real, single precision symmetric decomposition in the CDC version of NASTRAN). Following output of this message, the job is terminated by NASTRAN. The calculations are then continued on an unmodified restart run from the run selected. The computer time lost is that spent on runs which are not continued.

Eigenvalue Extraction

The need for faster eigensolution routines in NASTRAN was emphasized during the orbiter analysis. New routines should be developed for NASTRAN which would generate

all eigenvalues and up to about 50 eigenvectors for matrix orders up to approximately 500 in reasonable times. Since new routines were not available, two of the existing eigenvalue extraction methods (see ref. 32, section 10) in NASTRAN Level 15.5 were used to obtain the natural frequencies and mode shapes for the combined orbiter in the substructuring procedure described previously and also for the individual substructures.

Eigenvalue extraction by the Givens method.- The Givens method for extracting eigenvalues (transformation method based on the tridiagonalization techniques of Givens) was used for some of the phase I runs. Intermittent unscheduled exits occurred in some of these runs. Until errors are corrected, the Givens method in NASTRAN Level 15.5 is considered unreliable for eigenvalue extraction.

Eigenvalue extraction by the inverse power method with shifts.- The inverse power method with shifts for extracting eigenvalues was used on the phase II runs and some of the phase I runs. This tracking method is time consuming for large problems. Care must be exercised to ensure that absolutely all eigenvalues in the required range have been obtained. It is noted that a smaller field is required for this method in the READ (eigenvalue extraction) module than for execution of the SMP1 module which performs the Guyan reduction. Also, less field is required for the inverse power method than for the Givens method for eigenvalue extraction. One or more eigenvalues and eigenvectors can be obtained on an initial or restart run which is checkpointed. As previously mentioned, additional runs with modified frequency search ranges can be submitted until all the desired frequencies and modes are obtained.

Restarts

The restart capability in NASTRAN for utilizing data from previous executions was used on many of the orbiter runs. When using the appropriate Old Problem Tape (OPTP) on a subsequent run, the NASTRAN Data deck contained the Executive deck which included restart dictionary cards and an alter packet, a Case Control deck, and only modifications, if any, to the Bulk Data deck. The Bulk Data deck from the previously checkpointed run is contained on the OPTP. These cards, with two exceptions, must not be included again on a restart run since NASTRAN will abort the job if duplicate Bulk Data cards are found. However, the BEGIN BULK and ENDDATA cards — the two exceptions — must be included.

Unmodified restarts.- The NASTRAN Data deck for an unmodified restart included the full restart dictionary obtained on the previous checkpointed run and contained no modifications to the Bulk Data deck. The cards specifying DMAP alters to the rigid format prior to the last reentry point contained in the restart dictionary were removed from the alter packet in the Executive deck.

Modified restarts.- Restart tables are included in each rigid format description in reference 25, section 3. These tables were useful in determining which modules had to

be reexecuted when modifications were made to the bulk data. Although many different modified restarts were made, only two of those most frequently used are described.

When it was determined that the stiffness matrix had to be regenerated in the SMA1 module, only the first card from the restart dictionary was used and the entire alter packet was included. This mode of operation was convenient for the users and ensured that all modules would be reexecuted.

Substantial computer time was saved by executing modified restart runs when only the Real Eigenvalue Extraction Data card (EIGR) was changed. On these runs, the restart dictionary included the RESTART card with continuation cards through the last file checkpointed for reentry at the DPD module, which extracts the Eigenvalue Extraction Data from the Dynamics Data block. The DMAP sequence number for module DPD is 85 in Rigid Format 3. All DMAP alter cards specifying changes to the DMAP sequence prior to statement 85 were removed from the alter packet.

Pseudo restarts.- Pseudo restart runs are runs to obtain only additional output data from calculations made on previous executions. Several restart runs were made during the orbiter analysis. DMAP alters were inserted in the Executive deck to obtain printouts for selected matrices. Modifications were made in the Case Control deck for printing and/or plotting as required.

Changes in the plot package in the Case Control deck on a pseudo restart run will trigger execution or reexecution of only those modules related to plotting if a fully checkpointed run has been made previously. This mode of operation is desirable especially when solving large problems. The primary reason for using this method to obtain deformed plots is that the field length required for plotting is substantially less than that required for solution of medium or large problems. Thus, several runs can be submitted with different plot packages for a nominal cost compared with the cost for a large solution run.

Plotting

A post-processor system is utilized now for all graphics at the LRC computer complex. Use of this post-processor system, however, was optional during most of the orbiter runs. It was selected primarily to utilize on-line plotting capability which is both faster and less expensive than plotting on off-line devices available at the LRC computer complex. The general-purpose plotter was selected in the plot package in the Case Control deck. A PLT2 physical tape reel must be requested and mounted prior to NASTRAN execution whenever a plot package is included in the Case Control deck.

In order to obtain NASTRAN plots at the LRC computer complex, three programs must be executed in order but not necessarily on the same job submittal. These programs are as follows:

(1) NASTRAN, which generates plot commands for the general purpose plotter on the PLT2 reel (It is noted that the PLT2 reel is not released by the LRC version of NASTRAN Level 15.5.),

(2) NASTPLT, which reads the plot commands from the PLT2 reel and reformats them on the plot vector file, SAVPLT, in the format used by the LRC plotting post processors, and

(3) PLOT, which formats the plot vector file from the SAVPLT file into a plot vector file for the particular graphic device selected on its load-execute card and also allows modifications to be made to the plot vector file.

When on-line plots were obtained on the same job following NASTRAN execution, the field length held by the job was reduced to 52 000 octal in order to release excess core to the operating system.

Concluding Remarks

NASTRAN is an effective and versatile tool for predicting vibration response of complicated structures. However, orbiter analyses at the Langley Research Center required long computer execution times with large field lengths, which, under normal operating procedures, resulted in extended turnaround times. These turnaround times could be shortened only by obtaining priority of operation in the LRC computer complex. This situation is equivalent to having a dedicated computer available. The single DMAP alter packet and DMAP tape copy program provided by the Grumman Aerospace Corporation (refs. 21 and 26) for substructuring in NASTRAN is easier to use than the substructure analysis procedure described in the NASTRAN User's Manual (ref. 25). New eigensolution routines should be developed for NASTRAN which would generate all eigenvalues and up to about 50 eigenvectors for matrix orders up to approximately 500 in reasonable times.

APPENDIX C

FLEXIBILITY INVESTIGATION OF ORBITER JOINTS
AND DOOR LONGERON

Arthur I. Miller* and Murray Bernstein*

This appendix contains a brief description of the simulation of certain flexibilities not accounted for in the initial NASTRAN model. The most significant is the flexibility of the interface between the fin and the fuselage. Of the three models shown in figure 24, model F1 was based on an approximate structural analysis of the fin-fuselage interface, whereas models F2 and F3 were derived from comparisons of static analytical and test deflection data. The use of model F1 was limited to static analysis, but models F2 and F3 were used in both static and dynamic analyses. Of lesser importance are the flexibilities of the juncture between the cabin and cargo bay and the additional bending flexibility of the door longeron due to its discrete-point attachment to the longeron along the cargo bay.

Joint Flexibilities

Modification of the NASTRAN finite-element model to account for joint flexibility was most readily accomplished by adding spring elements. Values for the spring constants were derived either from a simple idealization of the structural characteristics of the model joints or from correlation between static test deflection data and analysis.

Fin-fuselage interface.- The interface shown in figures 23(a) and 23(b) is statically indeterminant and relatively complex. Loads to the fuselage are transmitted through the forward and aft spars by clips and by the fin-fuselage angle connection along the interface. Figure 23(b) shows the aft spar-clip connection. Loads through the center spar are transmitted by a gusset plate (fig. 23(a)) designed to transmit fin pitch into the main fuselage engine bulkhead. In attempting an analytical representation, it was assumed that only the forward and aft clips had to be considered and other elements were not significant. Such a model is designated as F1 in figure 24.

---

*Grumman Aerospace Corporation.

APPENDIX C

The actual specifications of the clips in model F1 are shown in sketch (C1).

Rear clip

1.905 cm (3/4")

2.22 cm (7/8")

1.27 cm (1/2")

1.59 cm (5/8")

70.35°

1.27 mm (0.050")

0.635 cm (1/4")

1.905 cm (3/4")

8.89 cm (3 1/2")

Front clip

1.905 cm (3/4")

1.905 cm (3/4")

1.27 cm (1/2")

1.27 cm (1/2")

40°

1.016 mm (0.040")

0.635 cm (1/4")

8.89 cm (3 1/2")

1.905 cm (3/4")

Sketch (C1)
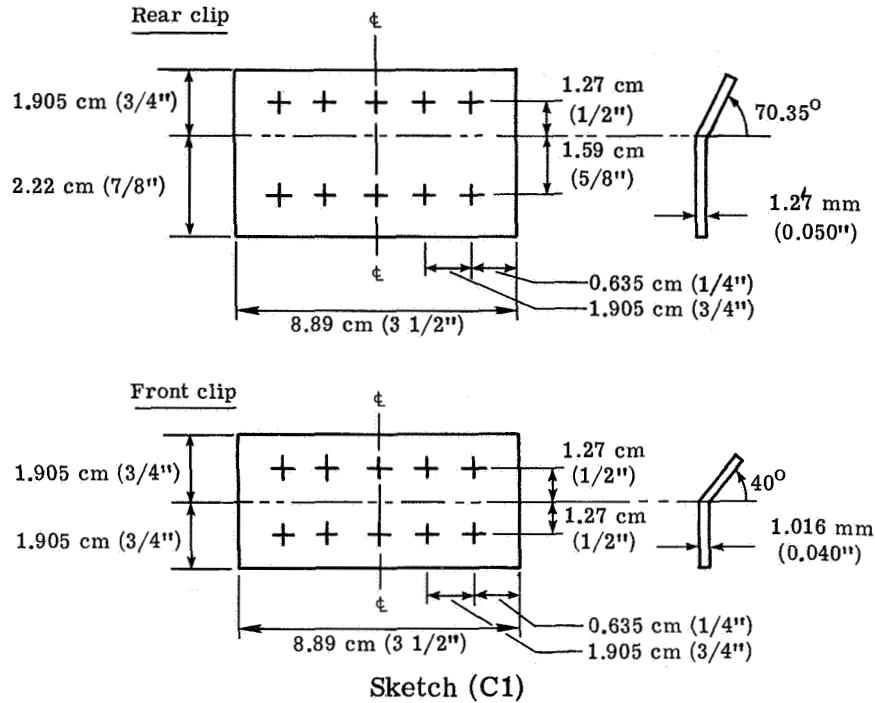
The idealization of the clip as a pin-roller attachment is an attempt to determine the flexibility of the clip itself. The spring constant K_{F1} of the idealized clip is determined from a consideration of bending energy alone. A representation of the fin-clip support is given in sketch (C2):

Sketch (C2)
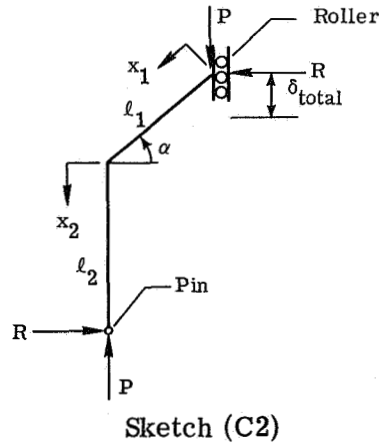
For the clip idealization shown therein, the strain energy in bending is given by:

$$U = \frac{1}{2} \int_0^{\ell_1} \frac{M_1{}^2}{EI_F} \, dx_1 + \frac{1}{2} \int_0^{\ell_2} \frac{M_2{}^2}{EI_F} \, dx_2 \qquad (C1)$$

The total deflection δ_{total} due to bending is

$$\delta_{total} = \int_0^{\ell_1} \frac{M_1 \frac{\partial M_1}{\partial P}}{EI_F} dx_1 + \int_0^{\ell_2} \frac{M_2 \frac{\partial M_2}{\partial P}}{EI_F} dx_2 \qquad (C2)$$

The bending moment in span ℓ_1 is given by

$$M_1 = \left(\frac{P\ell_2 \cos \alpha}{\ell_2 + \ell_1 \sin \alpha} \right) x_1 \qquad (C3)$$

and for span ℓ_2

$$M_2 = -\frac{P\ell_1 \cos \alpha \left(\ell_2 + x_2 \right)}{\ell_2 + \ell_1 \sin \alpha} \qquad (C4)$$

Then,

$$\delta_{total} = \frac{P}{3EI_F} \left(\overline{A}^2 \ell_1^3 + 7\overline{B}^2 \ell_2^3 \right) \qquad (C5)$$

where

$$\overline{A} = \frac{\ell_2 \cos \alpha}{\ell_2 + \ell_1 \sin \alpha} \qquad (C6a)$$

and

$$\overline{B} = -\frac{\ell_1 \cos \alpha}{\ell_2 + \ell_1 \sin \alpha} \qquad (C6b)$$

The spring constant K_{F1} of the idealized clip is given by

$$K_{F1} = \frac{P}{\delta_{total}} \equiv \frac{3EI_F}{\overline{A}^2 \ell_1^3 + 7\overline{B}^2 \ell_2^3} \qquad (C7)$$

Model F2 shows a single spring to be added to the NASTRAN model to account for the difference between analyses and test results. Only a forward spring was required because, as noted in the main body of this paper, the aft attachment in the fuselage had a negligible effect on the frequencies and the aft fuselage support frame, to which the clip is attached, is quite flexible.

It is assumed that the measured fore-and-aft deflection of the fin is composed of two components. One of these, $\delta_{a,s}$, is due entirely to fin fore-and-aft bending and is found from analysis to be small. The other deflection component Δ is assumed to be caused by joint rotation. The spring constant is determined solely for joint rotation and is given by the following set of relations shown in sketch (C3):
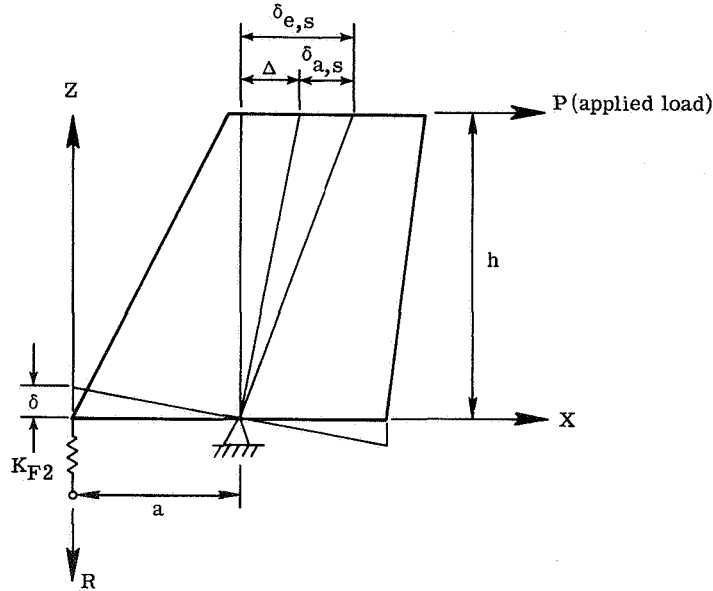
Sketch (C3)

Taking moments about the pivot yields

$$\left.\begin{array}{l} Ph = Ra \\[2mm] R = \dfrac{Ph}{a} \end{array}\right\} \qquad \text{(C8)}$$

or

The deflection required, $\Delta = \delta_{e,s} - \delta_{a,s}$, due to the rotation about the pivot yields

$$\left.\begin{array}{l} \dfrac{\delta}{a} = \dfrac{\Delta}{h} \\[3mm] \delta = \dfrac{a\Delta}{h} \end{array}\right\} \qquad \text{(C9)}$$

or

Thus, the spring constant

$$K_{F2} = \frac{R}{\delta} = \frac{Ph}{a}\frac{h}{a\Delta} = \frac{Ph^2}{\Delta a^2} \qquad \text{(C10)}$$

The spring constant used in the dynamic analysis $\left(K_{F2,dyn} \text{ in fig. 24}\right)$ was determined from the product of the spring constant used in the static analysis and the ratio of analytical-to-experimental deflections.

APPENDIX C

Model F3 in figure 24 shows the roll springs used in the antisymmetric loading. The roll springs were also determined from a correlation between experiment and analysis as shown by equations (C11) and (C12) and in sketch (C4) (based on ref. 21, vol. II).

Sketch (C4)

$$Ph = bR$$

or

$$R = \frac{Ph}{b}$$

(C11)

$$\Delta = \delta_{e,a} - \delta_{a,a}$$

$$\frac{2\delta}{b} = \frac{\Delta}{h}$$

(C12)

or

$$\delta = \frac{\Delta b}{2h}$$
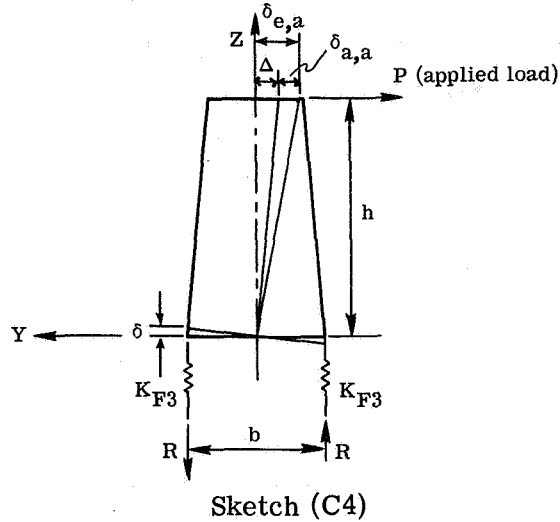
The spring constant K_{F3} is given by

$$K_{F3} = \frac{R}{\delta} = \frac{2Ph^2}{\Delta b^2}$$

(C13)

Again, the spring-constant value for the dynamic analysis $\left(K_{F3,dyn} \text{ in fig. 24}\right)$ was determined by multiplying K_{F3} by the ratio of analytical-to-experimental static deflections.

39

APPENDIX C

Comparison of finite-element models RS1 and RS2 with static test (see table X) indicates that fin model F1 allows excessive flexibility of the interface between fin and fuselage. Fin model F2 reduces the flexibility of the fin-fuselage interface through elimination of the aft clip spring. This is possible since the fuselage support frame (which has no underlying frame structure) to which the aft clip is attached is already quite flexible, as is evident in figure 23(b). Other rod-shear panel models RS4 and RS5 and reduced membrane model RM1 yield fin deflections of sufficient accuracy (approximately ±10 percent of measured fin deflection) when using fin model F2. Fin model F3, used in the case of antisymmetric loading, yields fin deflections within 5 percent of measured data, as indicated by the results shown in table XI.

The dynamic effects of joint flexibility are shown in table XII in a comparison of symmetric-mode orbiter frequencies calculated using model F2 flexibility with initial analytical frequencies and with measured frequencies. As may be seen, this modification resulted in about a 15- to 25-percent discrepancy between analytical and measured frequencies. Fin-fuselage flexibility thus accounts for $13\frac{1}{2}$ percent of the disagreement between initial analytical and measured frequencies in the first mode and for as much as 58 percent in the fourth mode.

Cabin-to-payload bay juncture.- The CPB joint experiences primarily axial loading during fuselage vertical bending. The axial loading is assumed to be carried by the aluminum splices across the 0.0813-cm (0.032-in.) joint gap. The upper splice is further assumed to transmit bending due to the 6° bend. The upper splice may be idealized as a pin-roller configuration for bending deflection as in model F1 of figure 24.

Joint flexibility for the upper splice is based on the deflection relation

$$\delta_{upper} = \delta_{x,axial} + \delta_{x,bending} \tag{C14}$$

and for the lower splice

$$\delta_{lower} = \delta_{x,axial} \tag{C15}$$

The structural idealization of the upper splice is illustrated in sketch (C5):
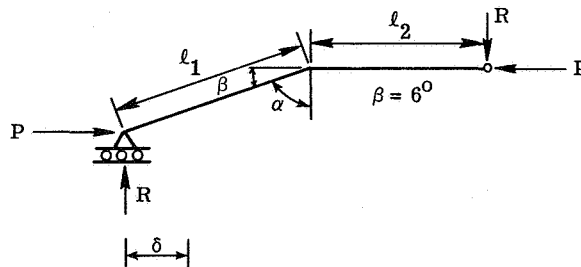
Sketch (C5)

Then, for the upper splice,

$$\delta_{x,axial} = \frac{1}{A_p E}\left[(P \cos \beta + R \sin \beta)\ell_1 + P\ell_2\right] \tag{C16}$$

where

$$R = \frac{P\ell_1 \cos \alpha}{\ell_2 + \ell_1 \sin \alpha}$$

and

$$\delta_{x,bending} = \frac{P}{3EI_p}\left(\overline{A}^2\ell_1^3 + 7\overline{B}^2\ell_2^3\right) \tag{C17}$$

where

$$\left.\begin{array}{l}\overline{A} = \dfrac{\ell_2 \cos \alpha}{\ell_2 + \ell_1 \sin \alpha} \\[2em] \overline{B} = -\dfrac{\ell_1 \cos \alpha}{\ell_2 + \ell_1 \sin \alpha}\end{array}\right\} \tag{C18}$$

therefore,

$$\frac{\delta_{upper}}{P} = \frac{1}{A_p E}\left[(\cos \beta - \overline{B} \sin \beta)\ell_1 + \ell_2\right] + \frac{1}{3EI_p}\left(\overline{A}^2\ell_1^3 + 7\overline{B}^2\ell_2^3\right) \tag{C19}$$

The linear spring K_u for the upper splice is simply P/δ_{upper}, or

$$K_u = \frac{1}{\dfrac{1}{A_p E}\left[(\cos \beta - \overline{B} \sin \beta)\ell_1 + \ell_2\right] + \dfrac{1}{3EI_p}\left(\overline{A}^2\ell_1^3 + 7\overline{B}^2\ell_2^3\right)} \tag{C20}$$

and the spring K_ℓ for the lower splice is given by P/δ_{lower}, or

$$K_\ell = \frac{1}{b_p/A_p E} = \frac{A_p E}{b_p} \tag{C21}$$

Assuming that the upper and lower splices act as springs in parallel, a new spring constant for the complete joint is simply the sum of the two spring constants K_u and K_ℓ.

APPENDIX C

The value of the total spring constant is given in figure 25. The greater portion of this value comes from K_l since no bending deflection is included as it is in the value for K_u. The actual values of K_l and K_u are given as follows:

$$K_l = \frac{1}{\delta_{x,axial}} = 28\ 895 \text{ kN/m} \quad (165\ 000 \text{ lb/in.})$$

$$K_u = \frac{1}{\delta_{x,axial} + \delta_{x,bending}} = 1999 \text{ kN/m} \quad (11\ 412 \text{ lb/in.})$$

Assessment of the CPB spring on static deflection cannot be made since no attempt was made to isolate its effect from other aspects of the analytical models. Dynamically, the CPB spring had negligible effect on frequencies and mode shapes in fuselage phase I (substructure) analysis.

Door Longeron Effectiveness

In the initial NASTRAN model, the door longeron was considered fully effective during fuselage bending. However, the door is attached physically to the fuselage by four shear pins spaced approximately 63.50 cm (25 in.) apart. One pin is shown in the door clip of figure 6. These are fastened into clips which bring the restraint point down about 2.54 cm (1 in.) below the neutral axis of the door longeron. Any axial (x-direction) load applied by the shear pins will result in a combination of extension and rotation of the door longeron. The bending flexibility due to rotation had not been accounted for and was therefore added. The rotational flexibility of the longeron as a beam was calculated as a small separate NASTRAN problem and translated into an effective reduction in cross-sectional area from 0.3613 cm^2 $\left(0.056 \text{ in}^2\right)$ for the original longeron to 0.1290 cm^2 $\left(0.02 \text{ in}^2\right)$. This modification resulted in a decrease in calculated fuselage bending stiffness of about $4\frac{1}{2}$ percent. An alternative approach adopted in reference 21 was remodeling this area by revising the geometry and adding additional grid points and constraint relationships.

The calculated flexibilities (i.e., deflections for unit loads) with the doors on were a reasonable match with measured flexibilities, but with doors off, the analytical model was too flexible. The results of the static test, upon initial review, indicated no significant difference in deflection with and without the doors. However, strain gages on the door indicated that the door-longeron stresses were about half those in the fuselage longeron and therefore the door was partially effective. Dynamically, the reduction in longeron area caused a negligible effect on frequencies and mode shapes.

APPENDIX C

Concluding Remarks

Investigation of the flexibility at the fin-fuselage interface has shown that fin models F2 and F3 yield fin deflections within 10 percent of measured deflections. Dynamically, fin model F2 accounts for approximately $13\frac{1}{2}$ percent of the first-mode frequency discrepancy between initial analysis and test. The effect of the CPB spring and reduction of the door longeron area result in negligible effects on overall orbiter frequencies and mode shapes.

APPENDIX D

NASTRAN MODELING ACCURACY STUDIES

Jerrold M. Housner and Manuel Stein

The purpose of this appendix is to present and discuss results of two studies which were undertaken to evaluate NASTRAN modeling accuracy for dynamic response of the fuselage of the 1/8-scale shuttle orbiter model. In the first study, the general capability of NASTRAN to predict accurately the response of the fuselage-like structure shown in figure 41 is considered, where shear lag and cross-sectional warping are included. The second study is concerned with the effect on the natural frequencies and mode shapes of high aspect ratio of NASTRAN's QDMEM2 membrane elements used in the orbiter fuselage.

Symbols

a_1, a_2, a_3 amplitudes of deflection functions for symmetric modes

$\hat{a}_1, \hat{a}_2, \hat{a}_3, \hat{a}_4$ amplitudes of deflection functions for antisymmetric modes

A_1, A_2, A_3, A_4 cross-sectional areas of fuselage stiffening rods

A_f, A_w, A_k cross-sectional areas of floor, wall, and keel, respectively

A_T total cross-sectional area, $2(A_1 + A_2) + A_3 + A_4 + A_f + 2A_w + A_k$

b semichord of fuselage cross section

C_θ warping coefficient given by equation (D18)

C_1 coefficient given by equation (D7)

E Young's modulus

f_{ij} coefficients defined by equation (D11)

G shear modulus

h_w, h_k heights of wall and keel, respectively

I_f $= \dfrac{1}{6} bt_2^3$

I_k $\qquad = \frac{1}{12} h_k t_1^3$

I_w $\qquad = \frac{1}{12} h_w t_3^3$

I_y, I_z $\qquad$ moments of inertia about axes passing through the cross-sectional centroid and parallel to the Y- and Z-axes, respectively

I_o $\qquad$ polar moment of inertia of cross section about the origin

$\overline{I}$ $\qquad$ effective moment of inertia defined by equation (D5)

J $\qquad$ torsion constant given by equation (D17)

ℓ $\qquad$ length of simplified fuselage

m $\qquad$ mass per unit length of the fuselage

s $\qquad$ cross-sectional coordinate, as shown in figure 42

t_1, t_2, t_3 $\qquad$ thicknesses of keel, floor, and wall, respectively

u $\qquad$ axial displacement (x-direction)

v $\qquad$ transverse displacement (y-direction)

w $\qquad$ lateral displacement (z-direction)

$\overline{u}_i, \overline{v}_i, \overline{w}_i$ $\qquad$ deflection functions defined by equations (D1) to (D3)

x, y, z $\qquad$ Cartesian coordinate system (see fig. 42)

z_o $\qquad$ shear-center offset from centroid in z-direction

ϵ $\qquad$ shear-center offset from Y-axis

θ, θ_i $\qquad$ clockwise rotation of cross section, as well as displacement function defined by equation (D3)

ψ_i $\qquad$ displacement function defined by equation (D1)

APPENDIX D

ν Poisson's ratio

ω angular frequency, rad/sec

ρ mass density

The primes indicate differentiation with respect to x.

Methods of Analysis

To confirm the NASTRAN results for a simplified fuselage model, two closed-form mathematical analyses were performed. One analysis, developed herein, was based on an energy approach using an assumed displacement state, piecewise linear along the cross-sectional perimeter. The second analysis was based on a thin-walled, open-section theory (ref. 33). Included also are descriptions of two NASTRAN models of the simplified fuselage of figure 41. In contrast to the 1/8-scale orbiter fuselage, the simplified fuselage has uniform geometric and material properties along its length.

Piecewise linear analysis.- Due to symmetry, only half the fuselage cross section needs to be considered, as shown in figure 42. This model may be viewed as consisting of three plates — the keel, the floor, and the wall — and periodically spaced frames. The fuselage frames (fig. 41) are considered to be stiff enough so that the strain ϵ_s and curvature κ_{ss} in each plate is zero. The subscripts here are associated with the cross-sectional coordinates running counterclockwise around the cross section as shown in figure 42. Under this stiff-frame assumption, the deformations of the middle plane of each plate may be expressed as the following piecewise linear functions of s:

$$u_i(x,s) = \bar{u}_i(x) + s\psi_i(x) \tag{D1}$$

$$v_i(x,s) = \bar{v}_i(x) \tag{D2}$$

$$w_i(x,s) = \bar{w}_i(x) + s\theta_i(s) \tag{D3}$$

where i = 1, 2, and 3 identifies keel, floor, and wall, respectively. In equation (D1) the inclusion of the function $\psi_1(x)$ allows for the warping of the cross section, while in equation (D3) the function $\theta_i(x)$ allows for the rotation of the cross section.

Equations (D1) to (D3) indicate 15 unknown functions, but not all of these are independent. Since the displacements must be continuous at the joints and right angles must

46

be preserved at the joints, w_i and $\partial w_i/\partial s$ must be continuous. This implies eight continuity constraints on the unknown functions.

Symmetric modes: For symmetric modes, the following additional constraints may be imposed:

$$\overline{w}_1 = \theta_1 = \psi_2 = \theta_2 = 0 \tag{D4}$$

Consequently, upon application of the continuity and symmetry constraints, only three unknowns remain in equations (D1) to (D3). Calculation of the strains in each plate and application of the variational principle finally leads to the following equations of motion:

$$E\overline{I}\left(\overline{w}_2^{IV} + \frac{m\omega^2\overline{w}_2''}{2A_wG}\right) - m\omega^2\overline{w}_2 = 0 \tag{D5}$$

$$\psi_1''' = \frac{m\omega^2\overline{w}_2}{E\overline{I}} \tag{D6}$$

$$\overline{u}_2'' = C_1\psi_1'' \tag{D7}$$

where

$$\overline{I} = \frac{2}{3(1-\nu^2)}\left(h_w^2A_w + h_k^2A_k\right) + 2A_1h_w^2 + A_4h_k^2$$

$$- C_1\left[\frac{1}{1-\nu^2}\left(h_wA_w + h_kA_k\right) + 2A_1h_w + A_4h_k\right]$$

and

$$C_1 = \frac{h_wA_w + h_kA_k + \left(2h_wA_1 + A_4h_k\right)\left(1-\nu^2\right)}{A_f + 2A_w + A_k + \left(2A_1 + 2A_2 + A_3 + A_4\right)\left(1-\nu^2\right)}$$

The solution to equations (D5) to (D7) for simply supported boundary conditions is

$$\overline{w}_2 = a_1 \sin\frac{n\pi x}{\ell} \tag{D8a}$$

$$\psi_1 = a_2 \cos\frac{n\pi x}{\ell} \tag{D8b}$$

$$\overline{u}_2 = a_3 \cos\frac{n\pi x}{\ell} \tag{D8c}$$

Substitution of equation (D8a) into equation (D5) yields the frequency relation

$$\frac{\omega^2 \ell^4}{E\bar{I}/m} = \frac{n^4}{1 + \frac{E\bar{I}}{2GA_w}\left(\frac{n\pi}{\ell}\right)^2} \tag{D9}$$

When $\dfrac{E\bar{I}\pi^2}{2GA_w\ell^2} \ll 1$, the lowest frequency is found for $n = 1$. Once the frequency is determined, the corresponding mode shapes may be obtained from equations (D5) to (D8).

Antisymmetric modes: For antisymmetric modes, the following constraints replace equation (D4):

$$\bar{u}_1 = \psi_1 = \bar{v}_1 = 0 \tag{D10}$$

Consequently, upon application of continuity and antisymmetric constraints, there are four unknowns remaining in equations (D1) to (D3). Calculation of the strains in each plate and application of the variational principle result in the following set of equations:

$$\left[f\right]\begin{Bmatrix} \hat{a}_1 \\ \hat{a}_2 \\ \hat{a}_3 \\ \hat{a}_4 \end{Bmatrix} = 0 \tag{D11}$$

where the elements of matrix $\left[f\right]$ are

$$f_{11} = \left(\frac{n\pi}{\ell}\right)^4 \frac{E}{3(1-\nu^2)}\left(b^2 I_f + 2h_w{}^2 I_w + h_k{}^2 I_k\right) + 2G\left(\frac{n\pi}{\ell}\right)^2\left(I_f + 2I_k + 4I_w + b^2 A_w\right)$$

$$- \rho\omega^2\Big[2b^2 A_w + \frac{1}{3}b^2 A_f + \frac{2}{3}h_w{}^2 A_w + \frac{1}{3}h_k{}^2 A_k$$

$$+ 2b^2\left(A_1 + A_2\right) + 2h_w{}^2 A_1 + h_k{}^2 A_4 + I_f\Big]$$

$$f_{12} = f_{21} = \left(\frac{n\pi}{\ell}\right)^4\left(\frac{E}{1-\nu^2}\right)\left(h_w I_w + \frac{1}{2}h_k I_k\right) - \rho\omega^2\left(h_w A_w + \frac{1}{2}h_k A_k + 2h_w A_1 + h_k A_4\right)$$

$$f_{13} = f_{31} = 0$$

$$f_{14} = f_{41} = -2bGA_w\frac{n\pi}{\ell}$$

$$f_{22} = \frac{E}{1 - \nu^2}\left(\frac{n\pi}{\ell}\right)^4\left(2I_w + I_k\right) + A_f G\left(\frac{n\pi}{\ell}\right)^2 - \rho\omega^2\left(2A_w + A_f + A_k + 2A_1 + 2A_2 + A_3 + A_4\right)$$

$$f_{23} = f_{32} = -\frac{n\pi}{\ell} GA_f$$

$$f_{24} = f_{42} = 0$$

$$f_{33} = \left(\frac{n\pi}{\ell}\right)^2\left(\frac{E}{1 - \nu^2}\right)\left[\frac{1}{3} b^2 A_f + 2b^2 A_w + 2b^2\left(A_1 + A_2\right)\right] + GA_f$$

$$f_{34} = f_{43} = -\left(\frac{n\pi}{\ell}\right)^2\left(\frac{E}{1 - \nu^2}\right)\left[bh_w A_w + 2bh_w A_1\left(1 - \nu^2\right)\right]$$

$$f_{44} = \frac{2}{3} h_w^2 A_w\left(\frac{n\pi}{\ell}\right)^2\left(\frac{E}{1 - \nu^2}\right) + 2GA_w + 2EA_1 h^2\left(\frac{n\pi}{\ell}\right)^2$$

Nontrivial solutions to equation (D11) are obtained from the determinantal frequency equation

$$\left| f \right| = 0 \tag{D12}$$

which yields eigenvalues and eigenvectors. From the eigenvectors $\langle \hat{a} \rangle$, the mode shapes may be found from the following relations:

$$\theta_1 = \theta_2 = \theta_3 = \hat{a}_1 \sin\frac{n\pi x}{\ell} \tag{D13a}$$

$$\bar{v}_2 = \hat{a}_2 \sin\frac{n\pi x}{\ell} \tag{D13b}$$

$$\psi_2 = -\hat{a}_3 \cos\frac{n\pi x}{\ell} \tag{D13c}$$

$$\psi_3 = \hat{a}_4 \cos\frac{n\pi x}{\ell} \tag{D13d}$$

Analysis of thin-walled open section.- In reference 33, Chajes and Winter present a theory for the buckling of thin-walled open-section columns. In order to make this theory applicable to vibrations, the buckling terms in their equations are replaced by the appropriate inertial terms; and advantage is taken of symmetry to reduce the equations to

$$EI_y w^{IV} - m\omega^2 w = 0 \tag{D14}$$

$$EI_z v^{IV} - m\omega^2 v - m\omega^2 z_0 \theta = 0 \tag{D15}$$

$$EC_\theta \theta^{IV} - GJ\theta'' - \frac{m\omega^2 I_0}{A_T} \theta - m\omega^2 z_0 v = 0 \tag{D16}$$

where

$$J = \frac{2}{3}\left(bt_2^{\ 3} + h_w t_3^{\ 3}\right) \tag{D17}$$

$$C_\theta = \frac{2}{3} b^2 t_2 \left[\epsilon^3 - \left(h_w - \epsilon\right)^3\right] + \frac{2}{3} \epsilon^2 t_3 b^3 + 2A_1 b^2 \left(h_w - \epsilon\right)^2 + 2A_2 b^2 \epsilon^2 \tag{D18}$$

The term $EC_\theta \theta^{IV}$ provides the inherent resistance of the cross section to warping; I_y and I_z are the cross-sectional moments of inertia about axes passing through the centroid and parallel to the Y- and Z-axes, respectively; I_0 is the polar moment of inertia of the cross section about the origin; z_0 is the offset of the shear center from the centroid in the z-direction; ϵ is the offset of the shear center from the Y-axis.

Symmetric modes: For modes which are symmetric about the plane $y = 0$, $\theta \equiv 0$ and vibrations are governed by equation (D14), which is clearly the simple beam equation without transverse-shear effects.

Antisymmetric modes: For modes which are antisymmetric about the plane $y = 0$, $w \equiv 0$ and v and θ are given by

$$v = V \sin \frac{n\pi x}{\ell} \tag{D19}$$

$$\theta = \Theta \sin \frac{n\pi x}{\ell} \tag{D20}$$

Substitution of equations (D19) and (D20) into equations (D15) and (D16) yields the following frequency equation for nontrivial solutions:

$$\begin{vmatrix} EI_z\left(\frac{n\pi}{\ell}\right)^4 - m\omega^2 & -m\omega^2 z_0 \\ -m\omega^2 z_0 & EC_\theta\left(\frac{n\pi}{\ell}\right)^4 + GJ\left(\frac{n\pi}{\ell}\right)^2 - m\omega^2 \frac{I_0}{A_T} \end{vmatrix} = 0 \tag{D21}$$

The lowest frequency of equation (D21) occurs for $n = 1$.

50

APPENDIX D

NASTRAN models.- Two NASTRAN models of the simplified fuselage of figure 41 were considered and are shown in figure 43. As a consequence of symmetry, only a quarter of the fuselage needs to be retained. Both coarse (fig. 43(a)) and refined (fig. 43(b)) models were necessary to confirm convergence of solutions. Before Guyan reduction the coarse and refined models for the quarter fuselage contained 128 and 746 degrees of freedom, respectively, for the symmetric modes, and 112 and 694 degrees of freedom, respectively, for the antisymmetric modes. Comparison of these numbers (doubled) with those in table V shows that the coarse and refined models bracket the 1/8-scale fuselage model, with the refined model having nearly the same number of degrees of freedom as the 1/8-scale fuselage model.

A simple support at the end $x = 0$ was provided by setting $v = w = 0$ at all nodal (or grid) stations around the end. Setting the longitudinal displacement u, together with pitch and yaw rotations, equal to zero at all grid stations at the fuselage midspan gave the symmetric modes which included the lowest modes of interest.

For modes which are symmetric about the plane $y = 0$, the longitudinal displacement u, together with roll and yaw rotations, were set equal to zero at all grid points in the plane. For modes which are antisymmetric about this plane, the longitudinal displacement u, the vertical displacement w, and the pitch rotation were set equal to zero at all grid points in the plane.

Evaluation of NASTRAN Models for Vibration Analysis

The general capability of NASTRAN to predict accurately frequencies and mode shapes of the fuselage was determined by comparing NASTRAN solutions with the closed-form mathematical solutions previously described for the simplified model of figure 41. The geometric and material properties were considered uniform along the length of the model and are listed in table XIII. The length of the model was chosen to correspond to the distance between nodal points of the 1/8-scale fuselage in its first symmetric or antisymmetric mode, and, as previously noted, the ends were taken to be simply supported. As also previously observed, fuselage symmetry about the plane $y = 0$ enables the separation of modes into symmetric or antisymmetric about this plane. Furthermore, for the antisymmetric modes, the shear center — though lying in the plane $y = 0$ — does not coincide with the cross-sectional centroid. Consequently, lateral bending and torsion motions are coupled.

Frequencies calculated by both closed-form mathematical analyses are compared with NASTRAN frequencies in table XIV for the first symmetric and antisymmetric modes. In general, the results for each mode are in good agreement, and in particular, the refined NASTRAN model (fig. 43(b)) is in excellent agreement with the piecewise linear analysis. For the symmetric mode, the frequency by the beam solution is 12 percent higher than

51

that by the piecewise linear analysis. As is evident from equation (D9), the sole difference between the two solutions is the inclusion of transverse shear in the piecewise linear analysis. Hence, transverse shear is important in this mode.

In figure 44, the axial displacements and shearing stresses at a simple support are shown for the NASTRAN refined model and the piecewise linear model for the first symmetric mode. The agreement is seen to be excellent. In figure 45, the axial displacements and shearing stresses at a simple support, along with the lateral and transverse displacements at the fuselage midspan, are shown for the first antisymmetric mode. Again the agreement in displacements is excellent. The agreement in shearing stresses is also very good; however, as is often the case, the agreement is not as good as that for the displacements. It is also of interest to note in figure 45(b) the sizable amount of cross-sectional warping which takes place.

Although not shown, the modal displacements predicted by the coarse model were up to 6 percent less than those of the refined model. It is not reasonable to compare the modal stresses predicted by the coarse and refined models, since the NASTRAN predicted stresses are not at specific points, but are averages over an element, and the coarse elements are about six times bigger than the refined elements.

In summary, the coarse NASTRAN model (fig. 43(a)) was within 6 percent of the piecewise-linear solution, whereas the refined model provided excellent results $\left(\text{within } 1\frac{1}{2} \text{ percent of the piecewise-linear solution}\right)$.

Aspect Ratio Characteristics of NASTRAN Membrane Elements

The NASTRAN model of the 1/8-scale orbiter fuselage is largely composed of flat quadrilateral membrane finite elements. In general, these elements are too stiff in in-plane bending and must therefore be used cautiously in portions of a structure subjected to in-plane bending (see ref. 34). In particular, the QDMEM2 membrane element, used in the NASTRAN model, loses significant accuracy at high aspect ratios. This was demonstrated in an unreported analysis by William C. Walton, Jr., and Huey D. Carden of NASA Langley Research Center. Using a cantilever beam made up predominantly of QDMEM2 elements of aspect ratio 5 and subjected to a static concentrated load at the beam tip, they obtained an in-plane bending stiffness that was about 37 percent higher than the classical beam solution. This increase corresponds to a frequency 17 percent too high. With panels of aspect ratio 3, the stiffness increase was 17 percent, which corresponds to an 8-percent frequency increase.

Since the QDMEM2 elements were used with aspect ratios as high as 4 in the 1/8-scale orbiter model, it was considered necessary to examine their effect on NASTRAN predicted fuselage frequencies. Three separate studies were undertaken.

APPENDIX D

In the first study (ref. 21, vol. II) by Philip W. Mason (GAC), it was found that in modeling a structure like the fuselage with spar caps on the tension and compression sides, the stiffness increase due to high-aspect-ratio QDMEM2 elements is reduced as the spar-cap cross-sectional area is increased. Relating this result to a typical fuselage station, Mason estimated the frequency increase would be less than 5 percent. It is reasonable to conclude that when the spars are stiff enough to carry the burden of the bending loads, the membrane elements, acting together, behave like a shear web, and, since the membrane elements are designed to resist in-plane shear, the error due to their presence is reduced.

In an unreported second study by John L. Sewall (LRC), the vertical membrane fuselage sidewall in the payload-bay area, forward of the wing carry-through structure, was remodeled with an equivalent rod-shear panel combination. Imposing in-plane static loading on both the membrane and equivalent sidewall models resulted in only a 2- to 3-percent increase in stiffness of the membrane panel over that of the equivalent rod-shear panel model. Further examination showed that this difference for the sidewall could be attributed to interspersing panels of aspect ratio 1 and 2 among panels of aspect ratio 3 and 4 in the original membrane model.

Finally, in the third study (reported herein), a NASTRAN model of the simplified fuselage shown in figure 46 was considered. This model was composed of nearly all aspect-ratio-3 QDMEM2 elements; and an attempt was made to have, on the average, about the same number of elements in both the sidewalls and the floor of the fuselage as was in the original 1/8-scale NASTRAN fuselage model. This study showed only a 2-percent frequency increase compared with the refined NASTRAN model of figure 43(b), in which the panel elements were of aspect ratio 1.

In summary, it appears that the use of relatively high aspect-ratio QDMEM2 elements in the orbiter NASTRAN model will raise the frequency only a few percent. This increase would probably be higher if all the elements were of high aspect ratio or if spars were not present in the fuselage.

Conclusions

Results of the investigation reported warrant the following conclusions:

1. In general, NASTRAN solutions of a simplified orbiter fuselage structure for vibration mode shapes and frequencies correlated reasonably well with solutions by closed-form mathematical analyses. A coarse NASTRAN model with two panel elements in the walls and four in the floor gave frequencies within 6 percent. Refining the model to include 5 elements in the walls and 10 in the base greatly improved the accuracy to within $1\frac{1}{2}$ percent.

APPENDIX D

2. The use of relatively high aspect-ratio membrane elements (QDMEM2) in the orbiter NASTRAN model does not result in a frequency increase of more than a few percent. This increase is expected to be higher with all panel elements of high aspect ratio and/or without spars on the tension and compression sides of the fuselage.

APPENDIX E

PANEL IMPERFECTION STUDIES

Murray Bernstein* and John L. Sewall, Coordinators

In the original NASTRAN model, membrane elements making up the external fuse-lage and wing surfaces were considered fully effective in transmitting in-plane direct and shear stresses. However, inspection of the physical model showed that most surface panels were not perfectly flat but had initial out-of-plane bow considerably more in magnitude than the panel thickness. This deviation suggested that the panels could not be fully effective in carrying the in-plane stress. This was especially true of panels having large unsupported areas. This ineffectiveness was further evident in observations of localized oscillations during vibration testing and in strain-gage readings from static tests. To obtain an indication of the sensitivity of the vibration modes to reduced panel effectiveness, the vertical sidewalls of the analytical fuselage were remodeled with rods and shear panels replacing the membrane panels, and a complete NASTRAN vibration analysis (i.e., through phase II, see fig. 21) was made. The rods were of token or minimal, cross-sectional areas to stabilize the shear panels. The results of this analysis appear in table XV.

The significant frequency reductions produced by this modification stimulated a search for a valid measure of panel effectiveness. This search was followed along two general paths: First, static test deflections were compared with static analytical deflections to determine and evaluate candidate panel modifications; and second, independent studies were conducted both at LRC and GAC to determine effectiveness criteria.

Results from both approaches were applied in NASTRAN vibration analyses for comparison with measured frequencies and mode shapes. Frequencies of all the panel-effectiveness models are listed in table XVI along with the initial analytical frequencies and measured frequencies.

PANEL EFFECTIVENESS BASED ON STATIC TEST DATA

Arthur I. Miller*, Jack R. Barrett**, and Murray Bernstein*

Panel Effectiveness in Direct Stress

The initial analytical deflection curves when compared to static test points showed a uniformly stiffer appearance than the test model deflection curve (see figs. 47 to 49).

---

*Grumman Aerospace Corporation.
**Rockwell International Corporation.

APPENDIX E

The continuity of the deflection curve suggested a general overstiffness rather than a localized overstiffness. A general overstiffness was suspected in modeling the panels with fully effective skins. In modeling beam webs by rods and shear panels, one-sixth of the panel cross-sectional area is concentrated in the cap areas to represent a fully effective web in bending (as shown in ref. 35). However, the panel shear capability remains fully effective. This concept is applicable in representing the fuselage side-wall in vertical bending and the fuselage bottom panels in lateral bending.

When modeling skin-stringer structures subjected to compressive loads, the stringer and some skin is assumed effective. This is the case with wing cover sheets in wing bending and fuselage sidewalls and bottom panels in lateral and vertical bending, respectively. The problem then is to determine how much skin is actually effective. A number of analyses with varying amounts of effective skin could be run in order to achieve a correlation between static test deflections and analysis. However, it was considered more expedient to solve for an amount of effective skin in the test model directly and use it in the revised analytical model.

From the deflection equation normalized to a unit load

$$\delta \propto F \qquad\qquad (F = 4.45 \text{ N } (1 \text{ lb})) \qquad\qquad (E1)$$

where the constant of proportionality involves length cubed divided by bending stiffness EI. The modulus E and lengths of the analytical model were considered to be equivalent to those of the test model, thus allowing only the flexural moment of inertia I to vary by the amount of effective skin. The equation relating test and analysis can be stated as

$$\delta_T I_T = \delta_A I_A \qquad\qquad (E2)$$

and the moment of inertia of the test model I_T can be expressed as the ratio of maximum analytical-to-test deflections (δ_A/δ_T) multiplied by the moment of inertia for the initial analysis I_A, based on fully effective panels; i.e.,

$$I_T = \left(\frac{\delta_A}{\delta_T}\right) I_A \qquad\qquad (E3)$$

This effective I_T in the test model now becomes the required moment of inertia in the revised analytical model. The skin area required in the analytical model to satisfy I_T is formulated for the fuselage and wing in the next two sections.

Fuselage representation.- The fuselage is idealized as shown in sketch (E1).
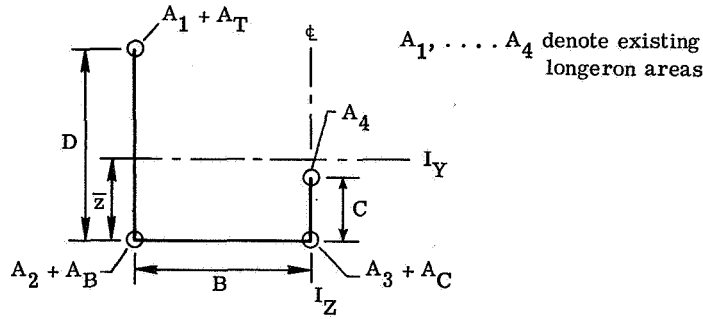
Sketch (E1)

Fuselage effective skin areas A_T, A_B, and A_C are determined by assuming that the neutral axis location of a fuselage section with fully effective skins is maintained, even though the moment of inertia for the section is reduced. The neutral axis of a cross section in terms of the unknown areas A_T, A_B, and A_C is given by

$$\bar{z} = \frac{\left(A_1 + A_T\right)D + A_4 C}{\left(A_1 + A_2 + A_3 + A_4\right) + \left(A_T + A_B + A_C\right)} \tag{E4}$$

Moments of inertia required at a cross section are determined by the following:

$$I_Y = \left(\frac{\delta_A}{\delta_T}\right)_Z I_{A,Y} = \left(A_1 + A_T\right)(D - \bar{z})^2 + \left(A_2 + A_3 + A_B + A_C\right)\bar{z}^2 + A_4(C - \bar{z})^2 \tag{E5}$$

and

$$I_Z = \left(\frac{\delta_A}{\delta_T}\right)_Y I_{A,Z} = \left(A_1 + A_2 + A_T + A_B\right)B^2 \tag{E6}$$

where

$\left(\dfrac{\delta_A}{\delta_T}\right)_Z$ ratio of maximum deflections between analysis and test in the z-direction

$\left(\dfrac{\delta_A}{\delta_T}\right)_Y$ ratio of maximum deflections between analysis and test in the y-direction

and the moments of inertia of the rods about their own centroids are neglected.

The terms $I_{A,Z}$ and $I_{A,Y}$ represent moments of inertia of fuselage cross sections with fully effective skins about the neutral Z- and Y-axes. Solution of equations (E4) to (E6) yields the three skin areas. These areas are:

$$A_T = \frac{I_Y - A_1 D(D - \bar{z}) + A_4 C(C - \bar{z})}{D(D - \bar{z})}$$

(E7)

$$A_B = \frac{I_Y - (A_1 + A_T)(D - \bar{z})^2 - A_4(C - \bar{z})^2}{\bar{z}^2} - (A_2 + A_3 + A_C)$$

(E8)

$$A_C = \frac{I_Y + A_4 C(C + D - 2\bar{z})}{\bar{z}(D - \bar{z})} - \frac{I_Z}{B^2} - (A_3 + A_4)$$

(E9)

The values of these areas over representative fuselage stations, as shown in table XVII, indicated that they were equivalent to having 46 percent of the cross-sectional skin area in the cargo bay effective in direct stress. The three areas were each represented by rod elements at the indicated locations adjacent to existing longerons, and the skin was modeled by shear panels, together with minimal rods where actual rods did not exist. The NASTRAN model RS2 was modeled in this fashion.

Included also in table XVII are effective areas arbitrarily distributed according to the 1/6-area criterion described earlier and amounting to 33 percent of the total skin cross-sectional area. This criterion was used to model RS1.

Wing representation.- The effective skin for carrying direct stress in the wing and wing carry-through structure was found in a manner similar to that for the fuselage. The total area moment of inertia $I_{A,X}$ of the initial analytical model at various cross sections along the span was reduced by the wing-tip deflection ratio $\left(\delta_A / \delta_T\right)_Z$ to give the required inertias I_X for the revised analytical model as follows:

$$I_X = \left(\frac{\delta_A}{\delta_T}\right)_Z I_{A,X}$$

(E10)

The deflections involved in this equation are shown in the following sketch (E2):

Sketch (E2)

APPENDIX E

A simplified typical wing cross section between two spars is represented in sketch (E3).
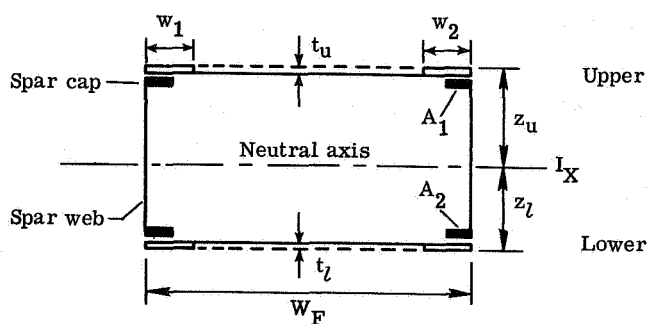
Sketch (E3)

The required moment of inertia I_X for the revised analytical model consists of two parts

$$I_X = I_c + I_s \tag{E11}$$

where I_c is the moment of inertia associated with in-plane bending of the spars about the neutral axis

$$I_c = A_1 z_u^2 + A_2 z_l^2$$

and where I_s is the moment of inertia of the wing cover skins effective in compression

$$I_s = W\left(t_u z_u^2 + t_l z_l^2\right)$$

The areas A_1 and A_2 contain the top and bottom spar-cap areas plus their associated 1/6 web areas (in accordance with ref. 35), and W is the effective skin width $\sum w_i$ where w_i is the effective skin width to one side of a spar. With I_X obtained from equation (E10) and I_c known from cross-sectional geometry, the only unknown equation (E11) is W, which may be expressed as

$$W = \frac{I_s}{t_u z_u^2 + t_l z_l^2} = \frac{I_X - I_c}{t_u z_u^2 + t_l z_l^2} \tag{E12}$$

Knowing W and the number of caps present in the cross section, w_i for each cap can be found and the reduced skin area $w_i t$ can be input into the analysis. The portion of skin effective in a section is given by

$$\frac{W}{W_F} = \frac{t_u W}{t_u W_F} = \frac{t_l W}{t_l W_F} = \frac{A}{A_{total}} \tag{E13}$$

where A is the effective skin area and A_{total} is the total skin area.

59

APPENDIX E

For the spanwise stations checked, the percent of skin effective was found to vary only slightly from 76.5 to 81.3 and averaged 80 percent. The wing was then modeled using shear panels and rods which included 80 percent of the skin areas and the total spar-cap areas. Minimal rods were again used for stability around panel edges not bounded by existing rib- or spar-cap rods. Rib-cap areas were arbitrarily sized using the 80-percent ratio. This method was used on model RS2 and gave the best static deflection correlation with test, as shown in figure 49.

The panel effectiveness in direct stress for the wing is indicated for models RS1 and RS2 in table X in the wing-tip row. In model RS1, only the carry-through structure panels were reduced for the wing, and the panels outboard of the fuselage were fully effective as in the original analysis. As in the case of the revised fuselage for this model, the wing carry-through panels were also arbitrarily modeled by the 1/6-area criterion of reference 35, with 1/6 of the web areas lumped in the top-and-bottom spar-cap areas for a 33-percent panel effectiveness. The deflection curve for this model in figure 49 shows that the desired wing-tip deflection was obtained with only this inboard part of the wing structure reduced in stiffness. Since both outer wing and its carry-through structure were of the same type of construction, a uniform reduction was needed for both parts to be more effective than 33 percent, i.e., if 1/6 of the panel area had been used for the outer wing as well as for the carry through, the desired deflection would have exceeded the test value. With available static test data, it was possible to find the percent skin effective in the test model and verify this percentage in an analytical model. This was done for model RS2, as described in the foregoing paragraphs, and resulted in a tip deflection within 2 percent of the test value.

Model Evaluation in Direct Stress

Table X provides a summary of static deflection results for several analytical symmetric models. The degree of flexibility of these models over the original is apparent from the table, but, it is difficult to judge from these data alone as to which of the two models, RS1 or RS2, yields the best deflection results. However, the static deflection curves in figures 47 to 49 show that correlation between static test and analysis of the fuselage and wing was best for analytical model RS2.

Panel Effectiveness in Shear

In addition to investigating the effectiveness of flat imperfect panels in direct stress, modifications were also introduced in an effort to account for reduced in-plane shear effectiveness. This was accomplished in three steps. The first two steps apply to rod-shear panel models whereas the third step involves a reduced membrane panel model.

60

APPENDIX E

In the first step, it was assumed that the effectiveness in shear would be the same as in direct stress. The resulting effect on static deformation is noted by comparing models RS4 with RS2 in table X. All panels of RS2 are fully effective in shear, whereas in model RS4 panel thicknesses are reduced so that the shear effectiveness was 46 percent for the fuselage cargo-bay region and 80 percent for the wing. Deflections for loads at the midfuselage increased 20 percent due to added shear effects; however, the increase was less than 10 percent for other loading conditions. The fin deflection should not be considered in the comparison because of the changes in the fin-root flexibility representation from F1 to F2. Vibration analysis using model RS4 resulted in eigenvalues much closer to the measured values than the original model but still somewhat high (see table XVI(a).

As a second step in evaluating effectiveness in shear, all panels including those in the fuselage were assumed 80-percent effective. The resulting deflections are listed under model RS5 in table X. The midfuselage value is now within 5 percent of the corresponding value for model RS2. Similar comparisons for loads at the fuselage nose and cabin ballast are not valid because a required constraint relationship at the junction of the cabin and fuselage longeron which had been inadvertently omitted in previous models was now added. The resulting change in deflection was not considered large enough to require rerunning the large computer programs for the other models. The deflections along the length of the fuselage are shown in figure 48 for midfuselage load. Model RS5 is slightly more flexible than the physical model (i.e., analytical deflections higher than measured deflections), and the shear effect is not significant for this static loading. Vibration analysis of this model resulted in frequencies still about 7 to 10 percent higher than measured values as shown in table XVI(a).

In order to determine the separate sensitivities of the fuselage and wings to panel imperfections, a vibration analysis was made with fuselage skin in the payload-bay area fully effective in direct stress and shear but with the wing panels 80-percent effective. This model is designated RS3 in table XVI(a), and, as can be seen, there are negligible changes in all but the second frequency, which is a predominant wing-bending frequency. For this mode, modifications to the wing panel effectiveness resulted in a 5-percent frequency reduction. Comparison of these frequencies with those of model RS5 indicates the wing to be far less affected by panel imperfections than the fuselage.

The third step in accounting for in-plane shear effectiveness involved returning to the membrane panel representation and modifying it in accordance with results from separate panel effectiveness studies. In contrast to the rod-shear panel model, in-plane shear effectiveness in the membrane model cannot be different from direct-stress effectiveness. Work at GAC (ref. 21, vol. II) based on a nonlinear analysis indicated

that for panels typical of the fuselage with imperfections on the order of 1.75 times the panel thickness a direct stress effectiveness of about 0.55 would be representative of the model. Tests on a simplified panel model described in the subsequent section indicated an effectiveness of about 0.5. Additional studies at LRC based on an elastic finite-element analysis gave a value of 0.63 for panel effectiveness. It was decided that a direct stress effectiveness value of 0.6 would be representative of the panel aspect ratios and initial imperfections found in most places on the model. Moreover, as discussed in reference 21, vol. II, the available information on shear indicated effectiveness values, both of 0.6 and 2/3.

Model Evaluation in Direct Stress and Shear

The 0.6-effectiveness value was used for models RM1 and RM2. Thicknesses of all exterior membrane panels in the fuselage, wings, and wing cover panels were uniformly reduced to 0.6 their original values. In model RM2, this thickness reduction was extended to membrane panels in the cargo-bay doors. The deflections of model RM1 under most static loads were higher than measured values, as may be noted from figures 48 and 49 and from table X. However, the model deflects less than the measured values at key significant locations; namely, the payload and cabin ballast where most of the weight is located. For that reason, the frequencies obtained from the vibration analysis shown in table VI are still higher than those measured. This difficulty of having the model too flexible for some static loads, yet higher in frequency, indicated that additional corrections were required. This observation can be drawn from comparison of the analytical and measured mode shapes in figures 12 to 15 and 26 to 29. However, since the revised model was considered close enough to the measured values to be adequate for appropriately combining the orbiter with the external tank and solid rocket boosters (e.g., by some modal coupling) and because of other higher priority work involving these other two shuttle elements, it was decided to forego any further modifications. An independent effort at modifying the model was continued at GAC (see ref. 21) where some of the anomalies were resolved.

The same membrane modifications were also made for the antisymmetric model, and static deflections for model RM1 are compared with those for the original analytical model and with measured deflections in table XI for four antisymmetric loadings. Frequencies are compared with initial analytical and measured frequencies in table XVI(b) and are generally in better agreement with measured frequencies, as are those of model RS6. Extending the 60-percent panel effectiveness for model RM1 to membrane panels in the door (model RM2) resulted in a negligible increase in flexibility and a negligible decrease in frequency. In general, the 0.6-effectiveness factor introduced sufficient flexibility into the original analytical model to significantly improve its agreement with the physical model but, in contrast to the symmetric model, not so much as

to make the analytical model more flexible than the physical model. This was true with doors on or off except for the midfuselage lateral load, for which the doors-on case of the revised analytical model was more flexible than the corresponding physical model.

PANEL EFFECTIVENESS DETERMINED FROM INDEPENDENT STUDIES

Murray Bernstein* and John L. Sewall, Coordinators

Independent studies that guided the choice of the panel effectiveness factor for the reduced membrane models (RM1 and RM2) are described in the following sections. These studies consisted of an analytical investigation at GAC and tests and analysis of a simple reinforced panel model at LRC.

Theoretical Criteria

The work reported in reference 21 involved calculating the effective panel width under direct stress loading for panels of aspect ratios and load intensities representative of the fuselage and wing. Timoshenko's equations were used for plates simply supported along the side and axially loaded along the ends. The displacement functions and assumed initial bow were similar to those in reference 30, and the range of maximum displacement of the initial bow is extended to twice the panel thickness. The method of solution involved writing the expression for potential energy in terms of the displacements and initial imperfections, determining the minimum value of potential energy with respect to the displacements, and solving for the strain and stress distributions. The stress distribution was then integrated to get the panel load and effective width. Typical analytical results for three panels are shown in figure 50.

These calculations showed that for panels with aspect ratios of 1.32, which are typical of the bottom of the fuselage, the effectiveness varies from 0.9 for maximum displacement of the initial bow of 1/4 thickness to 0.5 for twice the panel thickness at low load levels, as indicated from the inset plot of figure 50(a). Similar calculations for panels of 1.79 aspect ratio typical of the side wall, showed effectiveness to vary from 0.72 for 1/4 thickness initial bow to 0.47 for twice the thickness. The wing panels, which have aspect ratios of 0.54, were very effective even with maximum displacement of the initial bow up to twice the thickness. This work was not extended to shear and bending.

However, work in references 36 and 37 indicated that an effectiveness of 2/3 in shear would be applicable. This was reinforced by data from previously unreported tests of riveted panels at GAC in which the data, although widely scattered, indicated an average effectiveness of about 0.6 in shear.

---

* Grumman Aerospace Corporation.

APPENDIX E

INVESTIGATION OF THE EFFECTS OF PANEL IMPERFECTIONS
ON A SIMPLIFIED MODEL

Robert W. Herr and James C. Robinson

Apparatus.- To gain some insight into the effects of panel imperfections on fuse-
lage bending frequencies, the simplified model illustrated in figure 51 was fabricated.
The six-bay model consists of a 0.51 mm (0.020 in.) aluminum panel specially selected
for flatness, clamped between two frames of 1.02 by 19 mm (0.040 by 0.75 in.) alumi-
num angle. The aspect ratio of each of the six bays (1.56) is representative of the aspect
ratios of the 1/8-scale orbiter fuselage. Number 4 machine screws were used to clamp
the panel between the frames and were spaced every 20 mm (0.79 in.) along the longerons
and 19 mm (0.75 in.) along crosswise stiffeners. Panel imperfections were simulated by
first loosening all of the clamping screws, then, with the frame lying on a flat surface, a
distributed load was applied normal to the panel, one bay at a time, while the screws
surrounding the bay were tightened. Upon removal of the static load, most of the static
deflection remained. Adjacent bays were loaded in opposite directions. The nominal
amount of deformation was dependent upon the magnitude of the distributed load. The
procedure is approximate, of course, and the maximum simulated imperfection will vary
somewhat from bay to bay; upon loosening of the machine screws, the panel always
returned to its original flat state.

For vibration tests, the panel model was oriented vertically with its upper end
cantilevered. A 5 kg (0.0285 lb-sec^2/in.) mass was clamped to the free end. To facili-
tate the cantilever mounting and the attachment of the tip mass, the 0.51 mm (0.020 in.)
panel extended 5.08 cm (2.0 in.) beyond the frame at each end.

A small vibration exciter attached to the tip mass was used to excite the in-plane
bending and the axial vibration modes.

Analysis.- The effect of panel imperfections on the axial and bending stiffnesses
of the structure shown in figure 51 was studied analytically using the statics version of
the Structural Network Analysis Program (SNAP/STATICS, ref. 38). One average length
bay of the beam measuring 38.1 cm deep by 2.44 cm long (15.0 by 9.625 in.) was modeled
using triangular elements with both membrane and bending stiffnesses for the web and
offset beam elements for the stiffeners. The model had a total of 160 grid points. A
deformed shape of $w_0[1 - \cos f(x) \cos f(y)]$ was used for the panel imperfection. The
resulting stiffnesses are for small displacements and low load levels inasmuch as the
analysis does not consider the possibility of buckling.

The effects of these stiffness reductions on natural modes and frequencies were
calculated using the SPAR computer program (ref. 39) which is an improved version

of SNAP. A simple cantilevered-beam math model having 10 grid points was used to determine the lower natural frequencies and mode shapes.

Results.- Panel imperfections ranging from 1.75 to 4 times the panel thickness caused the following computed reductions in the total stiffness (panel and stiffeners) of the simplified model:

Panel imperfection		Total stiffness reduction, percent			Panel effectiveness, axial
w_o, mm (in.)	w_o/t	Bending	Shear	Axial	
0.9 (0.035)	1.75	3	6	22	0.63
1.4 (.055)	2.75	5	12	28	.53
2.0 (.080)	4.0	8	22	32	.48

The panel imperfections investigated are seen to have only a minor effect on the model bending stiffness but a significant effect on the axial stiffness, with the effects on shearing stiffness falling in between. The effectiveness of an imperfect 0.51 mm (0.020 in.) panel (relative to a flat panel) in resisting axial loads is given in the last column and was obtained by subtracting the longeron stiffness from the computed axial stiffness of the complete model. The panel effectiveness is seen to range from 0.63 to 0.48 for panel imperfections between 1.75 and 4.0 times the panel thickness.

The analytical and experimentally determined in-plane bending frequencies of the simplified panel model are as follows for the given values of initial panel imperfection:

Panel imperfection		Bending frequency, Hz		Frequency reduction, percent	
w_o, mm (in.)	w_o/t	Experimental	Analysis	Experimental	Analysis
0 (0)	0	41.4	44.7	0	0
.9 (.035)	1.75	40.3	44.1	2.6	1.3
1.4 (.055)	2.75	39.2	43.5	5.3	2.8
2.0 (.080)	4.0	38.6	42.9	6.8	4.0

The reduction in the in-plane bending frequency due to panel imperfection is seen to be quite small. This result is not surprising as the major out-of-plane panel imperfection lies near the neutral bending axis.

For fuselage bending vibrations in the pitch plane, imperfections in the fuselage bottom panel would be expected to have a greater effect on the resonant frequencies since the entire panel area is in direct stress at a maximum distance from the neutral

axis. This effect is indicated in the following table in which the fundamental axial frequency of the simplified panel model is shown for various panel imperfections:

Panel imperfection			Axial frequency, Hz		Frequency reduction, percent	
w_o, mm (in.)		w_o/t	Experimental	Analysis	Experimental	Analysis
0	(0)	0	247	279	0	0
.9	(.035)	1.75	196	250	21	10
1.4	(.055)	2.75		240		14
2.0	(.080)	4.0		232		17

The analytical results show a substantial reduction in the axial frequency for the range of panel imperfections investigated, 10 percent for imperfections 1.75 times the panel thickness to 17 percent for imperfections 4 times the panel thickness. Unfortunately, the experimental results are not definitive, due to coupling between the desired mode and the higher panel modes. In figure 52 the axial acceleration of the 5 kg $\left(0.0285 \text{ lb-sec}^2/\text{in.}\right)$ tip mass is plotted as a function of the excitation frequency for different amounts of panel imperfection. For the undeformed panel (fig. 52(a)) a relatively clean, well-defined resonance is observed at a frequency of 247 Hz. In figure 52(b) it is seen that for a nominal panel imperfection of 0.9 mm (0.035 in.) the frequency of the fundamental axial mode is 196 Hz, a reduction of 21 percent from the flat-panel frequency. For larger panel imperfections (figs. 52(c) and 52(d)), the out-of-plane vibration modes of the panels become so strongly coupled with the axial motion that it is impossible to isolate the desired axial vibration mode.

The 21-percent reduction in the experimental axial frequency attributable to 0.9 mm (0.035 in.) imperfection corresponds to 37-percent reduction in the axial stiffness as compared with a computed 20-percent reduction in axial stiffness. If the longitudinal stiffeners are assumed 100-percent effective, the approximate effectiveness of the panel in carrying axial loads is given by

$$\text{Panel effectiveness} = \frac{\left(A_L + A_p\right)\left(\frac{f}{f_o}\right)^2 - A_L}{A_p} \tag{E14}$$

where the cross-sectional area of longerons, $A_L = 1.45 \text{ cm}^2 \left(0.224 \text{ in}^2\right)$, the cross-sectional area of panel, $A_p = 1.93 \text{ cm}^2 \left(0.3 \text{ in}^2\right)$, the fundamental axial frequency of flat panel model, $f_o = 247$ Hz, and the fundamental axial frequency of imperfect panel model, $f = 196$ Hz. Substitution of these values into equation (E14) yields a panel effectiveness of only 0.34 compared with a computed value of 0.66. The cause of the large spread between the experimentally and analytically determined values of direct-stress

panel effectiveness is not immediately obvious, although there are reasons to believe that the true value probably lies between the two extremes.

The 100-percent effectiveness of the longerons (or stiffeners) is a questionable assumption since the longerons do not connect directly to either the tip mass or the backstop. On the other hand, carry through of loads at the panel ends should be very effective since axial extensions of the panel are clamped firmly to the tip mass and backstop. This would suggest that most of the discrepancy between experimental and analytical axial frequencies of the panel model with no panel imperfections (247 Hz and 279 Hz, respectively) is attributable to poor longeron carry-through structure. With the assumption of 100-percent effectiveness for the undeformed panel, the effectiveness of the longerons is given by

$$\text{Longeron effectiveness} = \frac{\left(A_L + A_p\right)\left(\frac{f}{f_0}\right)^2 - A_p}{A_L} \tag{E15}$$

where in this case f and f_0 are, respectively, the experimental and analytical axial frequencies of the panel model with no imperfections. Entering the appropriate values into equation (E15) results in a longeron effectiveness of 0.49. The effective-longeron area is thus reduced from 1.45 cm^2 $\left(0.224 \text{ in}^2\right)$ to 0.71 cm^2 $\left(0.11 \text{ in}^2\right)$. Recalculation of the deformed-panel effectiveness using this reduced effective area of the longerons indicates an approximate panel effectiveness of 0.49. This value of panel effectiveness is in good agreement with results interpolated from the GAC nonlinear analysis (ref. 21) for a panel aspect ratio of 1.56 and an imperfection 1.75 times the panel thickness. The more sophisticated nonlinear analysis by GAC would be expected to predict the imperfect panel effectiveness more accurately than the linear SNAP analysis.

CONCLUDING REMARKS

Murray Bernstein[*] and John L. Sewall, Coordinators

The estimate of direct stress capability based on 1/6 the web (shear panel) area lumped to the caps (longerons), which amounts to a 33-percent-effective skin, yielded results that are too flexible as evidenced by model RS1. A more valid procedure by which the moments of inertia in the analytical model are reduced yielded model RS2. This method required the use of static test data. Model RS2 has a 46-percent-effective skin fuselage and an 80-percent-effective skin wing in direct stress and correlates well with static test.

---

[*]Grumman Aerospace Corporation.

APPENDIX E

Comparison of the rod and shear panel models RS4 and RS5 shows an increase in static deflection at the midfuselage with decreasing shear effectiveness. Vibration analyses of these models resulted in an increase in frequency with increasing shear effectiveness. Model RS4 exhibited frequencies closer to measured values but still somewhat higher.

The membrane panel model RM1 was determined to have an effectiveness of about 0.6 in both direct stress and shear. While model RM1 clearly gives the best frequency and mode-shape correlation, the comparison with static test data is not so good as other static deflection models.

REFERENCES

1. Mixson, John S.; Catherine, John J.; and Arman, Ali: Investigation of the Lateral Vibration Characteristics of a 1/5-Scale Model of Saturn SA-1. NASA TN D-1593, 1963.

2. Runyan, H. L.; Morgan, H. G.; and Mixson, J. S.: Use of Dynamic Models in Launch-Vehicle Development. AGARD Rep. 479, May 1964.

3. Mixson, John S.; and Catherine, John J.: Comparison of Experimental Vibration Characteristics Obtained From a 1/5-Scale Model and From a Full-Scale Saturn SA-1. NASA TN D-2215, 1964.

4. Mixson, John S.; and Catherine, John J.: Experimental Lateral Vibration Characteristics of a 1/5-Scale Model of Saturn SA-1 With an Eight-Cable Suspension System. NASA TN D-2214, 1964.

5. Catherine, John J.: Torsional Vibration Characteristics of a 1/5-Scale Model of Saturn SA-1. NASA TN D-2745, 1965.

6. Thompson, William M., Jr.: An Investigation of the Response of a Scaled Model of a Liquid-Propellant Multistage Launch Vehicle to Longitudinal Excitation. NASA TN D-3975, 1967.

7. Jaszlics, Ivan J.; and Morosow, George: Dynamic Testing of a 20% Scale Model of the Titan III. AIAA Symposium on Structural Dynamics and Aeroelasticity, Aug.-Sept. 1965, pp. 477-485.

8. Peele, Ellwood L.; Thompson, William M., Jr.; and Pusey, Christine G.: A Theoretical and Experimental Investigation of the Three-Dimensional Vibration Characteristics of a Scaled Model of an Asymmetrical Launch Vehicle. NASA TN D-4707, 1968.

9. Leadbetter, Sumner A.; Leonard, H. Wayne; and Brock, E. John, Jr.: Design and Fabrication Considerations for a 1/10-Scale Replica Model of the Apollo/Saturn V. NASA TN D-4138, 1967.

10. Peele, Ellwood L.; Leonard, H. Wayne; and Leadbetter, Sumner A.: Lateral Vibration Characteristics of the 1/10-Scale Apollo/Saturn V Replica Model. NASA TN D-5778, 1970.

11. Vehicle Dynamics Group: 1/10-Scale Saturn V Model Structural Dynamic Analysis. Doc. No. D5-15631 A (Contract No. NAS8-5608), Boeing Co., May 1, 1967.

12. Pinson, Larry D.; Leonard, H. Wayne; and Raney, John P.: Analyses of the Longitudinal Dynamics of Launch Vehicles With Application to a 1/10-Scale Saturn V Model. J. Spacecraft Rockets, vol. 5, no. 3, Mar. 1968, pp. 303-308.

13. Pinson, Larry D.; and Leonard H. Wayne: Longitudinal Vibration Characteristics of 1/10-Scale Apollo/Saturn V Replica Model. NASA TN D-5159, 1969.

14. Pinson, Larry D.: Evaluation of a Finite-Element Analysis for Longitudinal Vibrations of Liquid-Propellant Launch Vehicles. NASA TN D-5803, 1970.

15. Grimes, P. J.; McTigue, L. D.; Riley, G. F.; and Tilden, D. I.: Advancements in Structural Dynamic Technology Resulting From Saturn V Programs. Volume I. NASA CR-1539, 1970.

16. Grimes, P. J.; McTigue, L. D.; Riley, G. F.; and Tilden, D. I.: Advancements in Structural Dynamic Technology Resulting From Saturn V Programs. Volume II. NASA CR-1540, 1970.

17. Leadbetter, Sumner A., coordinator: Application of Analysis and Models to Structural Dynamic Problems Related to the Apollo-Saturn V Launch Vehicle. NASA TN D-5831, 1970.

18. Leadbetter, Sumner A.; and Kiefling, Larry A.: Recent Studies of Space Shuttle Multibody Dynamics. NASA Space Shuttle Technology Conference. Vol. III, NASA TM X-2274, 1971, pp. 1-25.

19. Thornton, E. A.: Vibration Analysis of a 1/15 Scale Dynamic Model of a Space Shuttle Configuration. Grant No. NAS 1-9434-20, Old Dominion Univ., [1972]. (Available as NASA CR-111984.)

20. Grumman Aerospace Corp.: Design of a Space Shuttle Structural Dynamics Model. NASA CR-112205.

21. Mason, P. W.; Harris, H. G.; Zalesak, J.; and Bernstein, M.: Analytical and Experimental Investigation of a 1/8-Scale Dynamic Model of the Shuttle Orbiter. 1974.
    Volume I – Summary Report. NASA CR-132488.
    Volume II – Technical Report. NASA CR-132489.
    Volume IIIA – Supporting Data. NASA CR-132490.
    Volume IIIB – Supporting Data. NASA CR-132491.

22. Grumman Aerospace Corp.: Preliminary Shuttle Structural Dynamics Modeling Design Study. NASA CR-112196, 1972.

23. Kennedy, Charles C.; and Pancu, C. D. P.: Use of Vectors in Vibration Measurement and Analysis. J. Aeronaut. Sci., vol. 14, no. 11, Nov. 1947, pp. 603-625.

24. Mead, D. J.: The Internal Damping Due to Structural Joints and Techniques for General Damping Measurement. C.P. No. 452, British A.R.C., 1959.

25. McCormick, Caleb W., ed.: The NASTRAN User's Manual (Level 15.0). NASA SP-222(01), May 1973.

26. Bernstein, Murray; Mason, Philip W.; Zalesak, Joseph; Gregory, David J.; and Levy, Alvin: NASTRAN Analysis of the 1/8-Scale Space Shuttle Dynamic Model. NASTRAN: Users' Experiences, NASA TM X-2893, 1973, pp. 169-241.

27. Guyan, Robert J.: Reduction of Stiffness and Mass Matrices. AIAA J., vol. 3, no. 2, Feb. 1965, p. 380.

28. Everstine, Gordon C.: The BANDIT Computer Program for the Reduction of Matrix Bandwidth for NASTRAN. Rep. 3827, Naval Ship Res. & Develop. Center, Mar. 1972.

29. Haggenmacher, Gernot W.: Some Aspects of NASTRAN Solution Accuracy. NASTRAN: Users' Experiences, NASA TM X-2378, 1971, pp. 47-63.

30. Hu, Pai C.; Lundquist, Eugene E.; and Batdorf, S. B.: Effect of Small Deviations From Flatness on Effective Width and Buckling of Plates in Compression. NACA TN 1124, 1946.

31. The NASTRAN Programmer's Manual (Level 15.5). NASA SP-223(01), 1973.

32. MacNeal, Richard H., ed.: The NASTRAN Theoretical Manual (Level 15). NASA SP-221(01), 1972.

33. Chajes, Alexander; and Winter, George: Torsional-Flexural Buckling of Thin-Walled Members. J. Struct. Div., American Soc. Civil Eng., vol. 91, no. ST4, Aug. 1965, pp. 103-124.

34. Zienkiewicz, O. C.: The Finite Element Method in Engineering Science. McGraw-Hill Book Co., Inc., c.1971, pp. 154-155.

35. Kuhn, Paul: Stresses in Aircraft and Shell Structures. McGraw-Hill Book Co., Inc., 1956, pp. 47-100.

36. Stein, Manuel; and Starnes, James H., Jr.: Numerical Analysis of Stiffened Shear Webs in the Postbuckling Range. Numerical Solution of Nonlinear Structural Problems, R. F. Hartung, ed., AMD-Vol. 6, American Soc. Mech. Eng., c.1973, pp. 211-223.

37. Tsongas, Alexander G.; and Ratay, Robert T.: Investigation of Diagonal-Tension Beams With Very Thin Stiffened Webs. NASA CR-101854, 1969.

38. Whetstone, W. D.: Structural Network Analysis Program – User's Manual. Static Analysis Version V70E. LMSC-HREC D162812. Lockheed Missiles & Space Co., Dec. 14, 1970.

39. Whetstone, W. D.: SPAR Reference Manual. LMSC D403168 (Contract No. NAS 8-26352), Lockheed Missiles & Space Co., June 1974.

TABLE I.- PERTINENT SCALING RELATIONSHIPS FOR 1/8-SCALE MODEL[a]

Physical quantity	Magnitude
Length, L, and displacements	$\dfrac{L_m}{L_p} = \dfrac{1}{8}$
Poisson's ratio, ν	$\nu_m = \nu_p$
Mass density, ρ	$\rho_m = \rho_p$
Modulus of elasticity, E	$\dfrac{E_m}{E_p} = 1$
Strain, ϵ	$\epsilon_m = \epsilon_p$
Area, A	$\dfrac{A_m}{A_p} = \left(\dfrac{1}{8}\right)^2$
Area moment of inertia, I	$\dfrac{I_m}{I_p} = \left(\dfrac{1}{8}\right)^4$
Mass moment of inertia, I'	$\dfrac{I_m'}{I_p'} = \left(\dfrac{1}{8}\right)^5$
Stress, σ	$\sigma_m = \sigma_p$
Force, F	$\dfrac{F_m}{F_p} = \left(\dfrac{1}{8}\right)^2$
Longitudinal stiffness, EA	$\dfrac{(EA)_m}{(EA)_p} = \left(\dfrac{1}{8}\right)^2$
Bending stiffness, EI	$\dfrac{(EI)_m}{(EI)_p} = \left(\dfrac{1}{8}\right)^4$
Torsional stiffness, GJ	$\dfrac{(GJ)_m}{(GJ)_p} = \left(\dfrac{1}{8}\right)^4$
Weight, W	$\dfrac{W_m}{W_p} = \left(\dfrac{1}{8}\right)^3$
Acceleration, a	$\dfrac{a_m}{a_p} = \dfrac{8}{1}$
Natural frequency, ω	$\dfrac{\omega_m}{\omega_p} = \dfrac{8}{1}$

[a] Subscript m refers to model; subscript p refers to prototype.

TABLE II.- MEASURED AND INITIAL ANALYTICAL MODE FREQUENCIES OF

A 1/8-SCALE ORBITER MODEL

Mode	Frequency, Hz		Description of mode shape
	Experiment	Initial analysis	
Symmetric mode			
1	43.6	53.2	Fuselage first bending $(c/c_{cr} = 0.0088)$
2	51.6	62.6	Wing first vertical bending
3	57.9	75.2	Payload, fore-and-aft
4	79.9	108.5	Fin, fore-and-aft
5	95.7	----	Payload pitch
6	104.1	133.8	Wing first torsion
7	107.0	156.4	Fuselage second bending
Antisymmetric mode			
1	42.0	52.9	Orbiter first lateral bending, fin lateral bending
2	51.2	72.6	Wing first bending, fin lateral bending
3	----	85.1	Wing bending coupled with fuselage-payload and fin lateral bending
4	----	92.0	Fuselage lateral bending and aft orbiter yaw and roll
5	93.4	101.5	Fuselage lateral bending, payload yaw, and orbiter torsion

TABLE III.- FIRST MODE NATURAL FREQUENCIES

WITH STATIC PRELOAD

Preload		First mode frequency, Hz
N	lb	
0	0	43.7
890	200	43.9
1780	400	44.1
2670	600	44.3

TABLE IV.- ORBITER RUN STATISTICS

(a) Static analysis

	Symmetric	Antisymmetric
Field length, octal words	300 000	300 000
CPU time for typical run, sec	2 800	2 750
Number of runs	8	4

(b) Dynamic analysis

Phase I substructure	Field length, octal words	CPU time per run, sec	Number of runs	
			Symmetric	Antisymmetric
Fuselage	250 000	2680	9	1
Wing	160 000	760	6	1
Door	160 000	270	2	1
Fin	140 000	160	9	2
Payload	160 000	85	1	1
Tape copy	160 000	60	9	1
Phase II orbiter	300 000	3850	9	1

TABLE V.- ORBITER HALF-MODEL STATISTICS

[From ref. 21, vol. I]

| Phase I substructure | Grid points | Elements | | | | | | | Degrees of freedom | | | |
| | | Bar | Membrane | | Plate | Shear panel | Rod | Total elements | Symmetric model | | Antisymmetric model | |
			Quadrilateral	Triangular					After SPC and MPC	After Guyan reduction	After SPC and MPC	After Guyan reduction
Fuselage	537	93	336	7		172	616	1224	1417	246	1368	222
Wing	192		149	8		81	187	425	531	183	531	183
Door	134	9	20		16	64	178	287	396	26	384	26
Fin	59		24			22	65	111	101	25	99	24
Payload	12	8						8	24	24	26	26
Total	934	110	529	15	16	339	1046	2055	2469	504	2408	481
Phase II orbiter	215		125 PLOTEL						400	339	378	324

75

TABLE VI.- MEASURED AND BEST ANALYTICAL ORBITER FREQUENCIES

(a) Symmetric mode

Mode	Frequency, Hz		
	Measured	Analytical	
		Model RM1	Model RS6
1	43.6	44.2	44.2
2	51.6	53.6	54.4
3	57.9	64.4	63.0
4	79.9	84.2	80.2

(b) Antisymmetric mode

Mode	Frequency, Hz		
	Measured	Analytical	
		Model RM1	Model RS6
1	42.0	44.5	42.2
2	51.2	54.3	57.0
3	(a)	67.4	58.6
4	(a)	77.8	78.9
5	93.4	88.7	71.6

a Not found.

TABLE VII.- ANTISYMMETRIC MODES WITHOUT DOORS

(a) Fuselage (NASTRAN, phase I)

Mode	Frequency, Hz			Mode shape description
	Initial analysis (a)	Model RM1	Model RS6 (a)	
1	28.8	24.4	25.1	First torsion, predominantly in the cabin
2	89.1	75.4	73.8	First lateral bending
3	128.3	111.7	110.0	Coupled lateral bending and torsion

(b) Orbiter

Mode	Frequency, Hz	
	Measured	Analytical (b)
1	c 27.0	c 23.7
2	(d)	46.5
3	(d)	57.5
4	(d)	69.3
5	(d)	79.6
6	(d)	101.8

a From reference 21, vols. II, IIIA, and IIIB.
b Model RM1.
c First torsion, predominantly in cabin.
d Not investigated.

TABLE VIII.- DEFLECTION MEASUREMENT ACCURACY

133.45 N (30 lb) each

Simultaneous loads applied (19 on-off cycles)
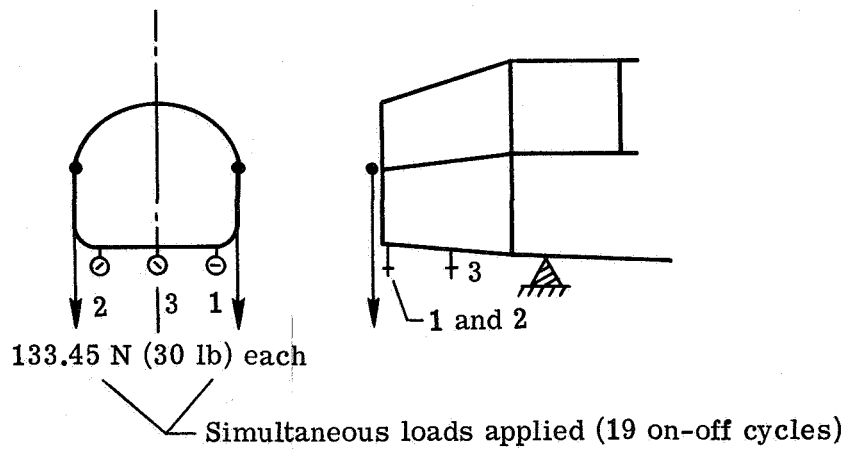
Dial indicator	Average deflection		Standard deviation		3-sigma deviation		
	μm	in.	μm	in.	μm	in.	Percent
1	117.22	4.615×10^{-3}	2.99	0.118×10^{-3}	8.99	0.354×10^{-3}	7.7
2	121.18	4.771	4.14	.163	12.40	.488	10.2
3	70.69	2.783	3.02	.119	9.04	.356	12.8

TABLE IX.- SUMMARY OF EXPERIMENTAL LOAD-POINT STATIC DEFLECTIONS

| Load application points | | Static deflection, μm/N (in/lb) | | | |
| | | Initial analysis | | Measured | |
Number in figure 37	Location	Doors off	Doors on	Doors off	Doors on
		Symmetric loading			
3	Midfuselage	0.214 (37.4 $\times 10^{-6}$)	0.176 (30.9 $\times 10^{-6}$)	0.236 (41.3 $\times 10^{-6}$)	0.234 (41.0 $\times 10^{-6}$)
1	Fuselage nose	.316 (55.4 $\times 10^{-6}$)	.296 (51.8 $\times 10^{-6}$)	.459 (80.3 $\times 10^{-6}$)	(a)
5	Wing tip	1.661 (290.8 $\times 10^{-6}$)	1.661 (290.8 $\times 10^{-6}$)	2.033 (356.0 $\times 10^{-6}$)	2.037 (356.8 $\times 10^{-6}$)
7	Fin ballast	1.067 (186.8 $\times 10^{-6}$)	1.067 (186.8 $\times 10^{-6}$)	2.056 (360.0 $\times 10^{-6}$)	2.106 (368.9 $\times 10^{-6}$)
6	OPS ballast	.193 (33.8 $\times 10^{-6}$)	.171 (30.0 $\times 10^{-6}$)	.211 (37.0 $\times 10^{-6}$)	(a)
4	Payload	.158 (27.6 $\times 10^{-6}$)	.154 (27.0 $\times 10^{-6}$)	.206 (36.0 $\times 10^{-6}$)	(a)
2	Cabin ballast	.183 (32.0 $\times 10^{-6}$)	.175 (30.7 $\times 10^{-6}$)	.240 (42.0 $\times 10^{-6}$)	(a)
		Antisymmetric loading			
2	Midfuselage	0.232 (40.7 $\times 10^{-6}$)	0.226 (39.5 $\times 10^{-6}$)	0.364 (63.8 $\times 10^{-6}$)	0.302 (52.9 $\times 10^{-6}$)
4	Fin ballast	3.260 (571.0 $\times 10^{-6}$)	1.621 (283.8 $\times 10^{-6}$)	3.969 (695.0 $\times 10^{-6}$)	(a)
1	Fuselage nose	b.76 (3.40 $\times 10^{-6}$)	b.26 (1.17 $\times 10^{-6}$)	b2.09 (9.30 $\times 10^{-6}$)	b.44 (1.94 $\times 10^{-6}$)
3	Wing tip	b1.21 (5.40 $\times 10^{-6}$)	b1.21 (5.39 $\times 10^{-6}$)	b2.47 (11.0 $\times 10^{-6}$)	b2.38 (10.6 $\times 10^{-6}$)

a Not investigated.

b Units are μm/μm-N (in/in-lb).

78

TABLE X.- STATIC DEFLECTIONS FOR SYMMETRIC LOADING

| Load application points | | Static deflection, μm/N (in/lb) | | | | | | | | | |
| Number in figure 37(a) | Location | Initial analysis | | RS1 | RS2 | RS4 | RS5 | RM1 | RM2 | Measured | |
		Doors off	Doors on							Doors off	Doors on
3	Midfuselage	0.214 (37.4 × 10⁻⁶)	0.176 (30.9 × 10⁻⁶)	0.276 (48.4 × 10⁻⁶)	0.255 (44.7 × 10⁻⁶)	0.308 (54.0 × 10⁻⁶)	0.261 (45.7 × 10⁻⁶)	0.286 (50.1 × 10⁻⁶)	0.246 (43.0 × 10⁻⁶)	0.236 (41.3 × 10⁻⁶)	0.234 (41.0 × 10⁻⁶)
1	Fuselage nose	0.316 (55.4 × 10⁻⁶)	0.296 (51.8 × 10⁻⁶)	0.453 (79.3 × 10⁻⁶)	0.433 (75.8 × 10⁻⁶)	0.452 (79.1 × 10⁻⁶)	0.422 (73.9 × 10⁻⁶)	0.416 (72.8 × 10⁻⁶)	0.393 (68.8 × 10⁻⁶)	0.459 (80.3 × 10⁻⁶)	(a)
5	Wing tip	1.661 (290.8 × 10⁻⁶)	1.661 (290.8 × 10⁻⁶)	2.078 (363.9 × 10⁻⁶)	2.083 (364.7 × 10⁻⁶)	2.108 (369.2 × 10⁻⁶)	2.103 (368.2 × 10⁻⁶)	2.359 (413.1 × 10⁻⁶)	2.357 (412.8 × 10⁻⁶)	2.033 (356.0 × 10⁻⁶)	2.037 (356.8 × 10⁻⁶)
7	Fin ballast	1.067 (186.8 × 10⁻⁶)	1.067 (186.8 × 10⁻⁶)	2.556 (447.6 × 10⁻⁶)	2.483 (434.8 × 10⁻⁶)	1.915 (335.4 × 10⁻⁶)	1.878 (328.8 × 10⁻⁶)	2.253 (394.5 × 10⁻⁶)	2.177 (381.2 × 10⁻⁶)	2.056 (360.0 × 10⁻⁶)	2.107 (368.9 × 10⁻⁶)
6	OPS ballast	0.193 (33.8 × 10⁻⁶)	0.171 (30.0 × 10⁻⁶)	0.247 (43.2 × 10⁻⁶)	0.224 (39.2 × 10⁻⁶)	0.238 (41.7 × 10⁻⁶)	0.226 (39.6 × 10⁻⁶)	0.257 (45.0 × 10⁻⁶)	0.232 (40.7 × 10⁻⁶)	0.211 (37.0 × 10⁻⁶)	(a)
4	Payload	0.158 (27.6 × 10⁻⁶)	0.154 (27.0 × 10⁻⁶)	0.187 (32.7 × 10⁻⁶)	0.179 (31.4 × 10⁻⁶)	0.190 (33.2 × 10⁻⁶)	0.173 (30.3 × 10⁻⁶)	0.173 (30.3 × 10⁻⁶)	0.167 (29.3 × 10⁻⁶)	0.206 (36.0 × 10⁻⁶)	(a)
2	Cabin ballast	0.183 (32.0 × 10⁻⁶)	0.175 (30.7 × 10⁻⁶)	0.242 (42.4 × 10⁻⁶)	0.235 (41.1 × 10⁻⁶)	0.245 (42.9 × 10⁻⁶)	0.221 (38.7 × 10⁻⁶)	0.223 (39.0 × 10⁻⁶)	0.215 (37.6 × 10⁻⁶)	0.240 (42.0 × 10⁻⁶)	(a)

a Not investigated.

TABLE XI.- STATIC DEFLECTIONS FOR ANTISYMMETRIC LOADING

| Load application points | | Static deflection, μm/N (in/lb) | | | | | | |
| Number in figure 37(b) | Location | Initial analysis | | RM1 | | RM2, doors on | Measured | |
		Doors off	Doors on	Doors off	Doors on		Doors off	Doors on
2	Midfuselage	0.232 (40.7 × 10⁻⁶)	0.226 (39.5 × 10⁻⁶)	0.335 (58.6 × 10⁻⁶)	0.330 (57.7 × 10⁻⁶)	0.330 (57.7 × 10⁻⁶)	0.364 (63.8 × 10⁻⁶)	0.302 (52.9 × 10⁻⁶)
4	Fin ballast	3.260 (571.0 × 10⁻⁶)	1.621 (283.8 × 10⁻⁶)	3.804 (666.2 × 10⁻⁶)	3.794 (664.5 × 10⁻⁶)	3.795 (664.6 × 10⁻⁶)	3.969 (695.0 × 10⁻⁶)	(a)
1	Fuselage nose	b 0.76 (3.40 × 10⁻⁶)	b 0.26 (1.17 × 10⁻⁶)	b 0.81 (3.60 × 10⁻⁶)	b 0.32 (1.43 × 10⁻⁶)	b 0.34 (1.53 × 10⁻⁶)	b 2.09 (9.30 × 10⁻⁶)	b 0.44 (1.94 × 10⁻⁶)
3	Wing tip	b 1.21 (5.40 × 10⁻⁶)	b 1.21 (5.40 × 10⁻⁶)	b 1.66 (7.40 × 10⁻⁶)	b 1.65 (7.35 × 10⁻⁶)	b 1.65 (7.35 × 10⁻⁶)	b 2.47 (11.0 × 10⁻⁶)	b 2.38 (10.6 × 10⁻⁶)

a Not investigated.
b Units are μm/μm-N (in/in-lb).

TABLE XII.- JOINT FLEXIBILITY EFFECTS ON

ORBITER SYMMETRIC-MODE FREQUENCIES

Mode	Frequency, Hz		
	Measured	Analytical	
		Initial analysis	F2
1	43.6	53.2	51.9
2	51.6	62.6	63.4
3	57.9	75.2	72.55
4	79.9	108.5	91.8

TABLE XIII.- PROPERTIES OF SIMPLIFIED FUSELAGE MODEL

OF APPENDIX D

t_1 . . . . 0.051 cm (0.02 in.)

t_2 . . . . 0.0635 cm (0.025 in.)

t_3 . . . . 0.051 cm (0.02 in.)

b . . . . 0.3175 m (12.5 in.)

h_w . . . . 0.419 m (16.5 in.)

h_k . . . . 0.152 m (6 in.)

A_1 . . . . 0.645 cm^2 $\left(0.1 \text{ in}^2\right)$

A_2 . . . . 0.464 cm^2 $\left(0.072 \text{ in}^2\right)$

$A_3 = A_4$ . . . . 0.564 cm^2 $\left(0.0875 \text{ in}^2\right)$

E . . . . 72.4 GN/m^2 $\left(10.5 \times 10^6 \text{ lb/in}^2\right)$

ν 1/3

ℓ . . . . 2.46 m (97 in.)

TABLE XIV.- FREQUENCIES OF SIMPLIFIED FUSELAGE MODEL

OF APPENDIX D

Mode	Frequency, Hz, of –				
	Mathematical models		NASTRAN model		
	Bean solution (ref. 33)	Piecewise linear	Bending membrane		Membrane, coarse
			Coarse	Refined	
Symmetric, first vertical bending	87.6	77.8	82.3	78.5	(a)
Antisymmetric, first coupled transverse bending and torsion	53.1	51.8	54.9	51.1	54.9

[a] Not investigated.

TABLE XV.- EFFECT ON PHASE II ORBITER SYMMETRIC-MODE

FREQUENCIES OF REDUCED STIFFNESS

IN FUSELAGE SIDEWALLS

Mode	Frequency, Hz		
	Measured	Analytical	
		Initial analysis	Minimal rod-shear panel[a]
1	43.6	53.2	46.5
2	51.6	62.6	60.5
3	57.9	75.2	71.3
4	79.9	108.5	103.7

[a] Rods of minimal cross-sectional areas for panel stability.

TABLE XVI.- EFFECTS ON FREQUENCY OF VARIATIONS
IN PANEL EFFECTIVENESS

(a) Symmetric mode

Mode	Frequency, Hz						
	Measured	Initial analysis	RS3	RS4	RS5	RS6 (a)	RM1
1	43.6	53.2	53.85	45.55	46.8	44.2	44.2
2	51.6	62.6	59.5	54.3	55.1	54.4	53.6
3	57.9	75.2	74.4	63.45	65.8	63.0	64.4
4	79.9	108.5	108.7	86.3	88.3	80.2	84.2

(b) Antisymmetric mode

Mode	Frequency, Hz				
	Measured	Initial analysis (a)	RM1	RM2	RS6 (a)
1	42.0	52.9	44.5	44.4	42.2
2	51.2	72.6	54.3	54.2	57.0
3	(b)	85.1	67.4	67.2	58.6
4	(b)	92.0	77.8	76.5	78.9
5	93.4	101.5	88.7	86.4	71.6

[a] From reference 21.
[b] Not found.

TABLE XVII.- EFFECTIVE CROSS-SECTIONAL AREAS FOR PANELS IN PAYLOAD BAY
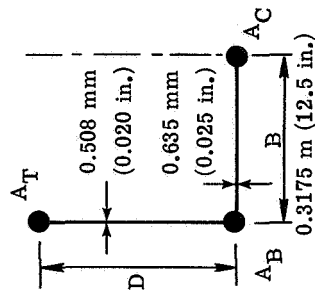
Fuselage station		Side depth, D		Fully effective skin area		A_T		A_B		A_C		A_{total}		Effective skin area, percent
m	in.	m	in.	cm²	in²	cm²	in²	cm²	in²	cm²	in²	cm²	in²	
Based on 1/6-area criterion [a]														
1.680	66.125	0.355	13.96	3.817	0.592	0.300	0.0465	0.636	0.0985	0.335	0.052	1.271	0.197	33.3
2.102	82.75	.376	14.81	3.927	.609	.3185	.0494	.654	.101	.335	.052	1.308	.203	33.3
2.529	99.56	.398	15.67	4.038	.626	.337	.0522	.673	.104	.335	.052	1.345	.208	33.3
2.826	111.25	.413	16.27	4.116	.638	.350	.0542	.685	.106	.335	.052	1.371	.212	33.3
3.105	122.25	.428	16.83	4.188	.649	.362	.0561	.697	.108	.335	.052	1.395	.216	33.3
From matched inertias based on measured deflections														
1.680	66.125	0.355	13.96	3.817	0.592	0.307	0.0476	0.861	0.133	0.592	0.0918	1.760	0.273	46.1
2.102	82.75	.376	14.81	3.927	.609	.346	.0536	.893	.138	.596	.0924	1.835	.284	46.7
2.529	99.56	.398	15.67	4.038	.626	.364	.0564	.948	.147	.534	.0828	1.846	.286	45.7
2.826	111.25	.413	16.27	4.116	.638	.376	.0583	.986	.153	.510	.0790	1.872	.290	45.5
3.105	122.25	.428	16.83	4.188	.649	.423	.0655	.748	.116	.676	.105	1.847	.286	44.1

[a] Area of sidewall, Dt_S; area of lower skin panel, Bt_ℓ.

External tank

Solid rocket booster
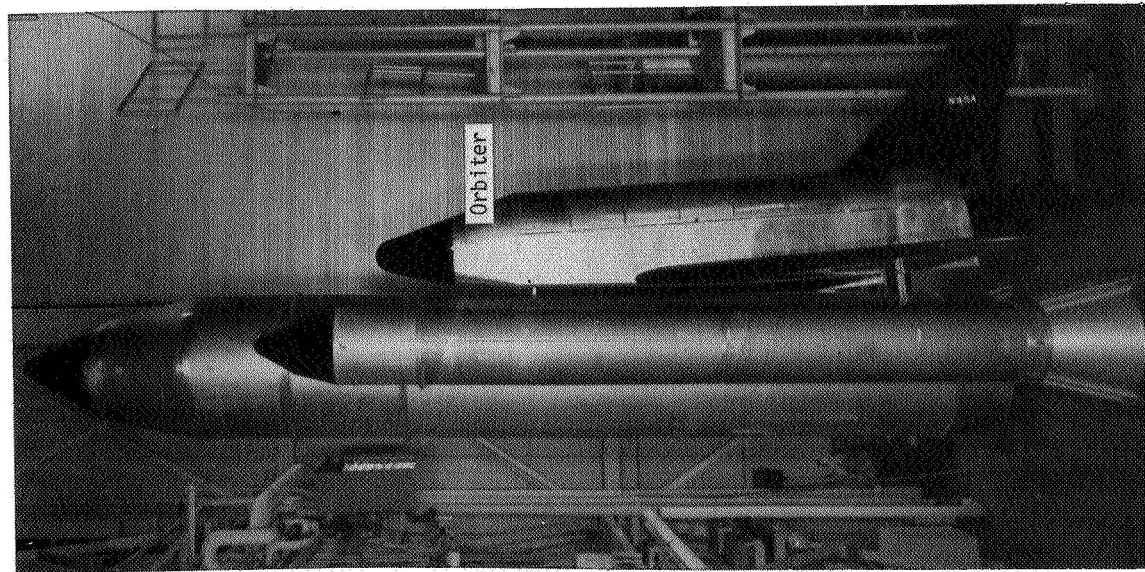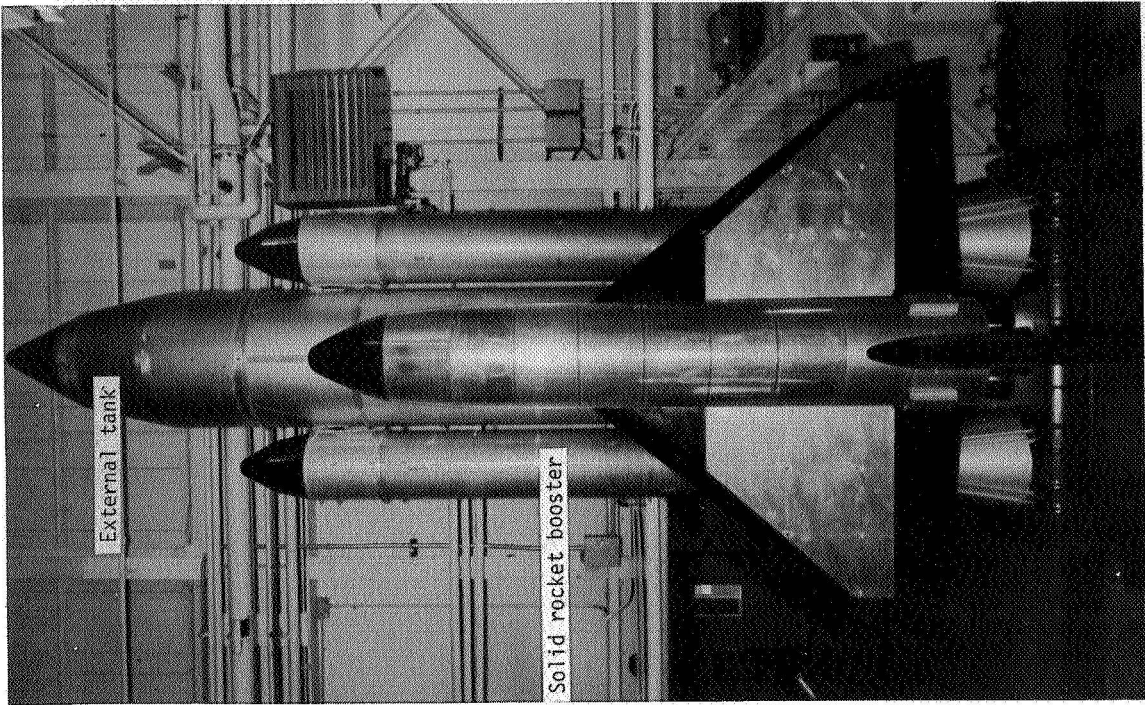
Orbiter

L-75-274

Figure 1.- Photographs of 1/8-scale dynamic model of space-shuttle configuration.

Cabin ballast

Payload

Fuselage cargo bay

Fin ballast location

Fin stub

OPS ballast location
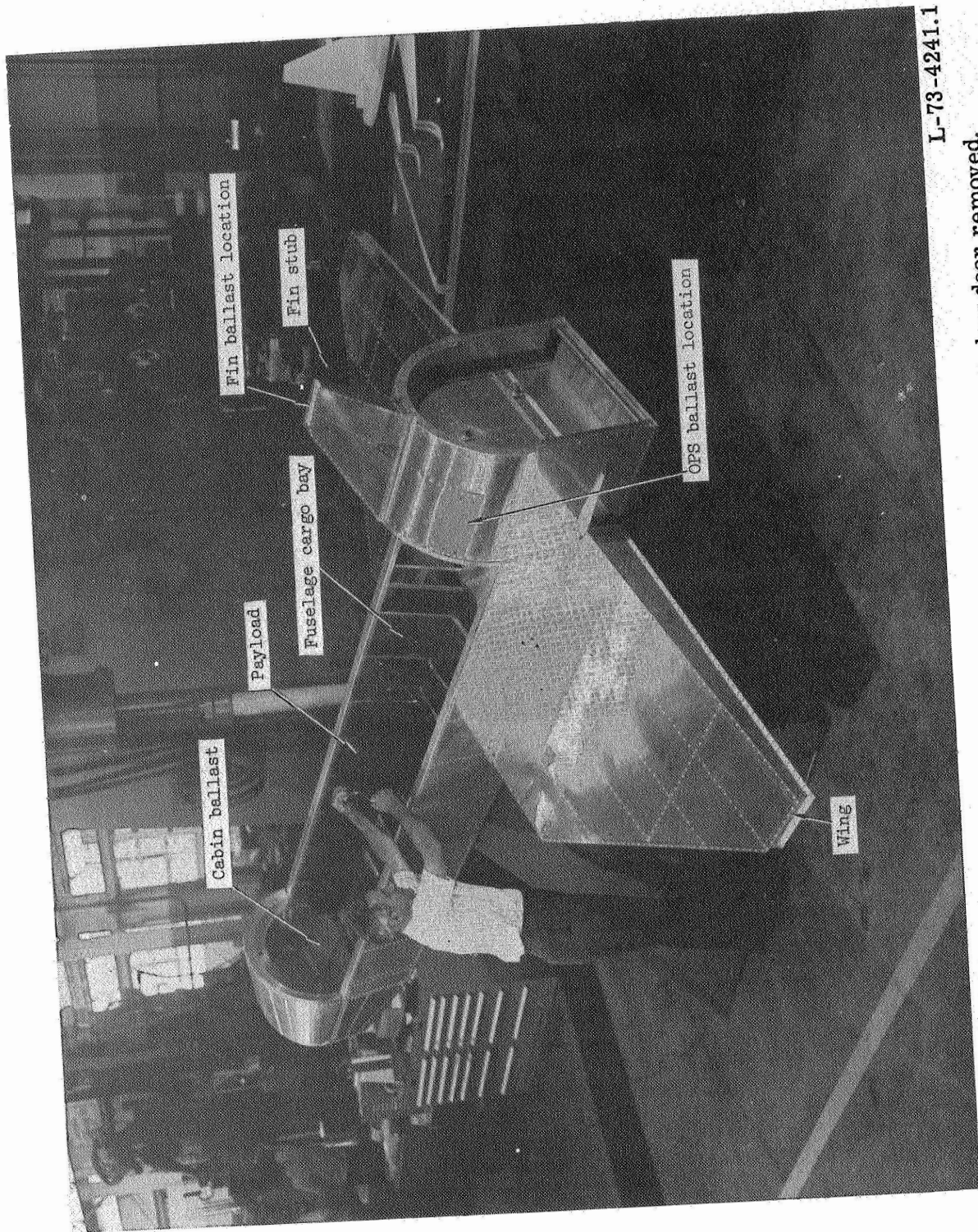
Wing

L-73-4241.1

Figure 2.- Photograph of 1/8-scale orbiter model with cargo-bay door removed.

86
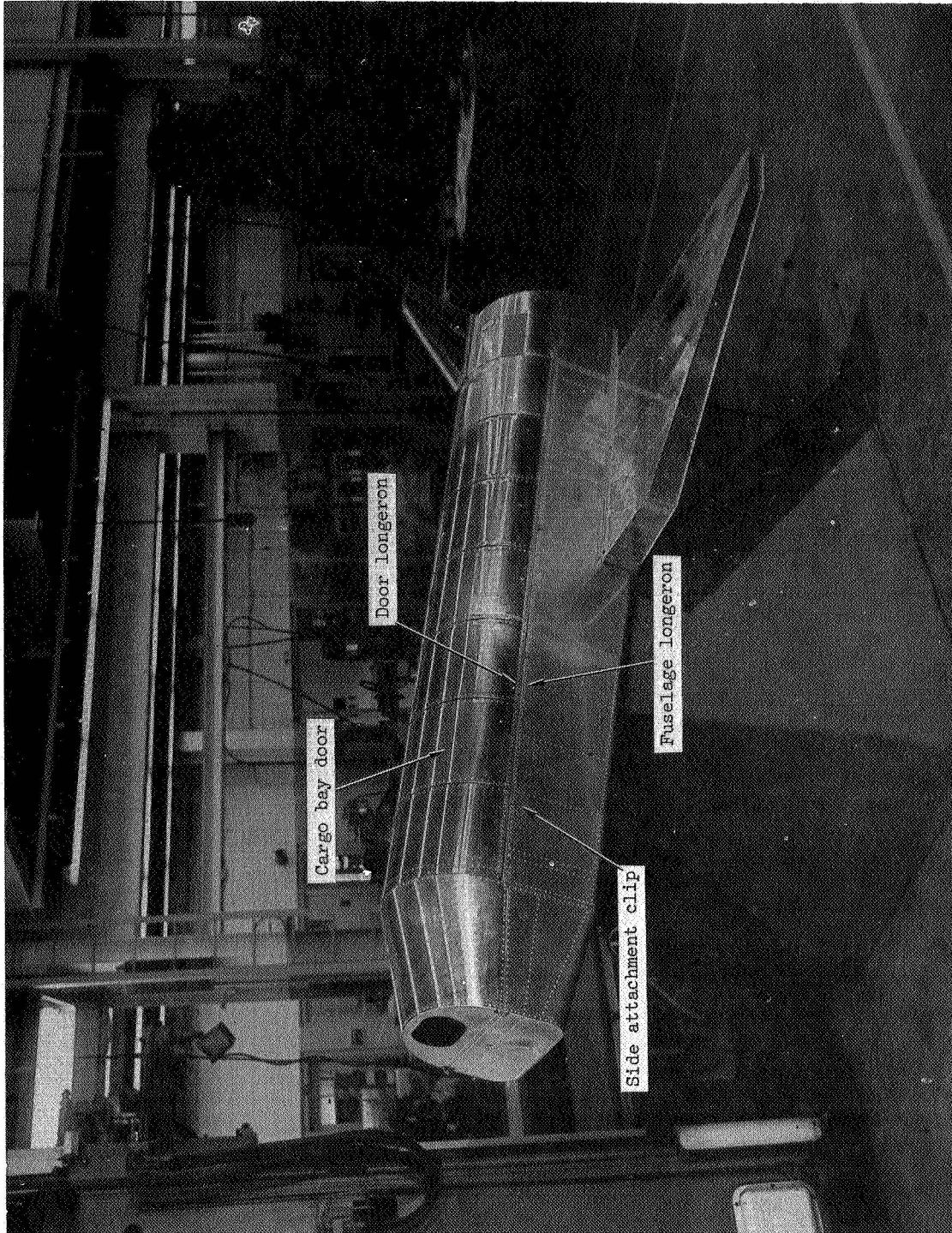
Figure 3.- Photograph of 1/8-scale orbiter model with cargo-bay door installed.

L-73-4244.1

Model substructure	Mass	
	kg	lbm
Fuselage structure	44.398	97.88
Ballast: Crew cabin	26.649	58.75
OPS	23.306	51.38
Fin	2.722	6.00
Wing structure	13.208	29.12
Ballast	15.935	35.13
Payload structure	41.050	90.50
Ballast	15.921	35.10
Cargo bay door	5.275	11.63
Suspension adapters	0.721	1.59
Transducers	1.488	3.28
	190.673	420.36

Station no.	Normalized dimension		
	Length (X)	Elevation (Z)	Span (Y)
1	0	0	0
2	0.1237	0.0251	0.0789
3	0.1541	0.0344	0.0896
4	0.2240	0.0430	0.2129
5	0.2921	0.0803	0.3334
6	0.3602	0.1029	0.4414
7	0.4283	0.1219	
8	0.4964	0.1706	
9	0.5179	0.2115	
10	0.5645	0.3011	
11	0.6326		
12	0.6810		
13	0.7025		
14	0.7428		
15	0.7643		
16	0.8262		
17	0.8495		
18	0.8584		
19	0.8888		
20	0.9553		
21	1.0000		

Figure 4.- General arrangement drawing of 1/8-scale orbiter model. Dimensions are normalized to fuselage overall length 3.543 m (139.5 in.).
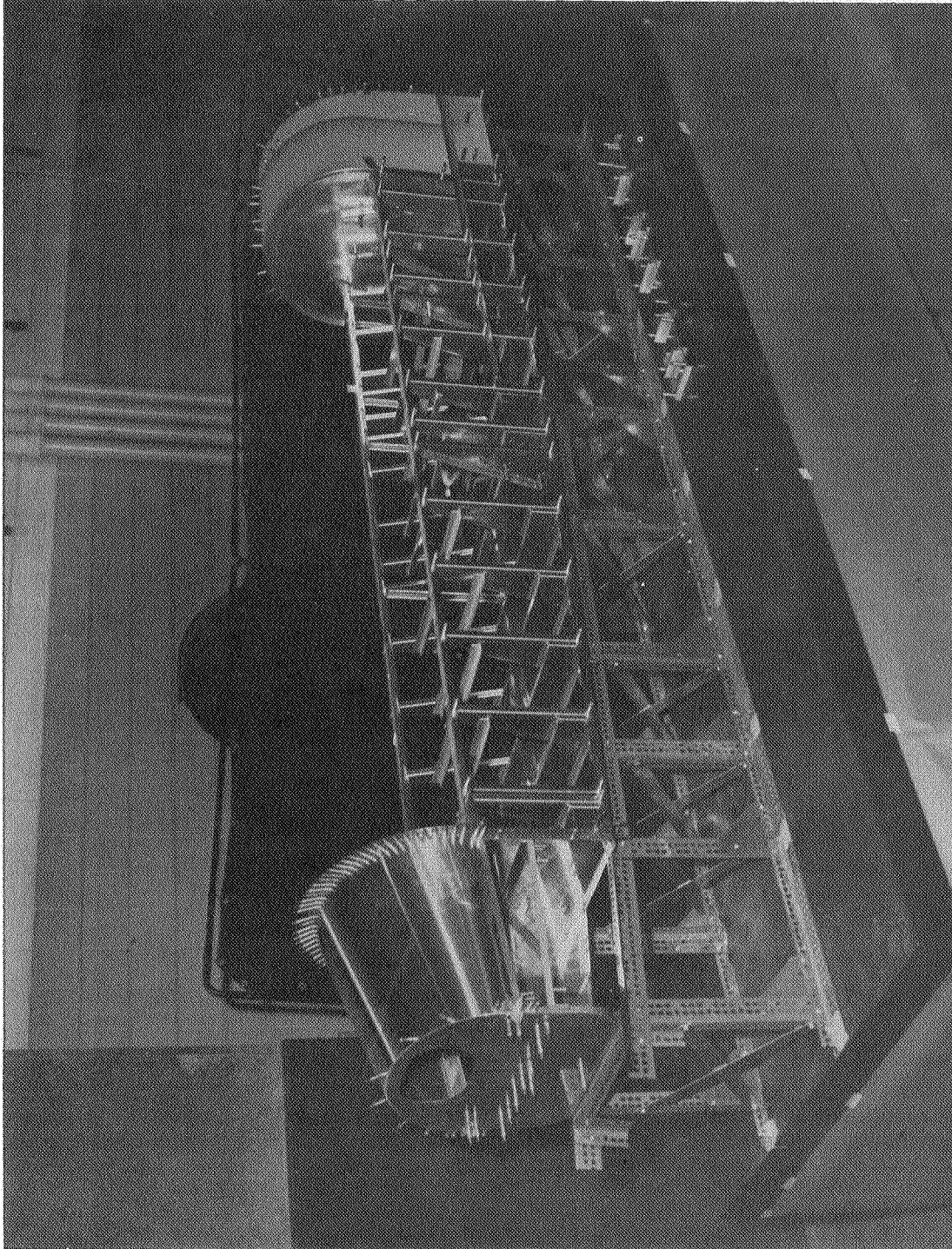
Figure 5.- Construction of 1/8-scale orbiter fuselage.

L-73-459

89

Door longeron

Fuselage longeron

Door clip
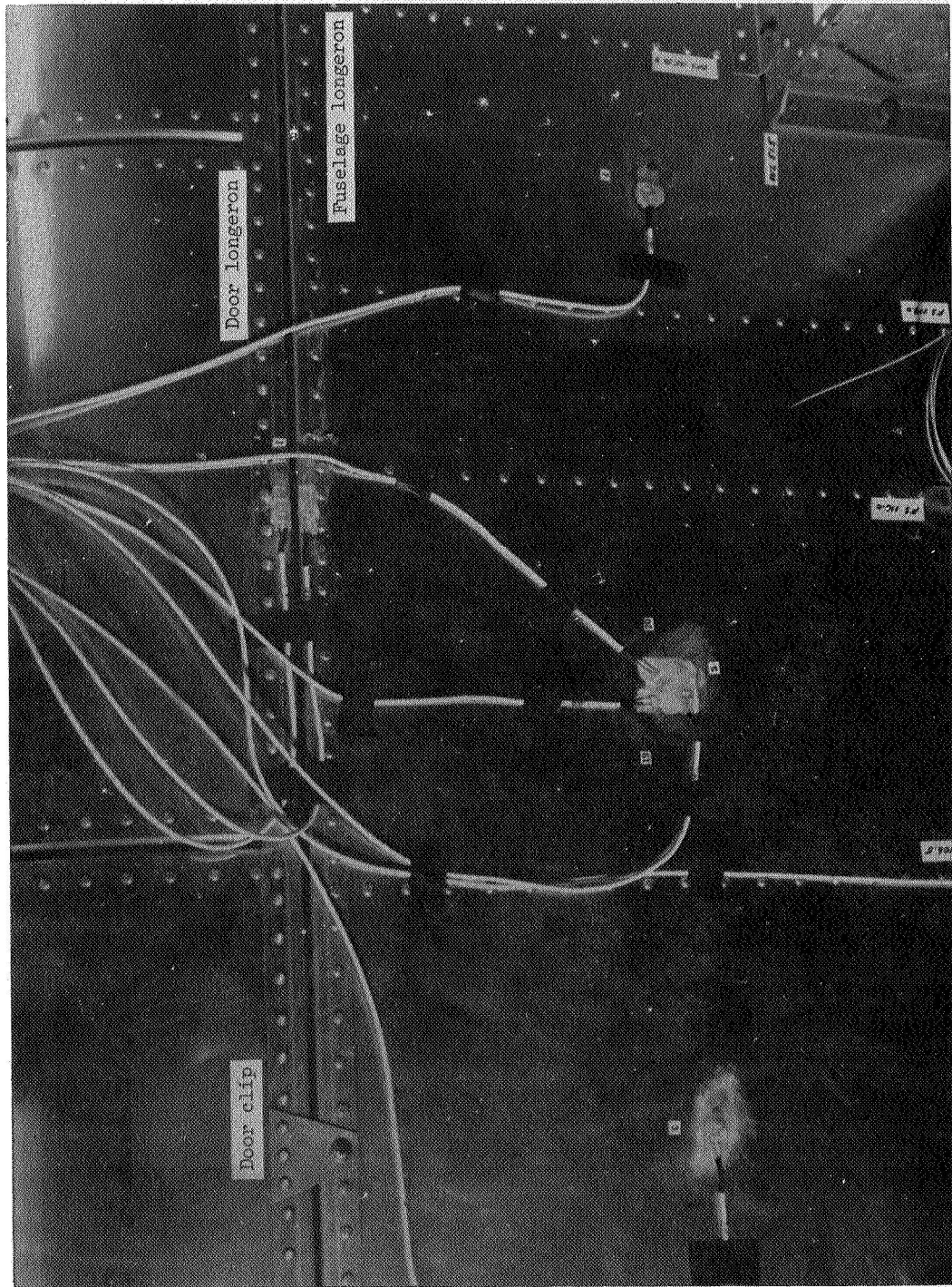
L-74-1946.1

Figure 6.- Strain-gage installation on skin panels and longerons.

Labels on image: Ballast, Root, Ribs, Spars, Tip, Trailing edge
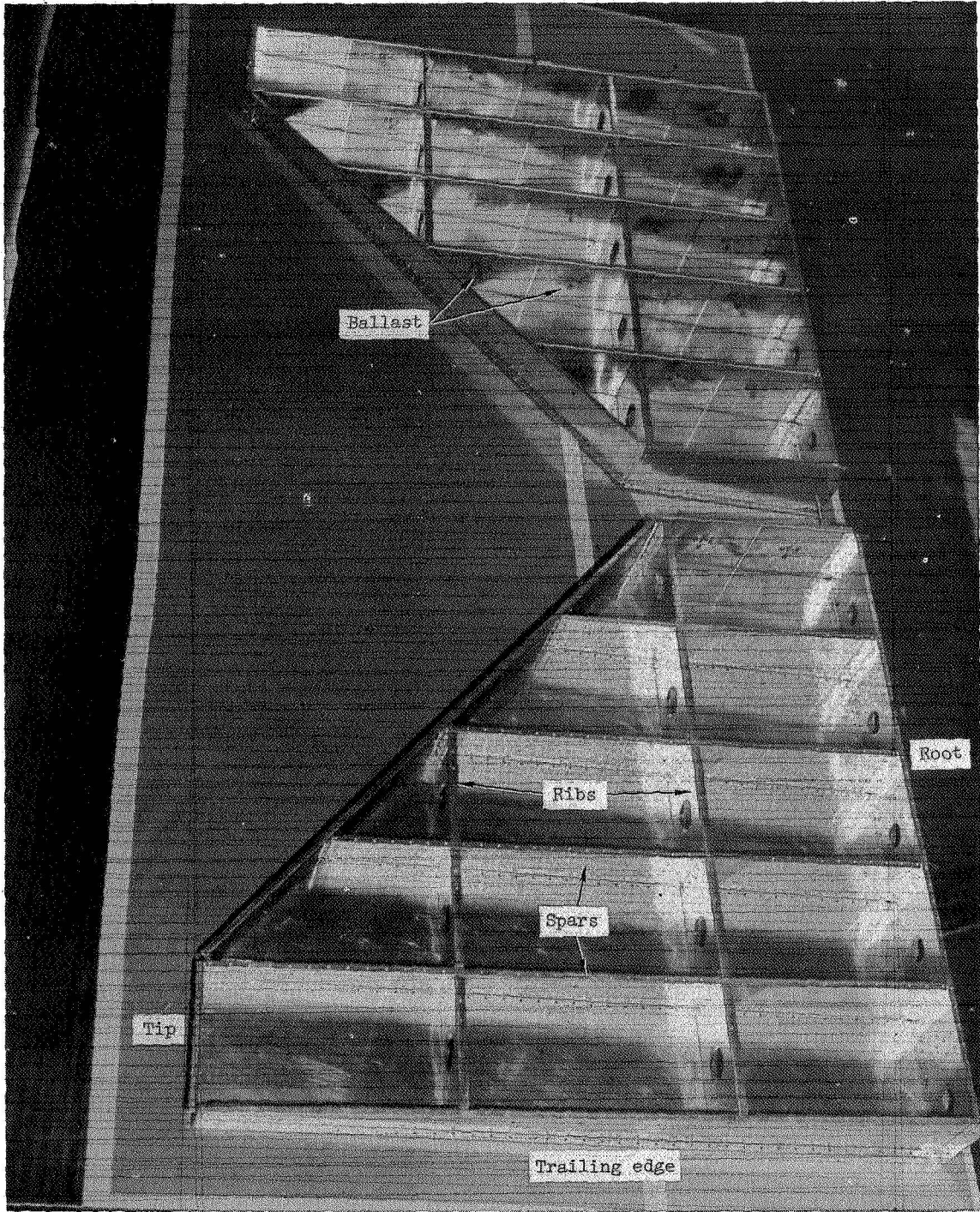
L-73-2642.1

Figure 7.- Partially constructed wings of 1/8-scale orbiter.

Figure 8.- Setup for vibration tests in horizontal attitude.

L-73-6074.1
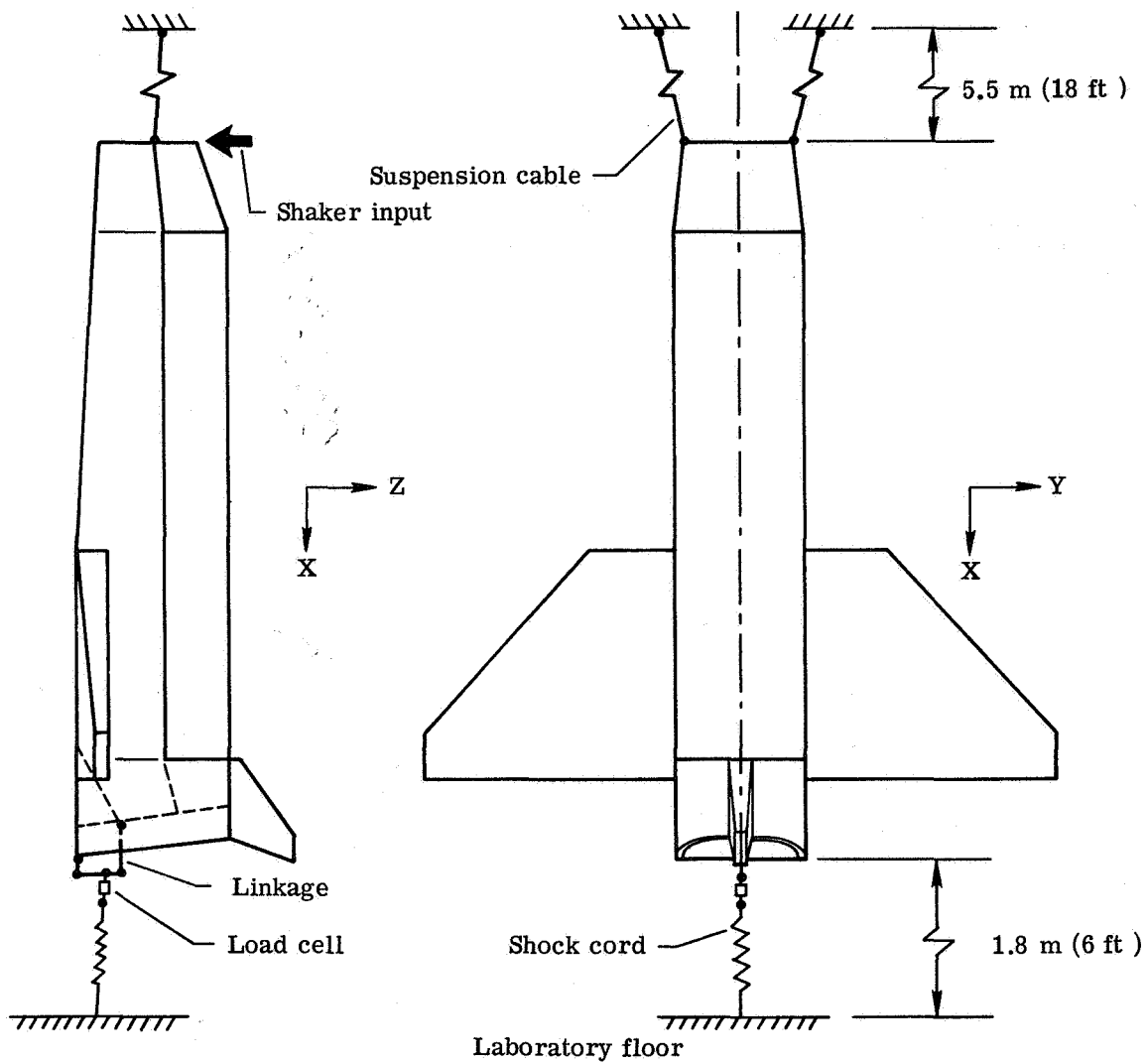
Figure 9.- Setup for vibration tests in vertical attitude with static tension
loading on fuselage.
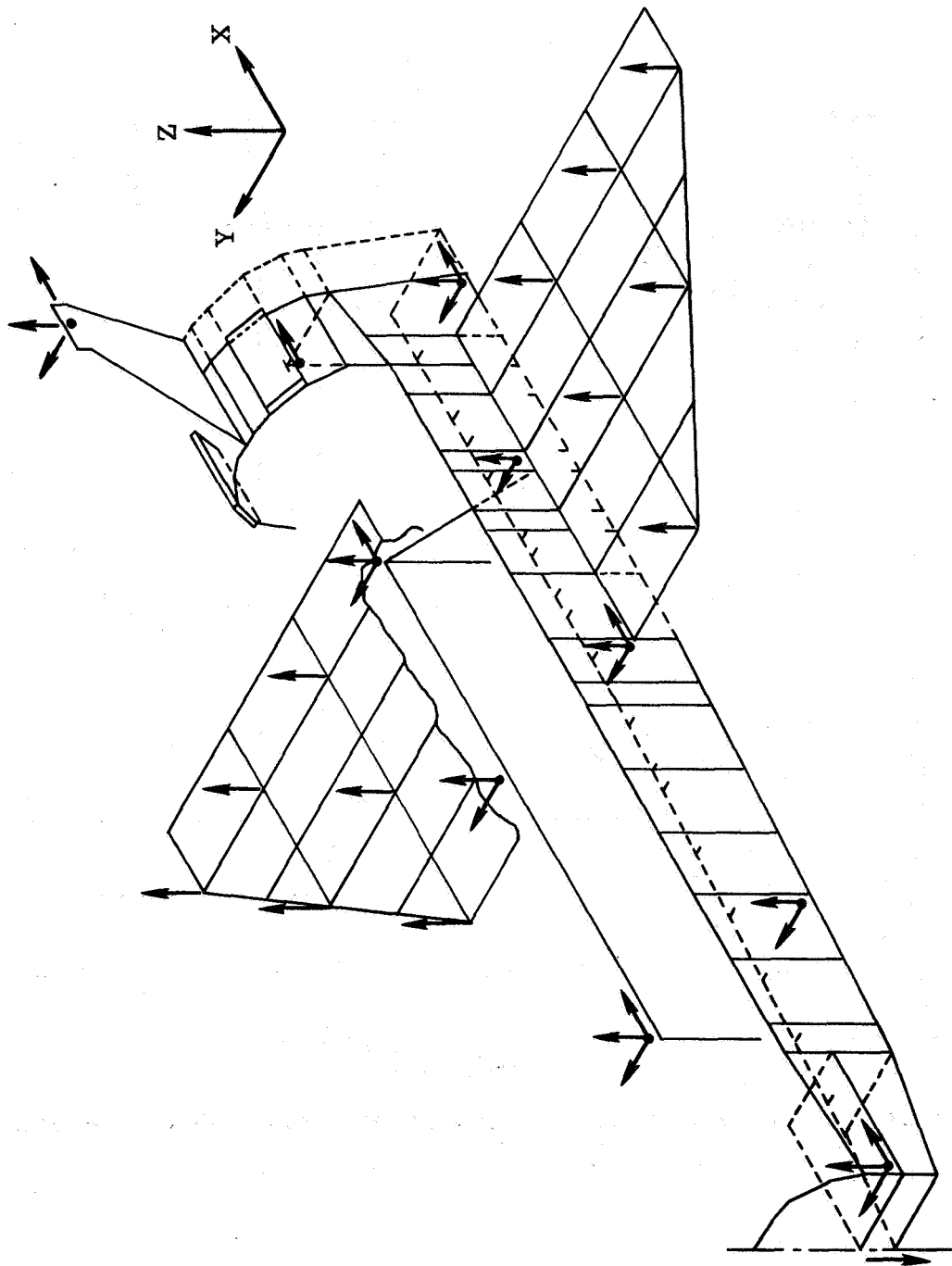
Figure 10.- Schematic drawing of fixed transducer locations for vibration tests.

94
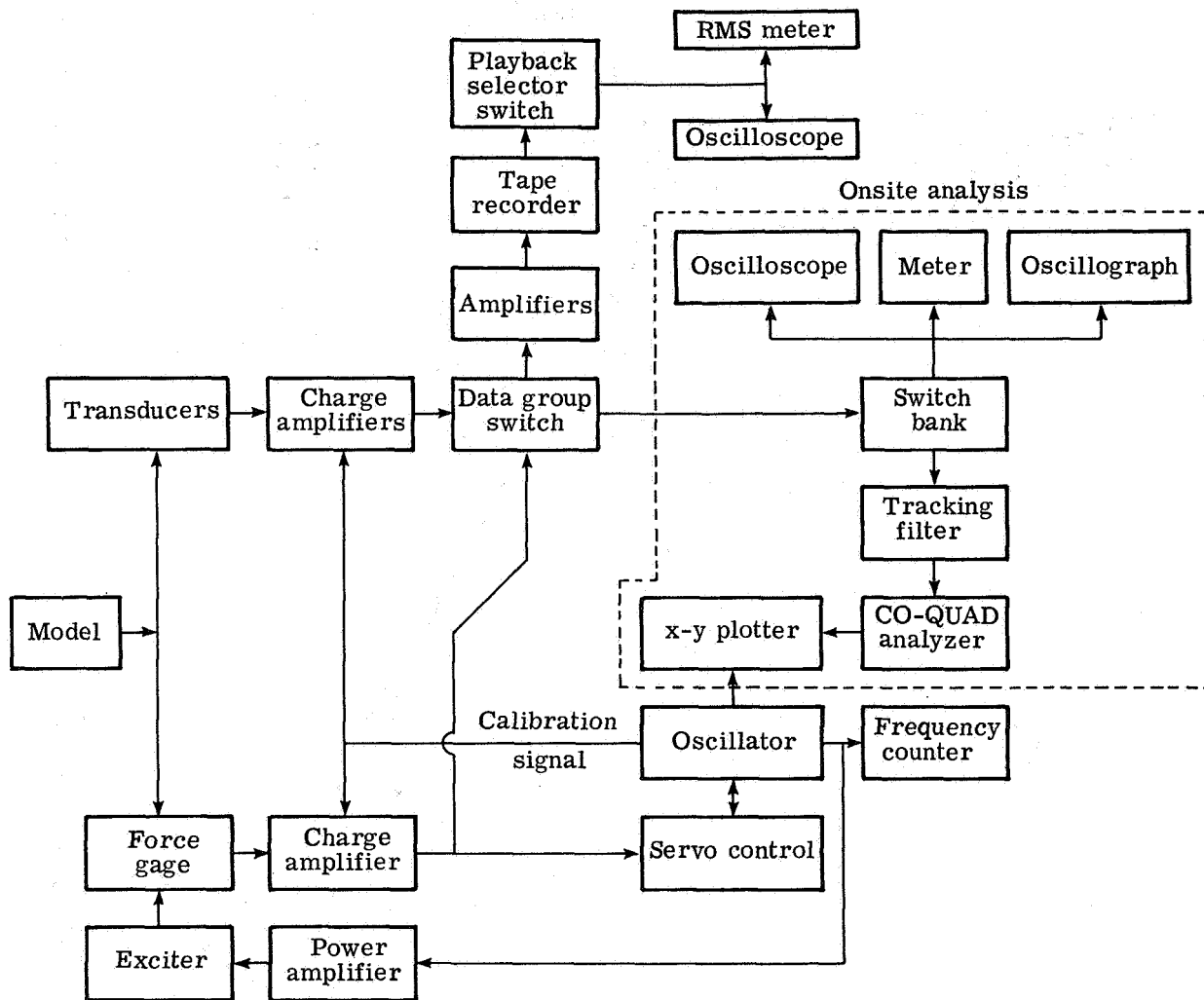
Figure 11.- Schematic diagram of instrumentation.
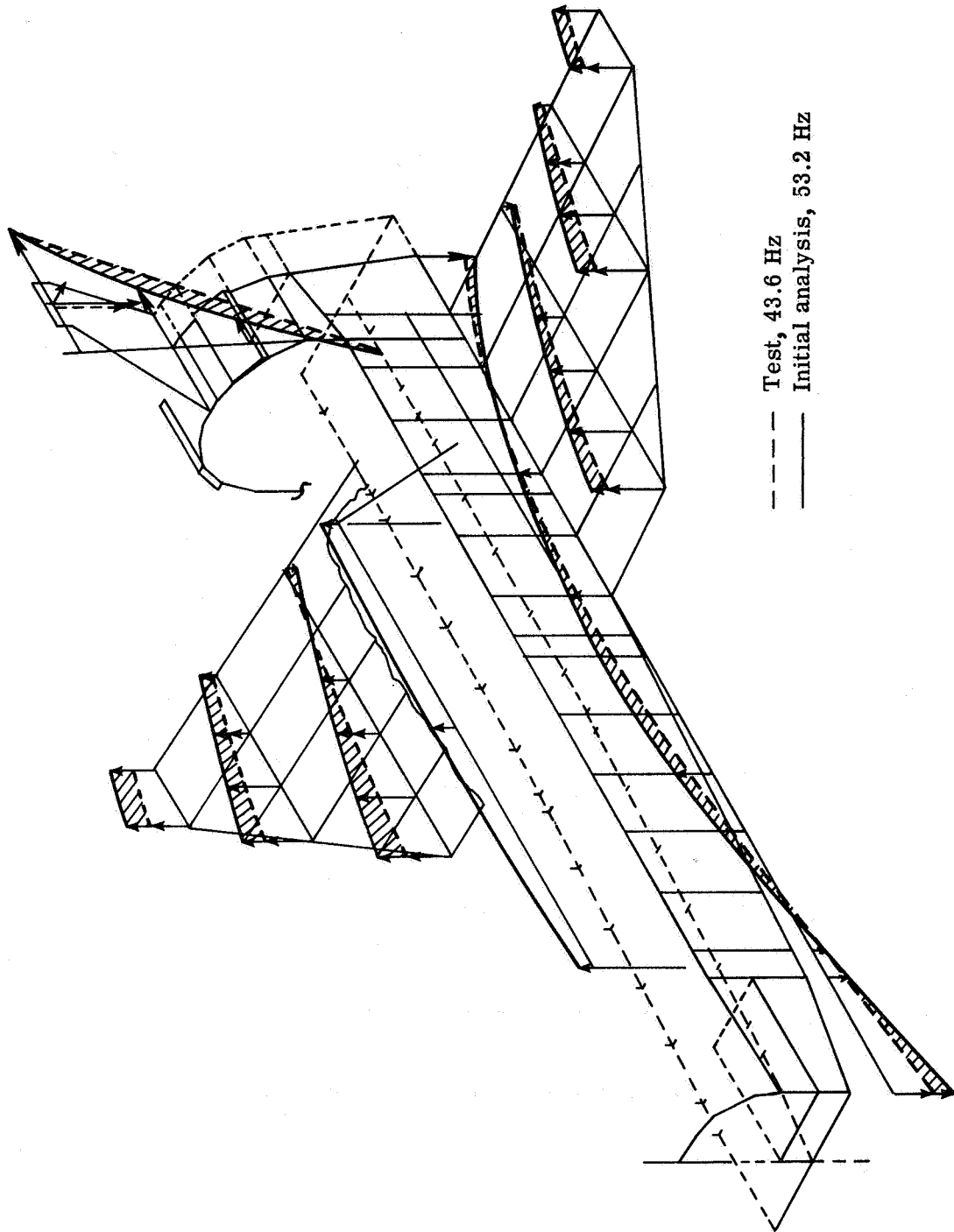
Figure 12.- Measured and analytical mode shapes for the orbiter first symmetric mode.

---- Test, 43.6 Hz
—— Initial analysis, 53.2 Hz
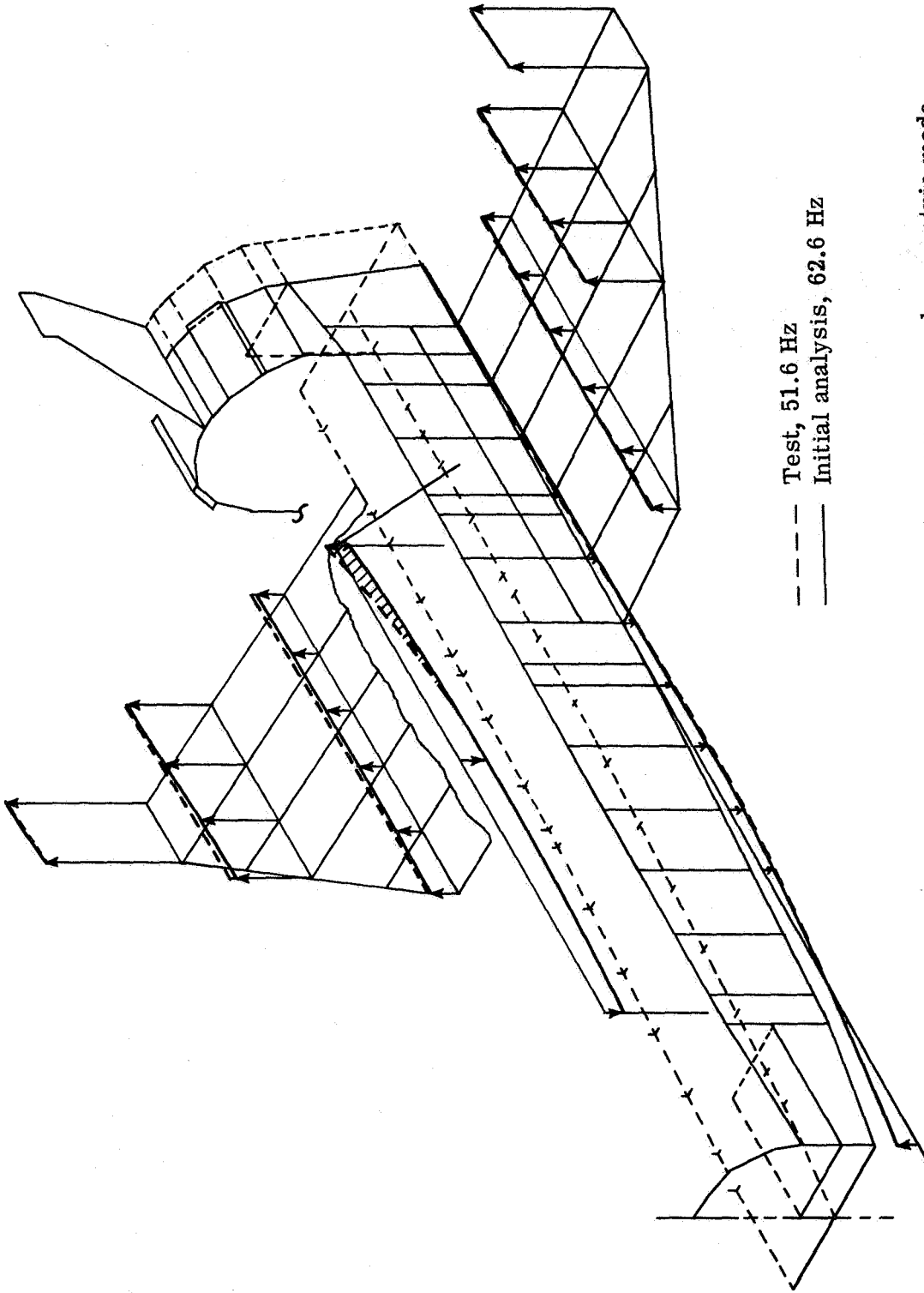
Figure 13.- Measured and analytical mode shapes for the orbiter second symmetric mode.

- - - Test, 51.6 Hz
——— Initial analysis, 62.6 Hz
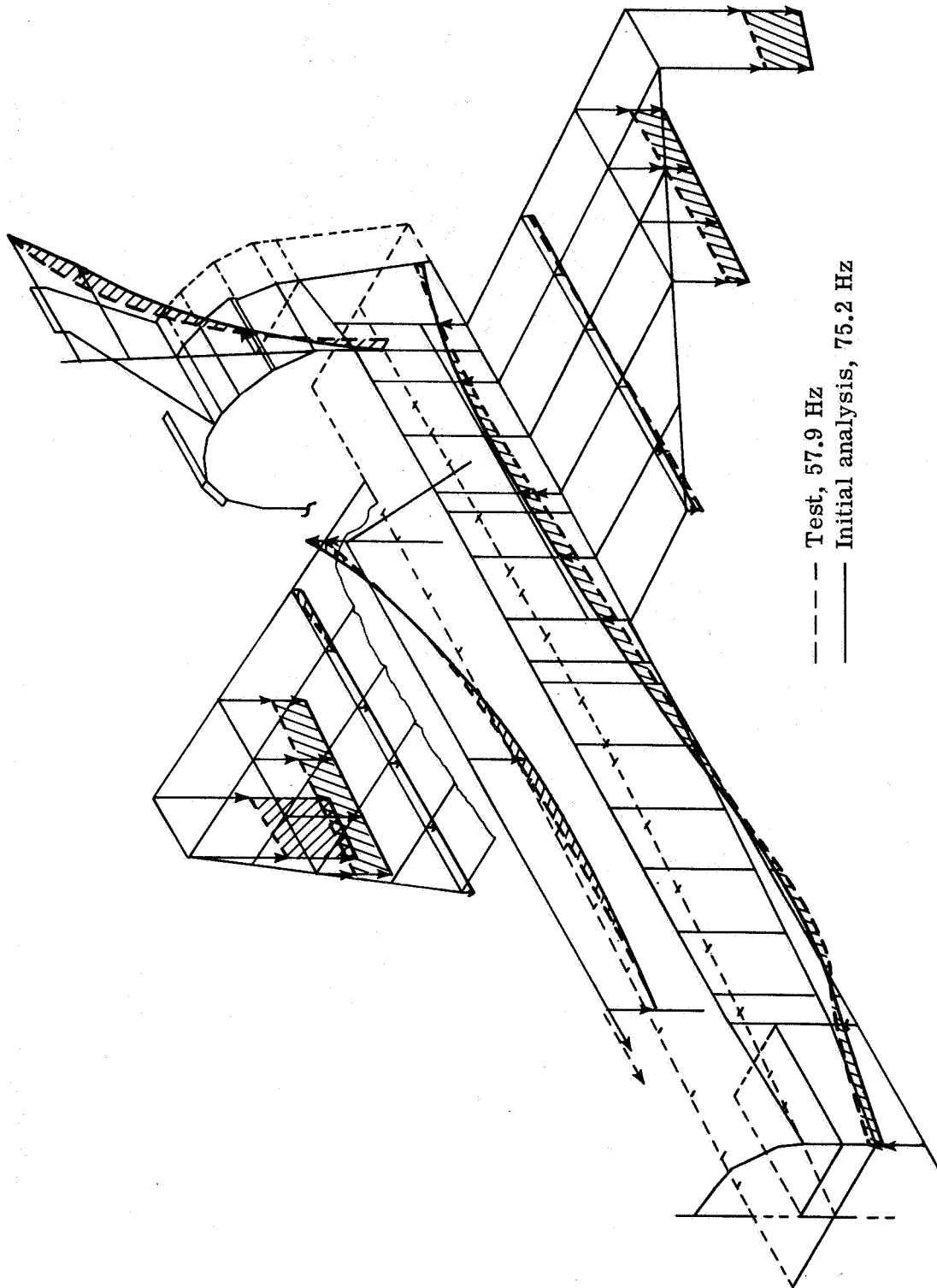
Figure 14.- Measured and analytical mode shapes for the orbiter third symmetric mode.

---- Test, 57.9 Hz
—— Initial analysis, 75.2 Hz
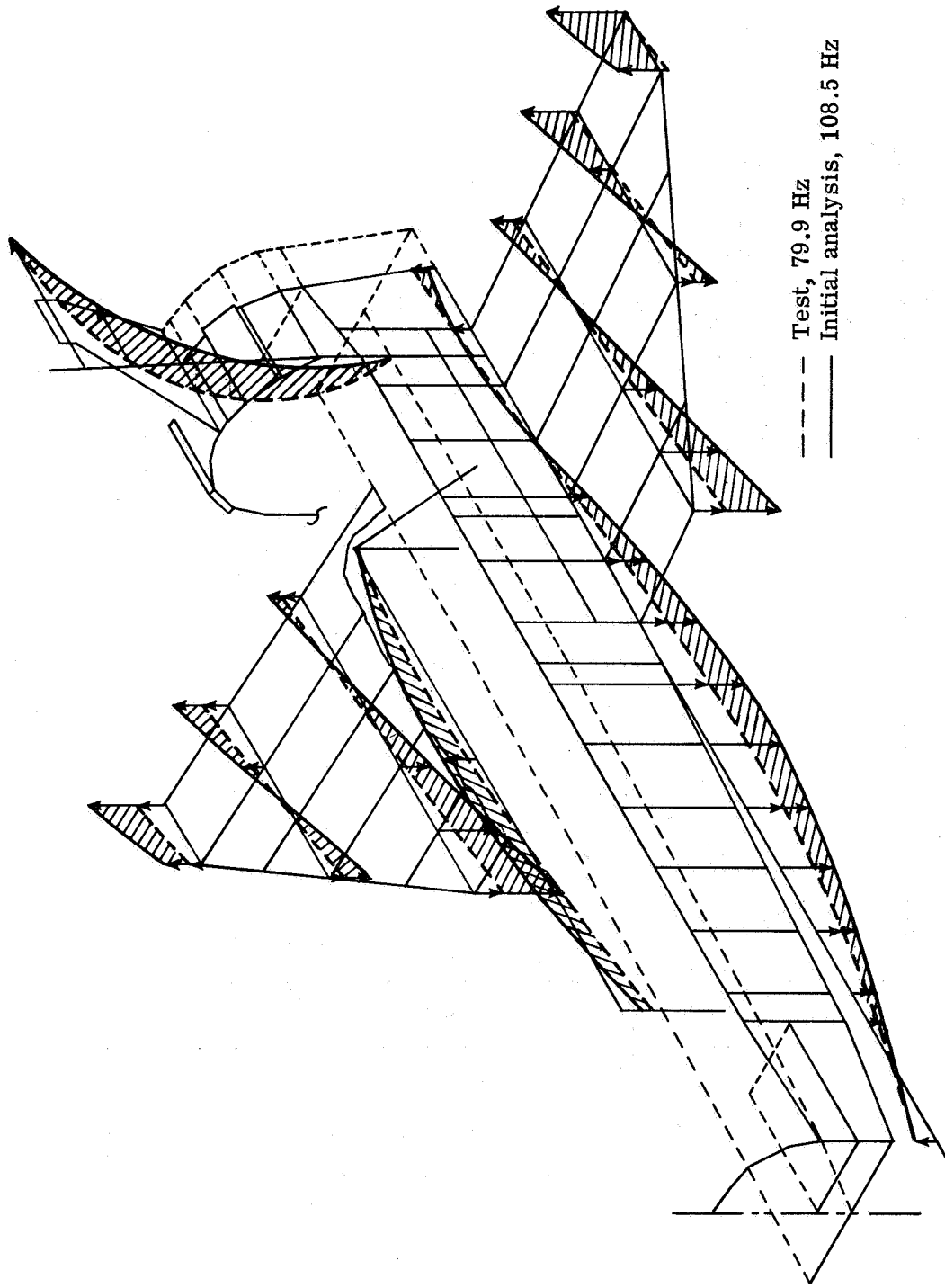
Figure 15.- Measured and analytical mode shapes for the orbiter fourth symmetric mode.

----- Test, 79.9 Hz
——— Initial analysis, 108.5 Hz
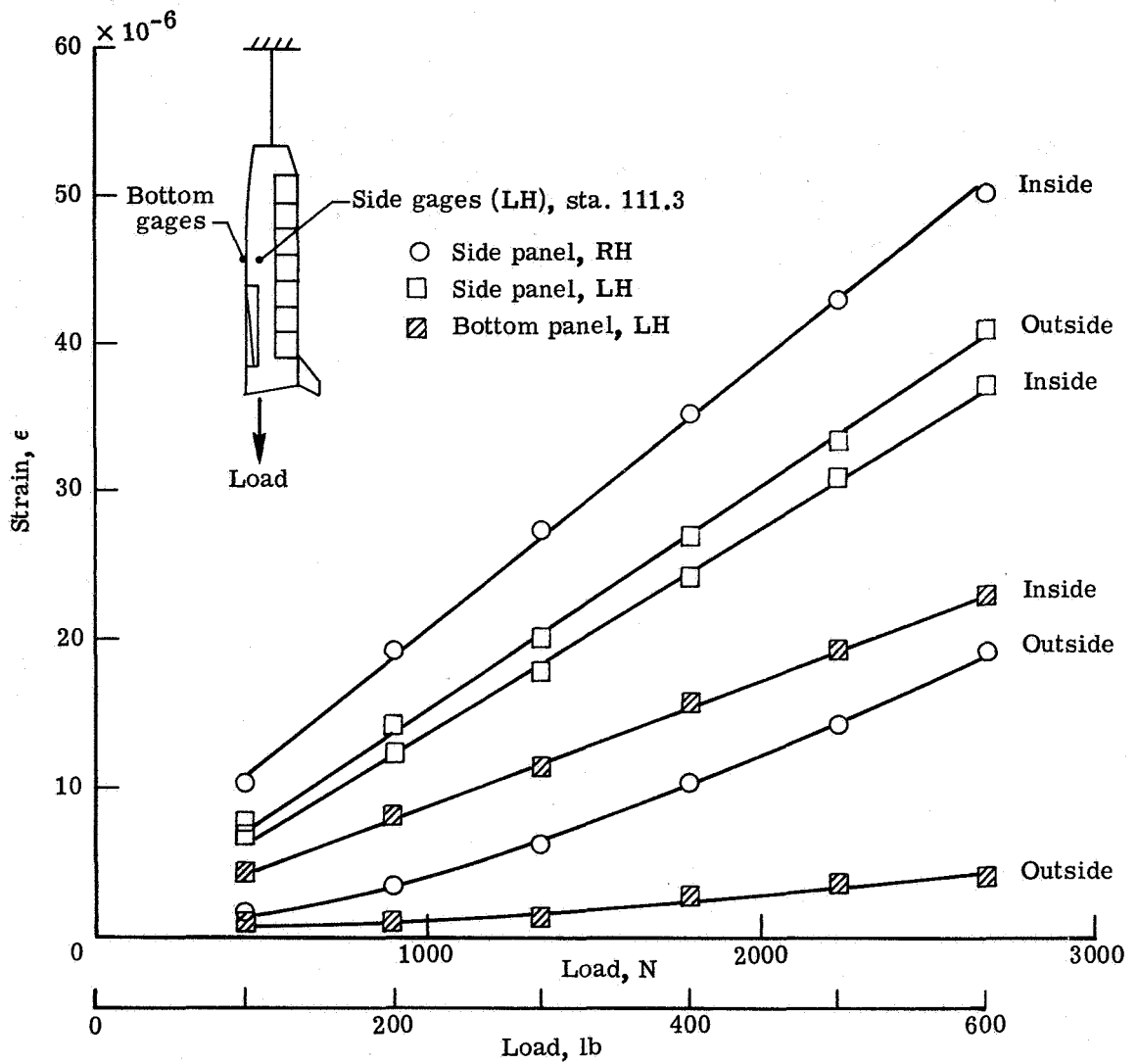
Figure 16.- Static strain-gage measurements obtained on typical fuselage skin panels.
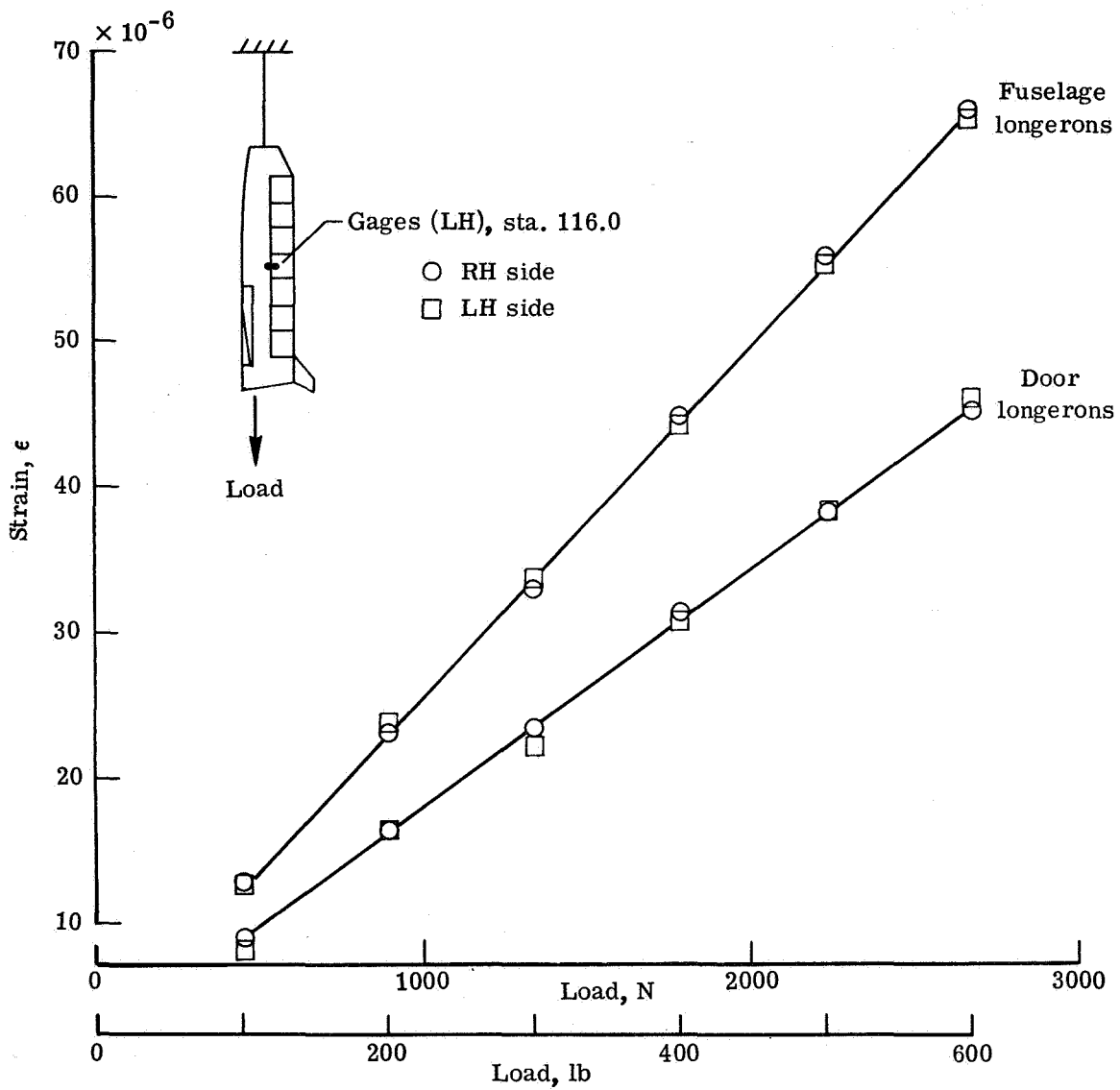
Figure 17.- Static strain-gage measurements obtained on cargo-bay door and fuselage longerons.
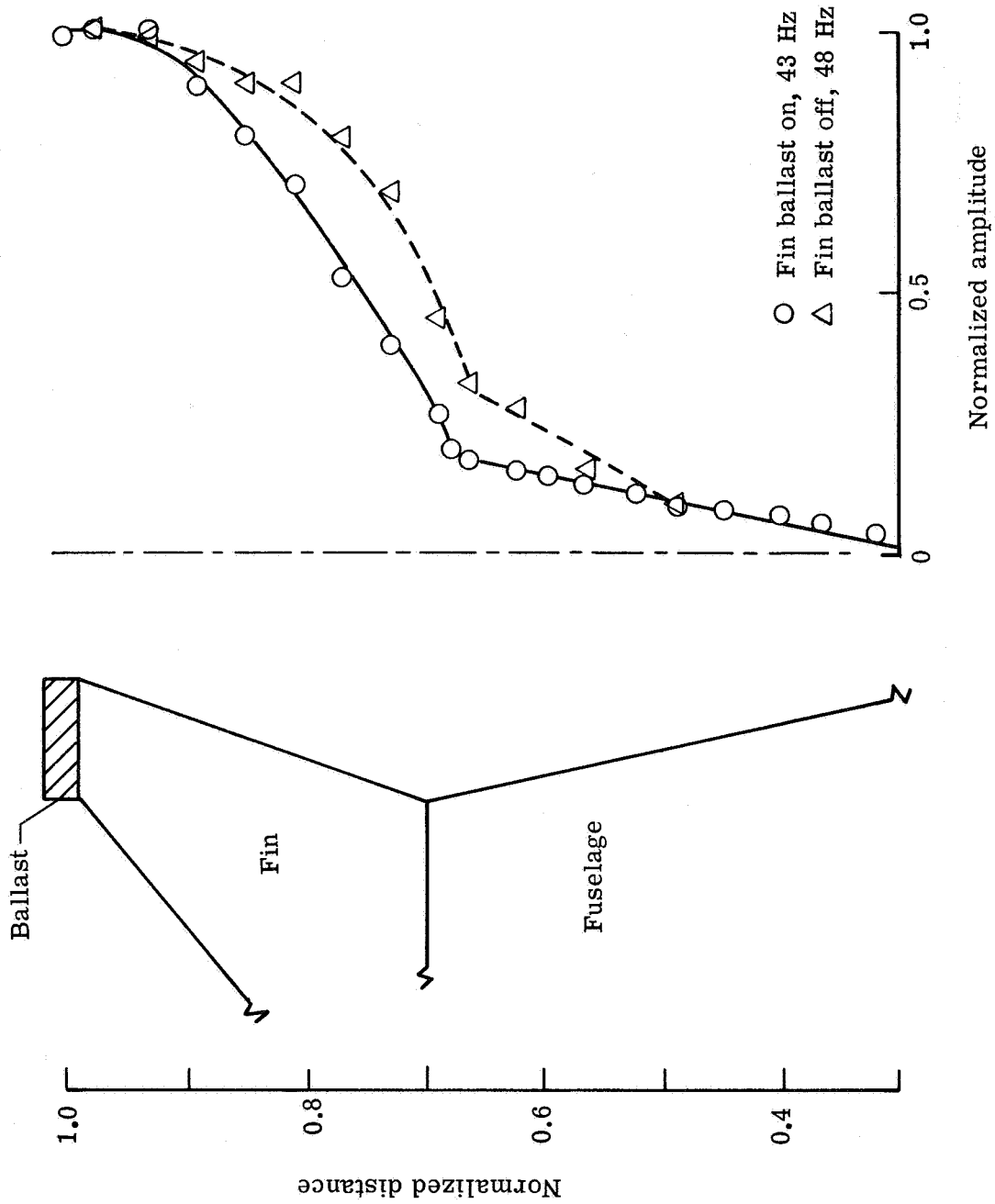
Figure 18.- Effect of fin ballast on experimental first-mode frequency and motion.

Normalized amplitude

○ Fin ballast on, 43 Hz
△ Fin ballast off, 48 Hz

Normalized distance

Ballast

Fin

Fuselage
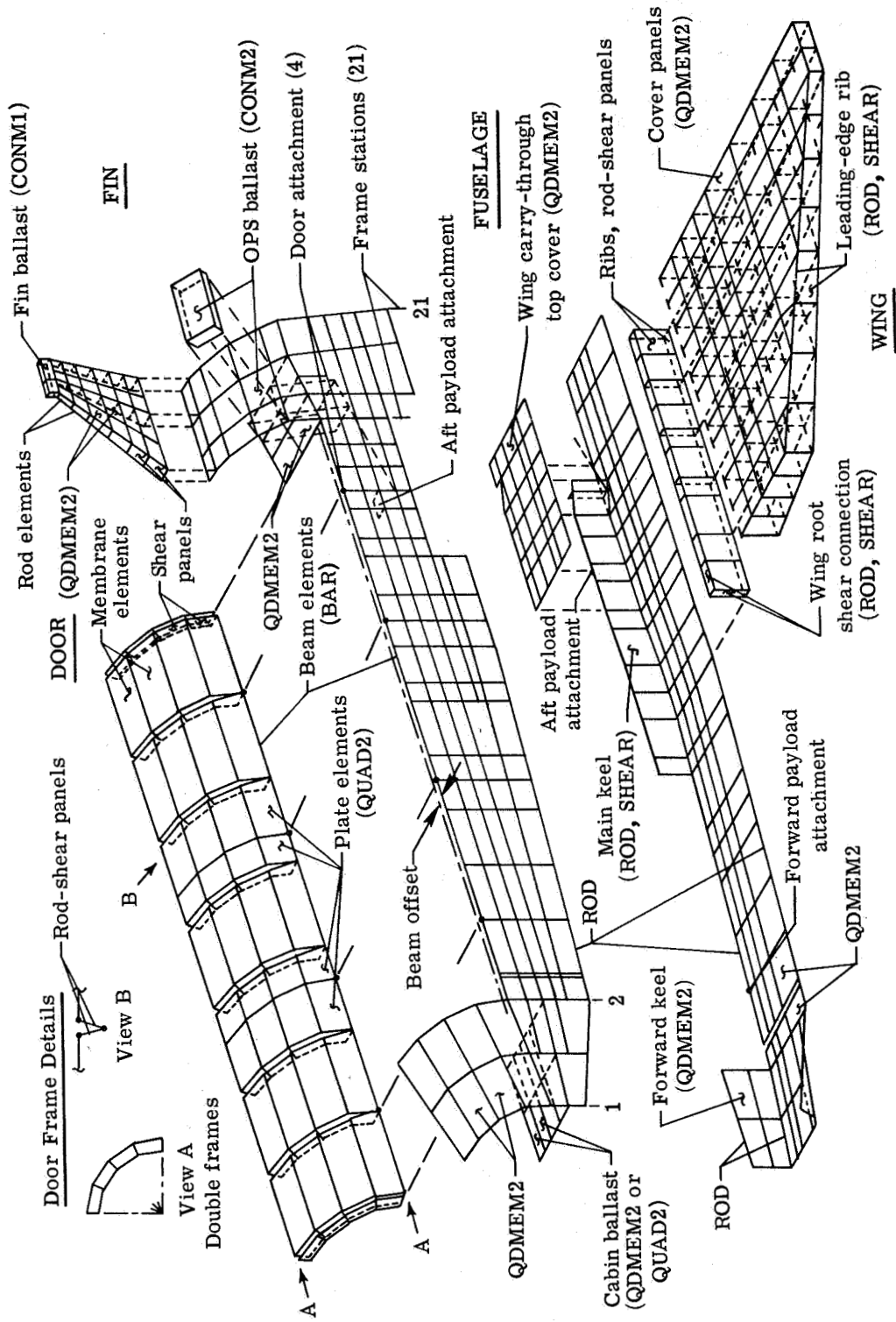
(a) Main substructures.

Figure 19.- 1/8-scale orbiter NASTRAN model (NASTRAN element identifications in parentheses).

103

Aft support brackets

Dummy elements (PLOTEL)

Aft payload attachments

Beam elements (BAR)

Grid points, concentrated masses (CONM2)

Forward support bracket

Dummy element (PLOTEL)

Forward payload attachment
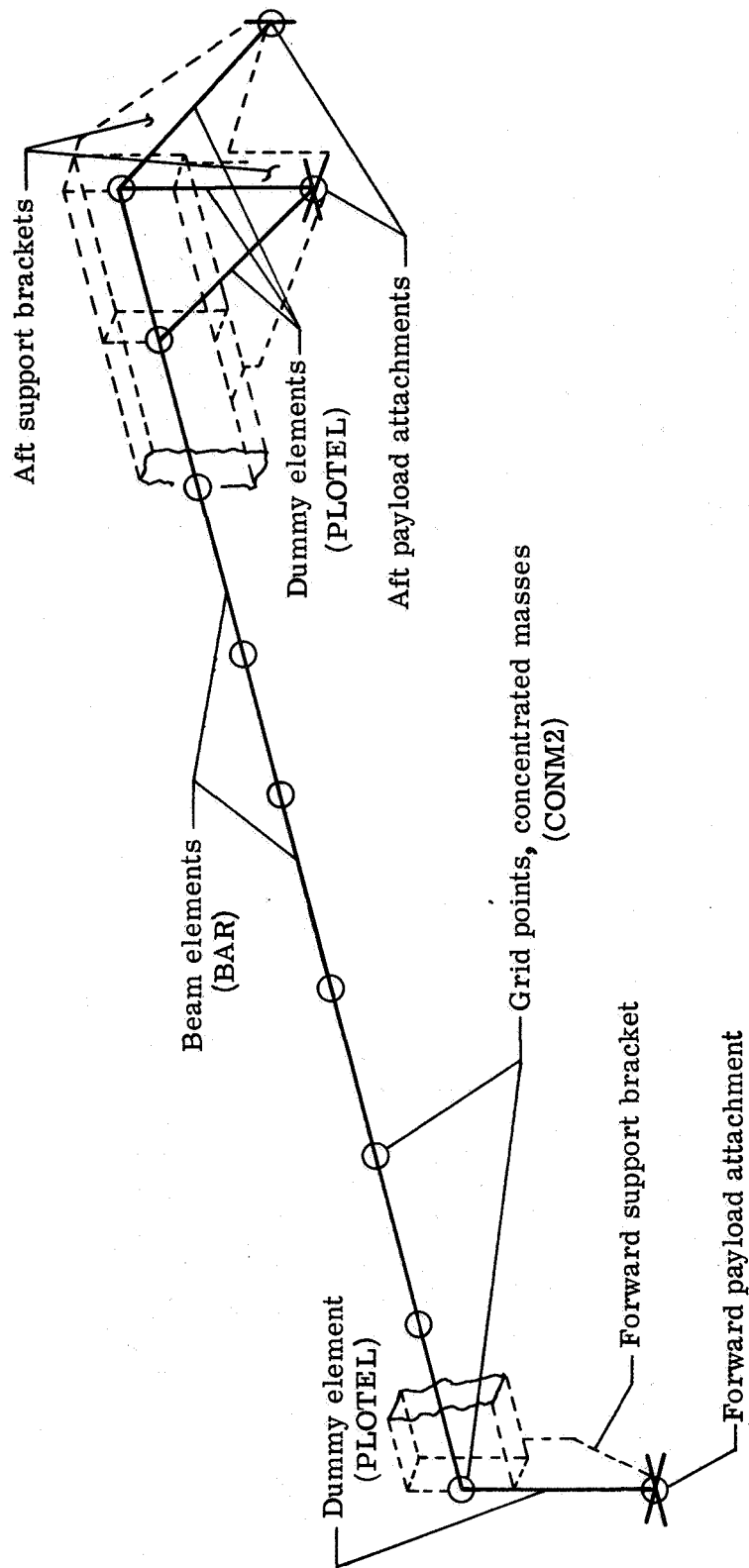
(b) Payload structure (actual beam and support brackets shown as dotted lines; support brackets assumed rigid).

Figure 19.- Concluded.
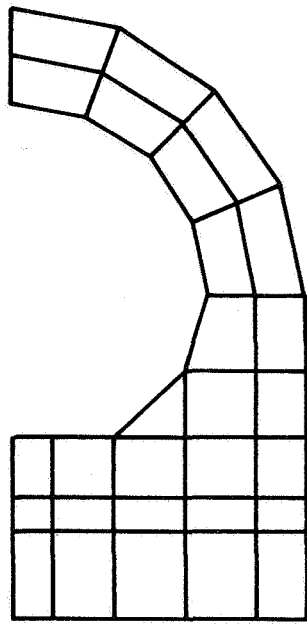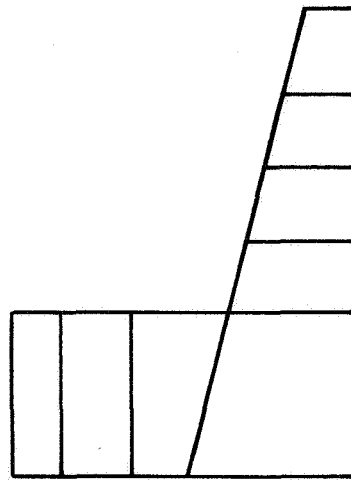
Cabin frame   Payload bay frame
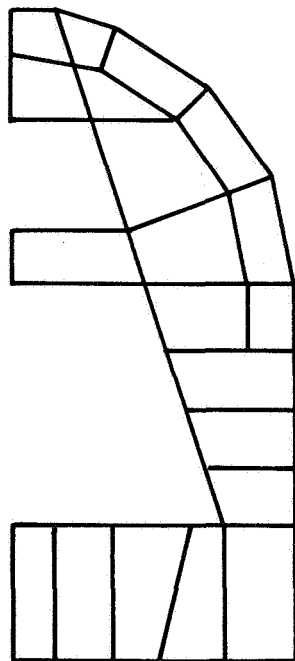
Frames in engine support structure
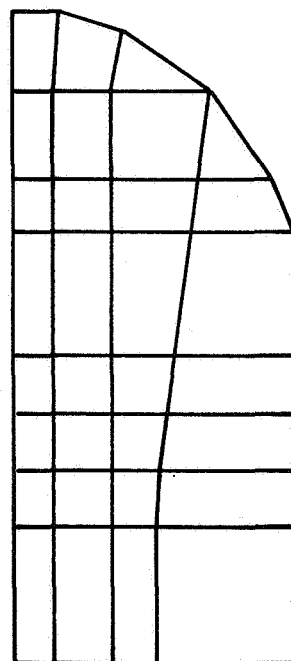
Figure 20.- Typical NASTRAN rod-shear panel models for frames
for 1/8-scale fuselage.
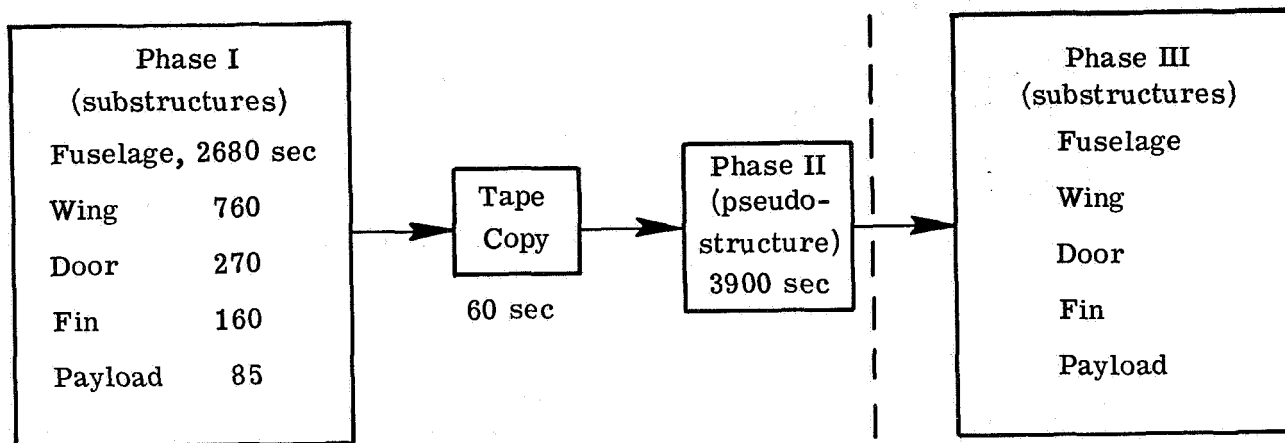
Total central processing unit time for full calculation 7915 sec.

Figure 21.- Orbiter substructuring sequence and computation times.
(Phase III not executed in this investigation.)

Labels within figure: L-74-3987.1

Top cover

Typical wing-fuselage shear connection

Typical fuselage frame

Bottom of fuselage
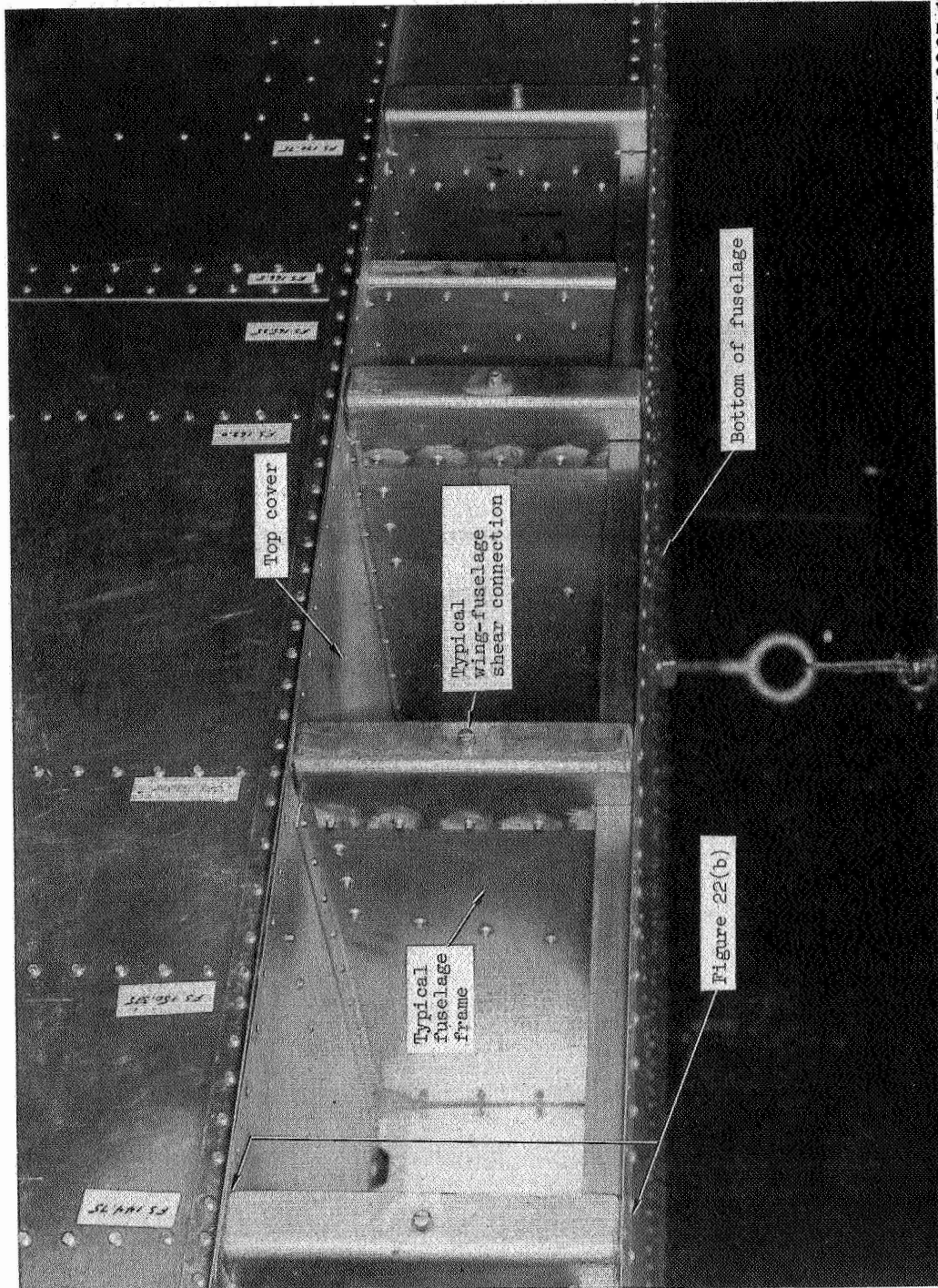
Figure 22(b)

(a) Overall view into fuselage interior.

Figure 22.- Views of wing carry-through structure with wing removed.

107

Wing carry-through top cover

Fuselage frame

Cutout for fuselage frame

Wing-fuselage vertical shear pin connection

Vertical channel (0.32 cm, 0.125 in.)
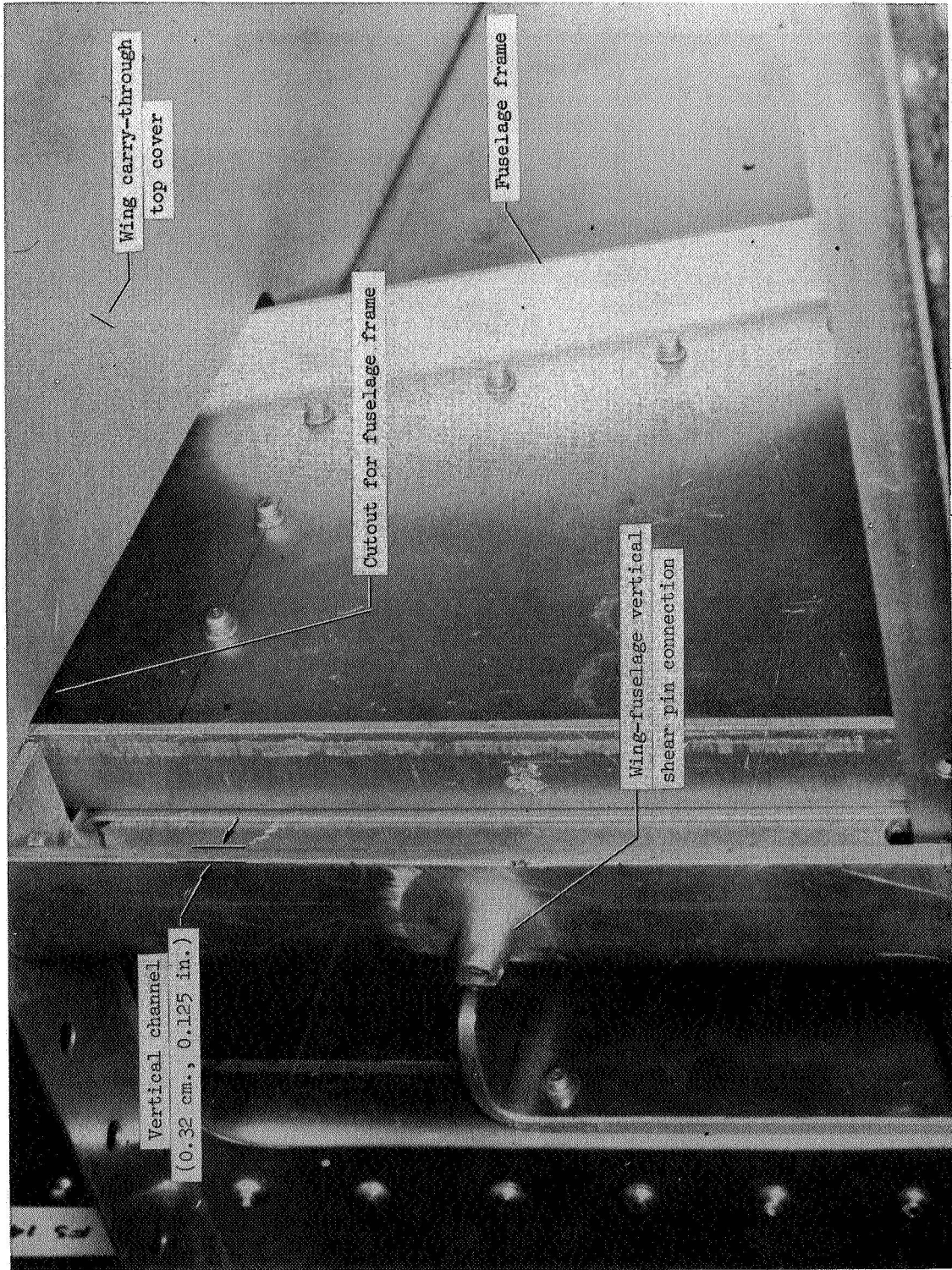
L-74-3988.1

(b) Wing-fuselage interface at fuselage station 144.75.

Figure 22. - Concluded.

Fin ballast

Center spar gusset plate

Forward spar clip

Fin-fuselage angle connection
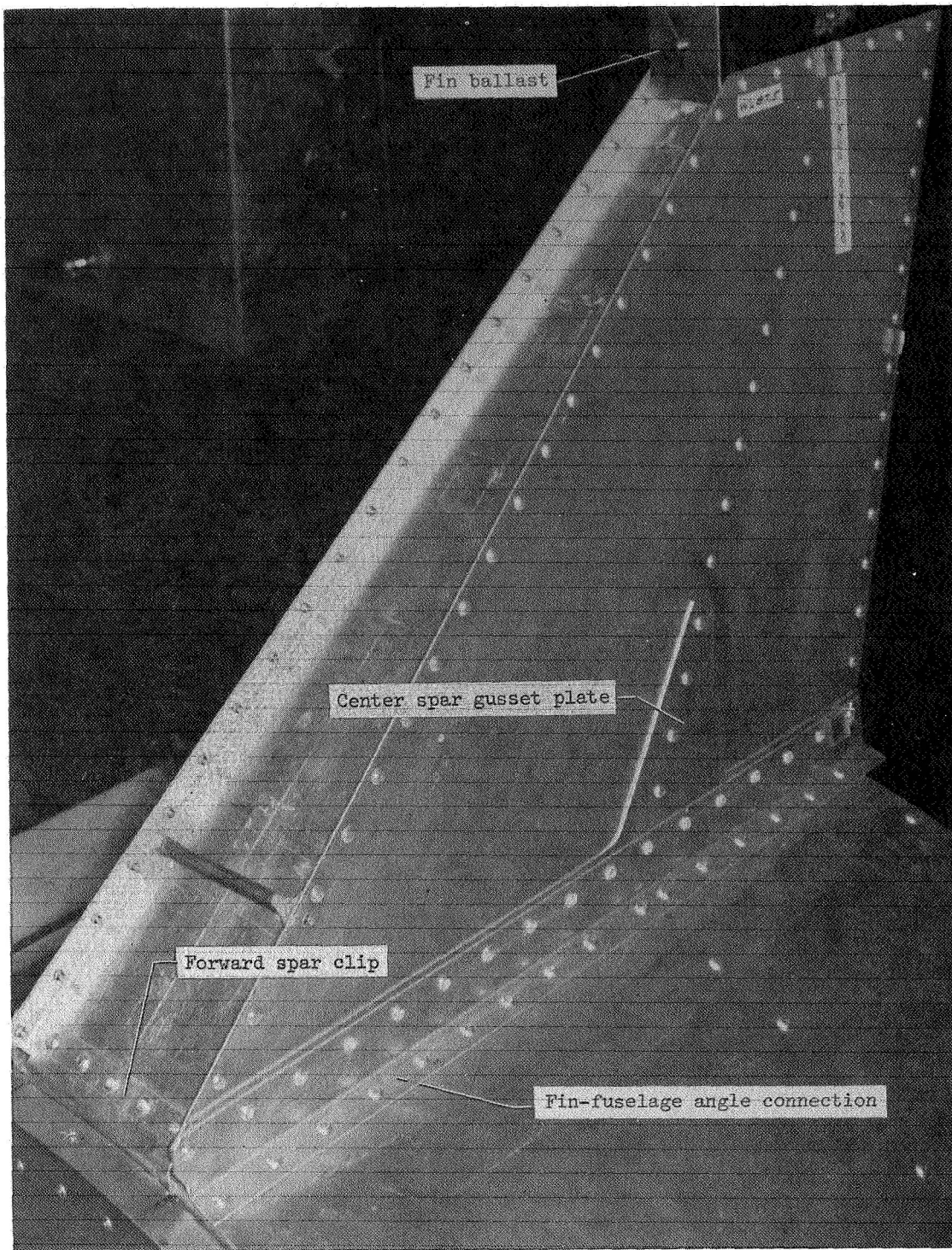
L-74-3990.1

(a) Forward and center spar connections.

Figure 23.- Fin-fuselage interface.

Aft fuselage support frame

Aft spar clip

Center spar gusset plates

Engine bulkhead
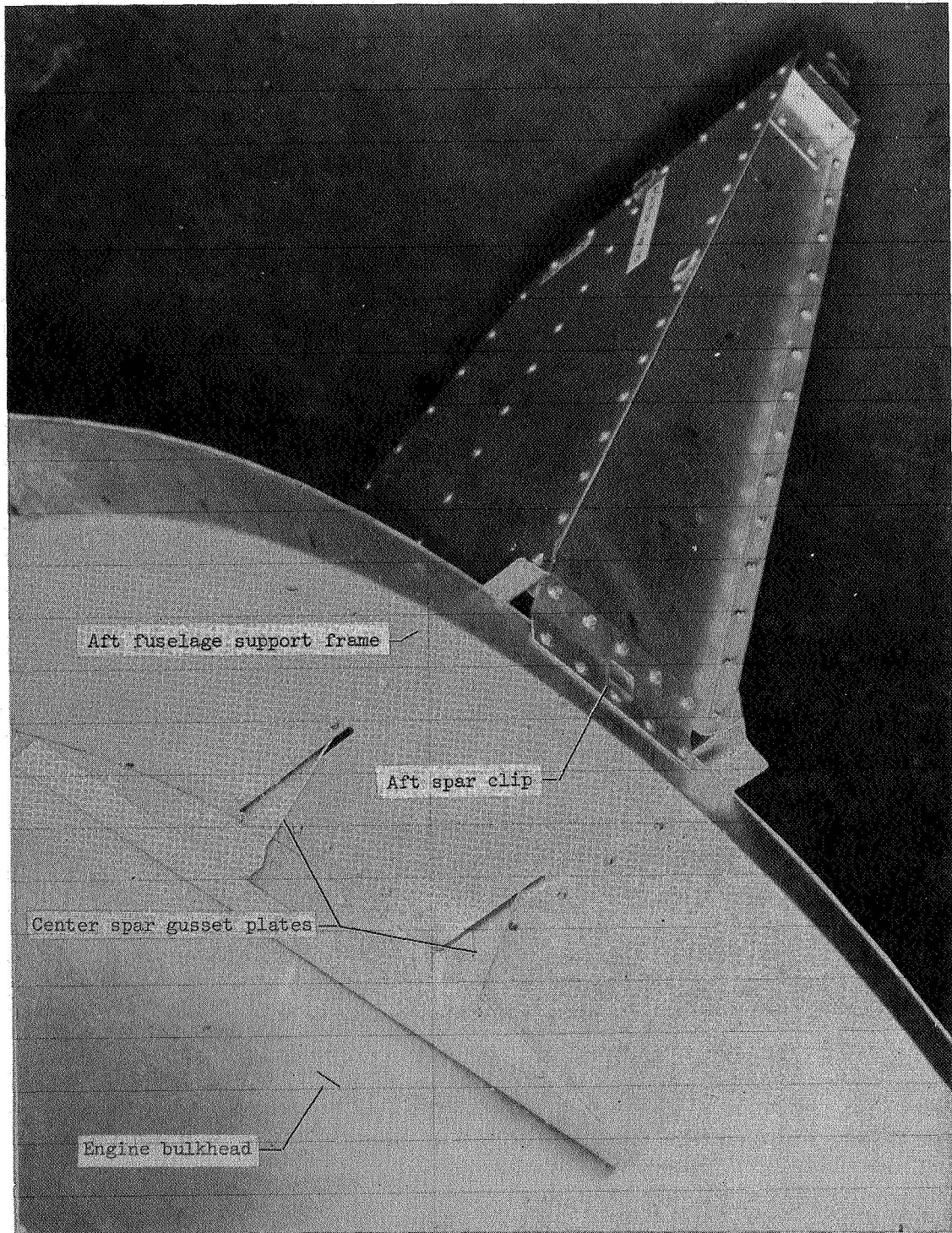
L-74-3989.1

(b) Detail of aft fin-fuselage interface connection.

Figure 23.- Concluded.

110
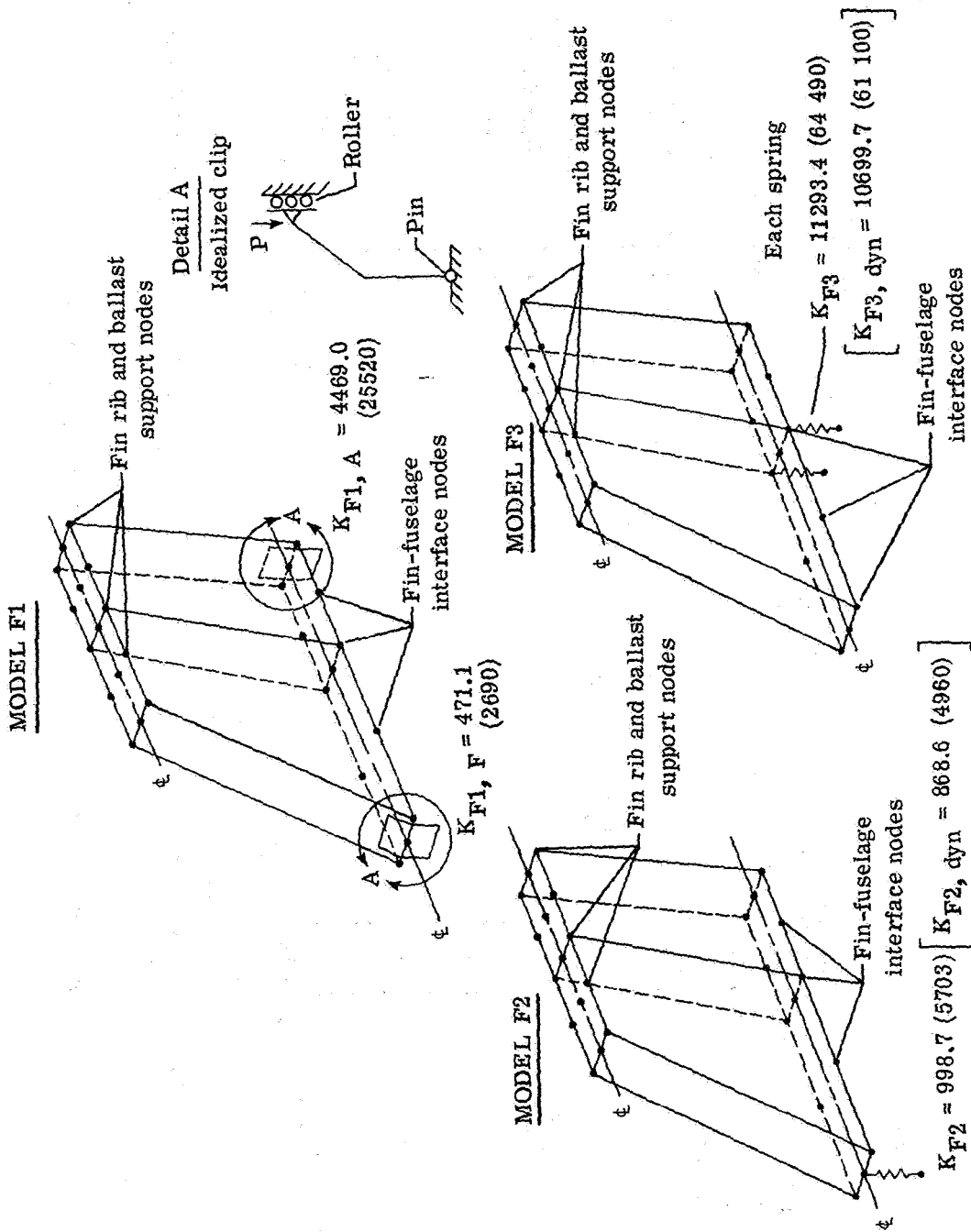
Figure 24.- Models of fin-to-fuselage joint flexibility. Units are in kN/m (lb/in.).

111
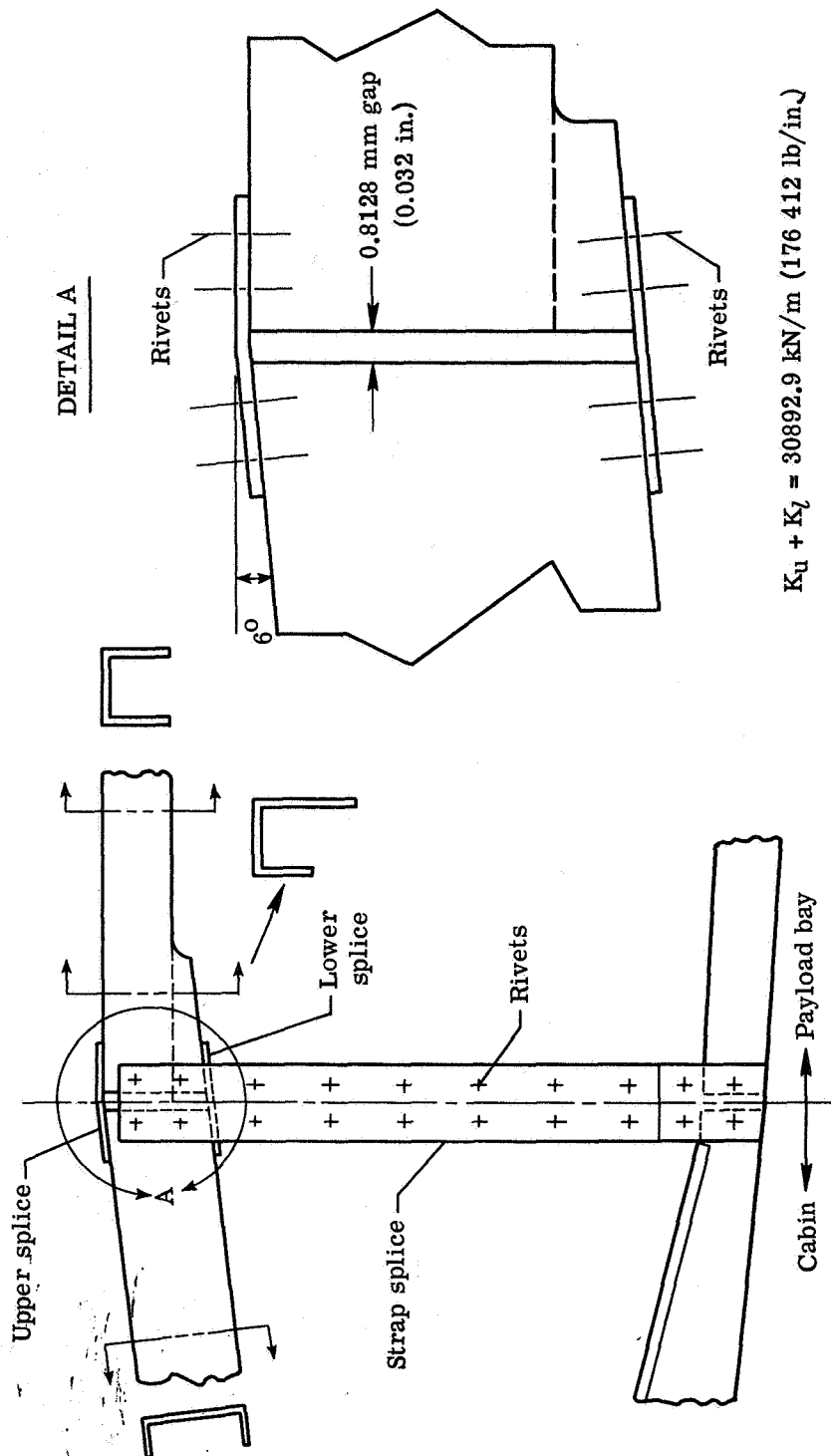
Figure 25.- Model of cabin-to-cargo-bay joint flexibility.

DETAIL A

Rivets

0.8128 mm gap
(0.032 in.)

Rivets

6°

$K_u + K_\ell = 30892.9$ kN/m (176 412 lb/in.)

Upper splice

Lower splice

Rivets

Strap splice

Cabin

Payload bay

A

112
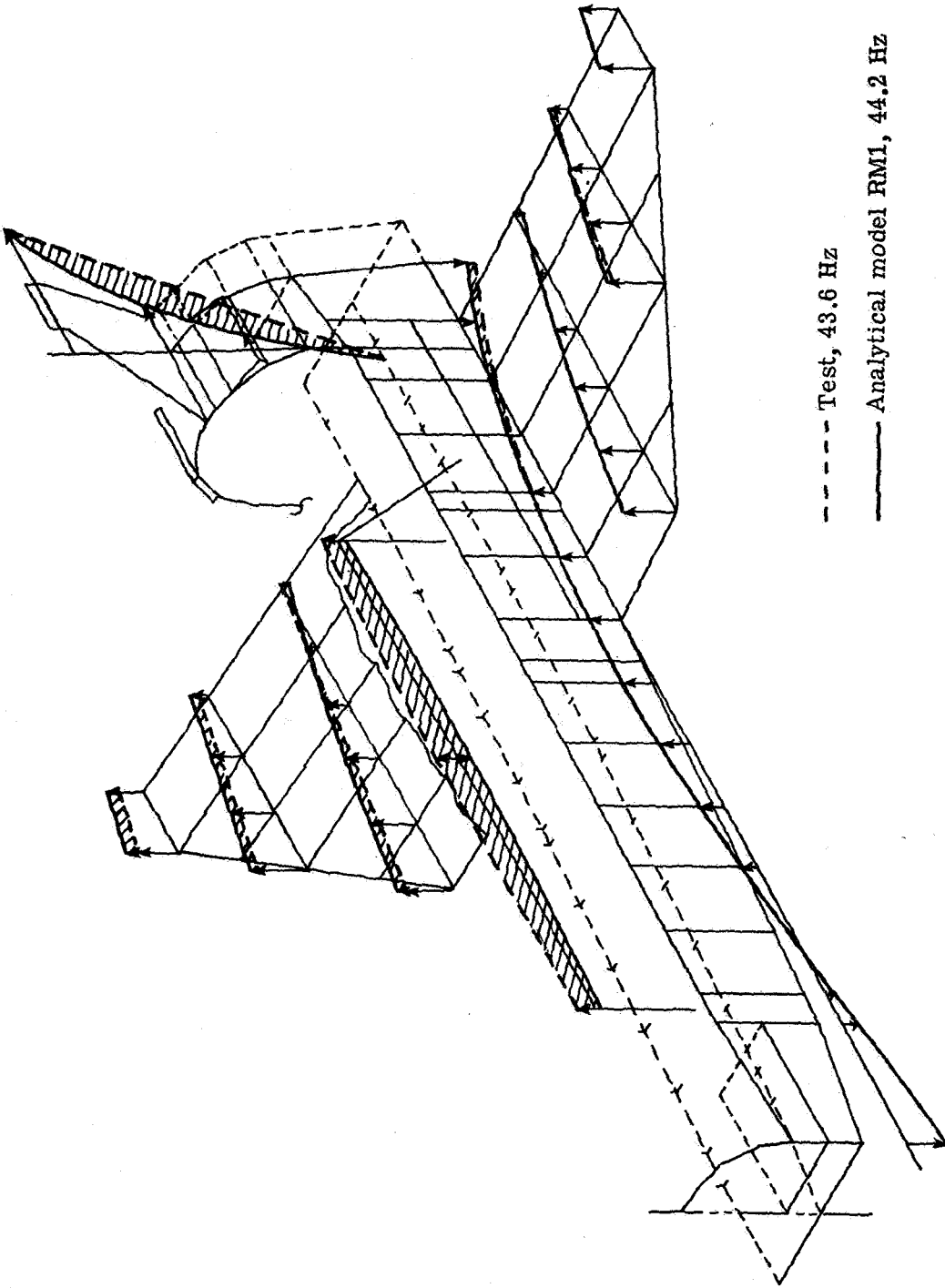
Figure 26.- Measured and analytical mode shapes of model RM1 for the orbiter first symmetric mode.

- - - - - Test, 43.6 Hz

———— Analytical model RM1, 44.2 Hz

113
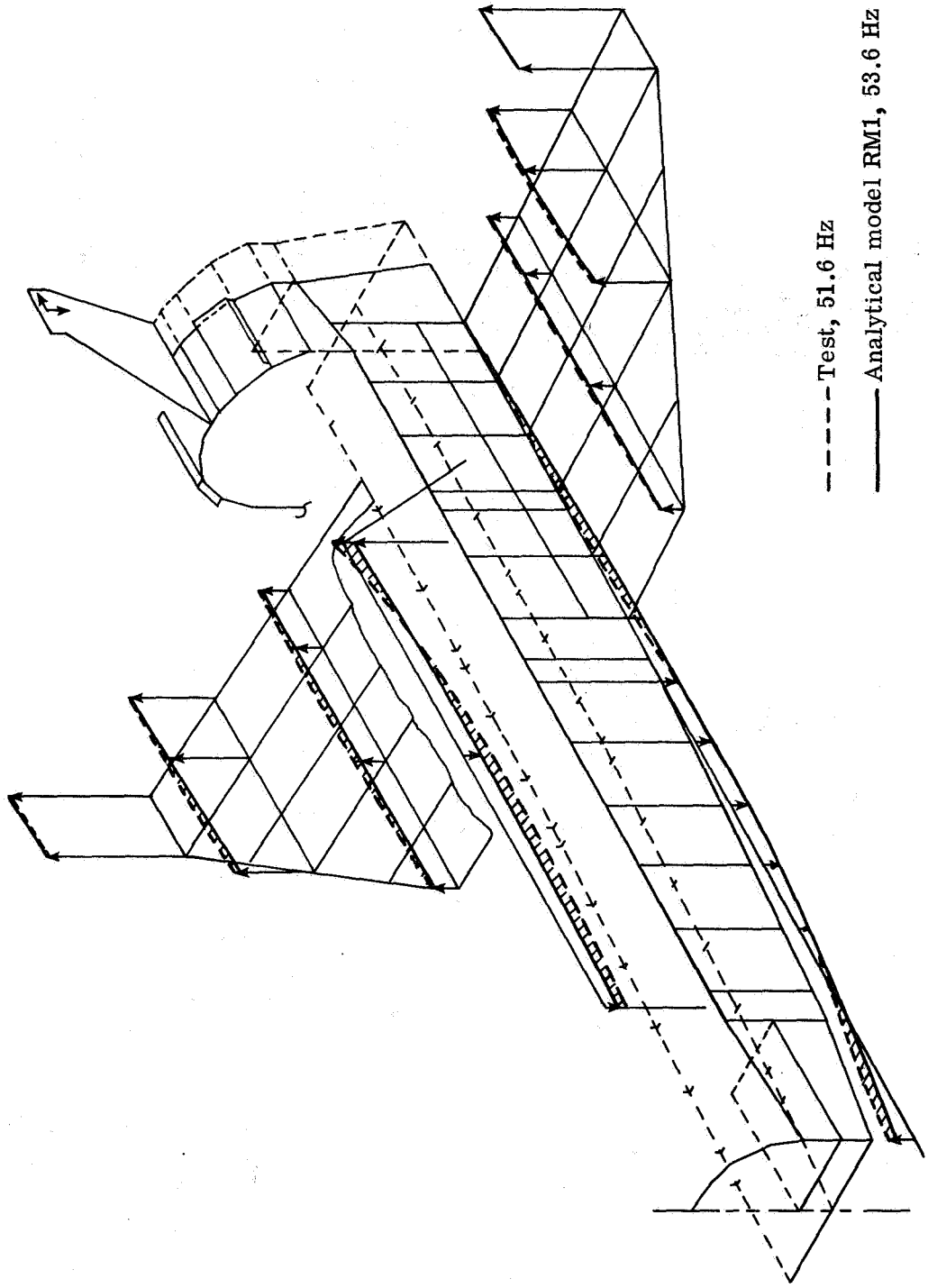
Figure 27.– Measured and analytical mode shapes of model RM1 for the orbiter second symmetric mode.

- - - - Test, 51.6 Hz

——— Analytical model RM1, 53.6 Hz
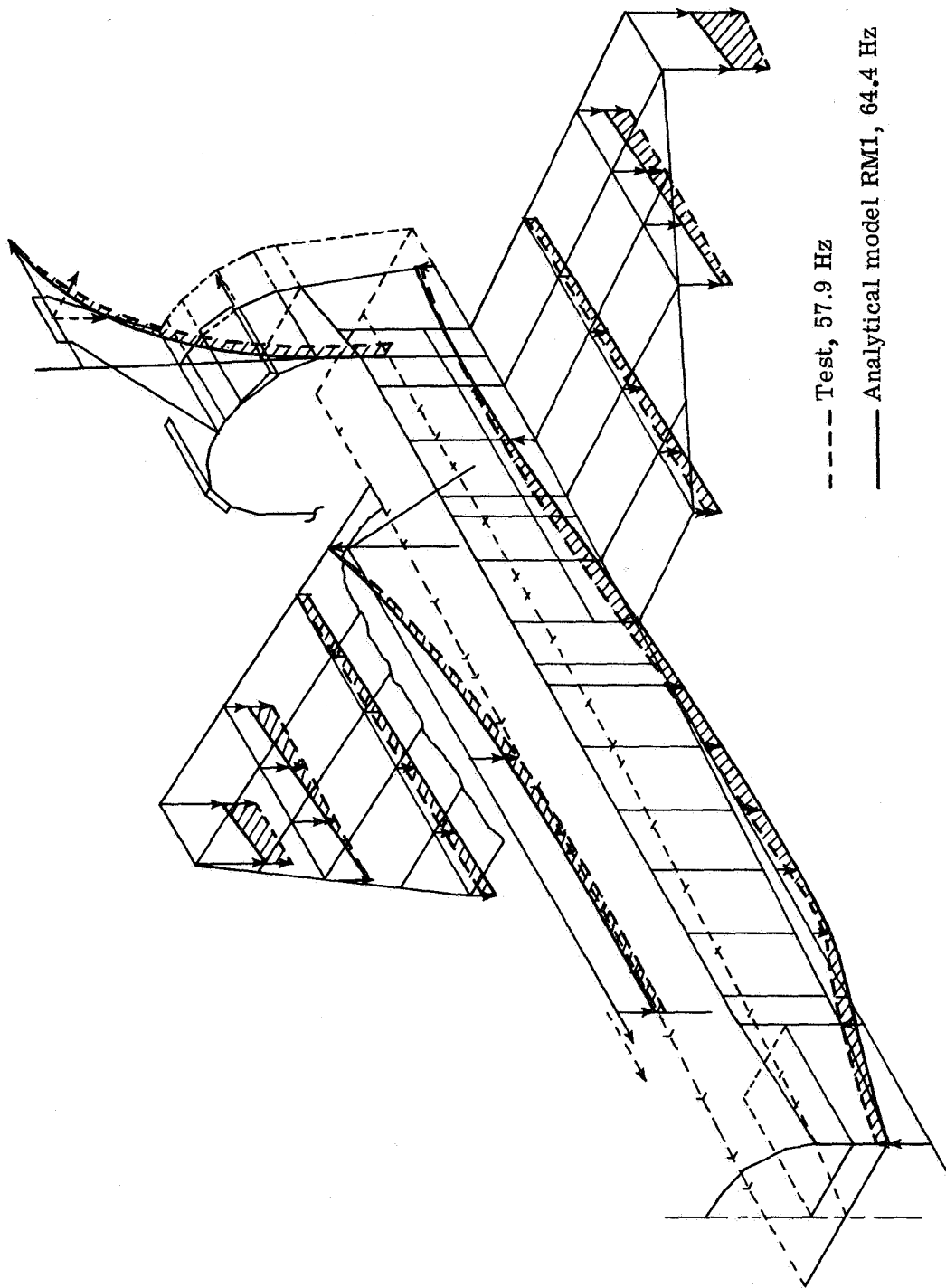
Figure 28.– Measured and analytical mode shapes of model RM1 for the orbiter third symmetric mode.

----- Test, 57.9 Hz

——— Analytical model RM1, 64.4 Hz

115
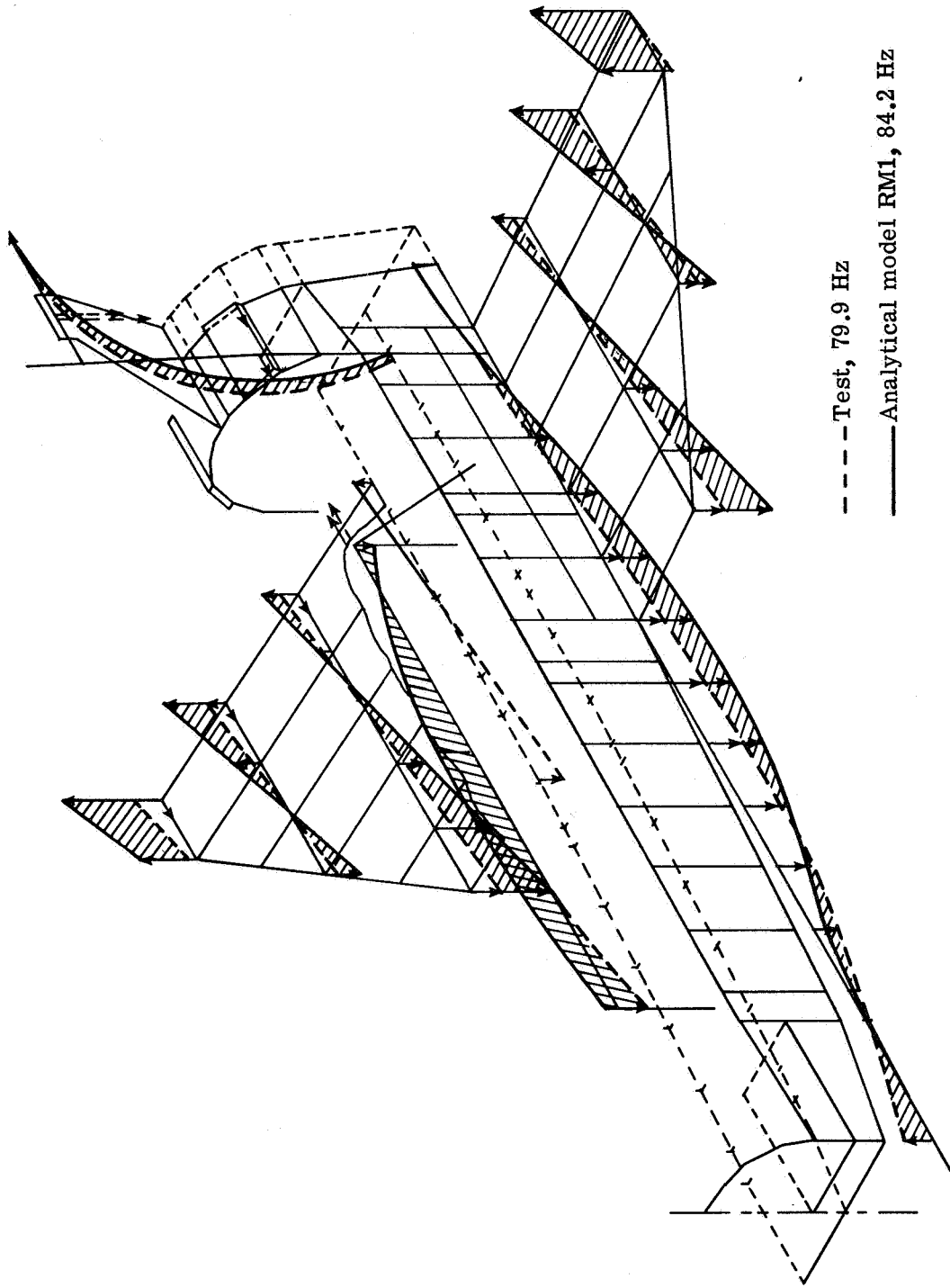
Figure 29. – Measured and analytical mode shapes of model RM1 for the orbiter fourth symmetric mode.

----- Test, 79.9 Hz

——— Analytical model RM1, 84.2 Hz

116
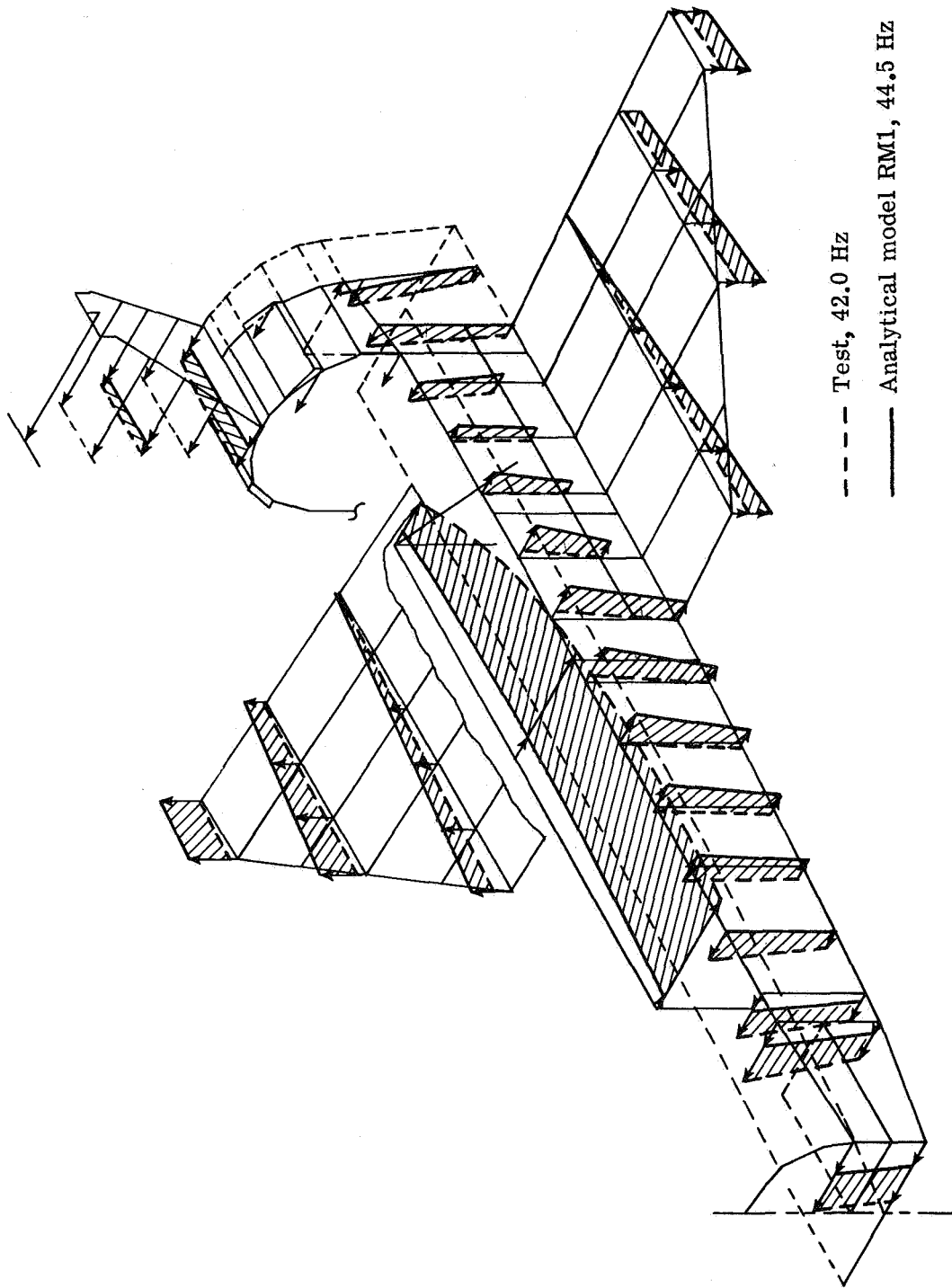
Figure 30. - Measured and analytical mode shapes of model RM1 for the orbiter first antisymmetric mode.

---- Test, 42.0 Hz

—— Analytical model RM1, 44.5 Hz

117
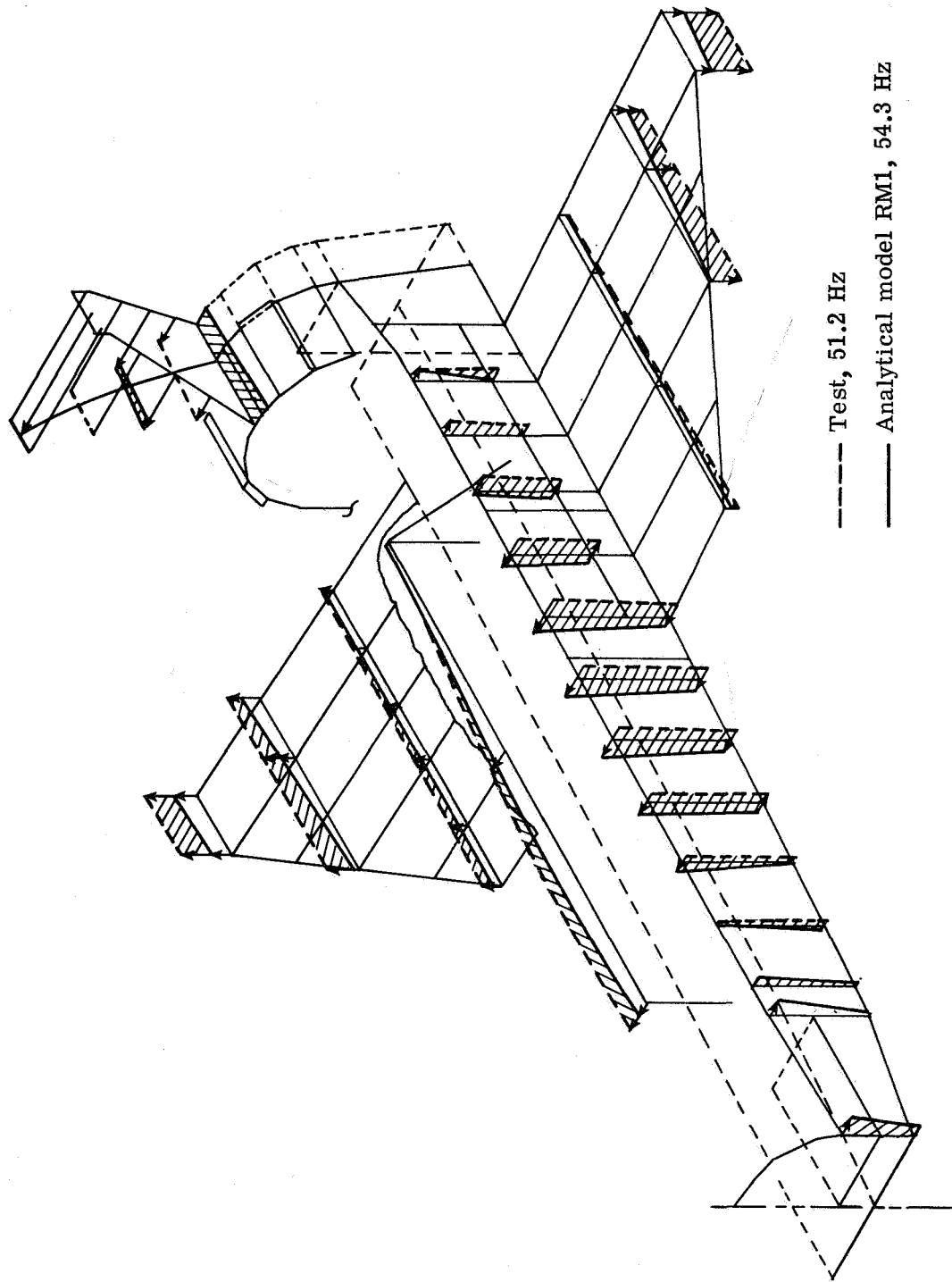
Figure 31.- Measured and analytical mode shapes of model RM1 for the orbiter second antisymmetric mode.

- - - - - Test, 51.2 Hz

——— Analytical model RM1, 54.3 Hz
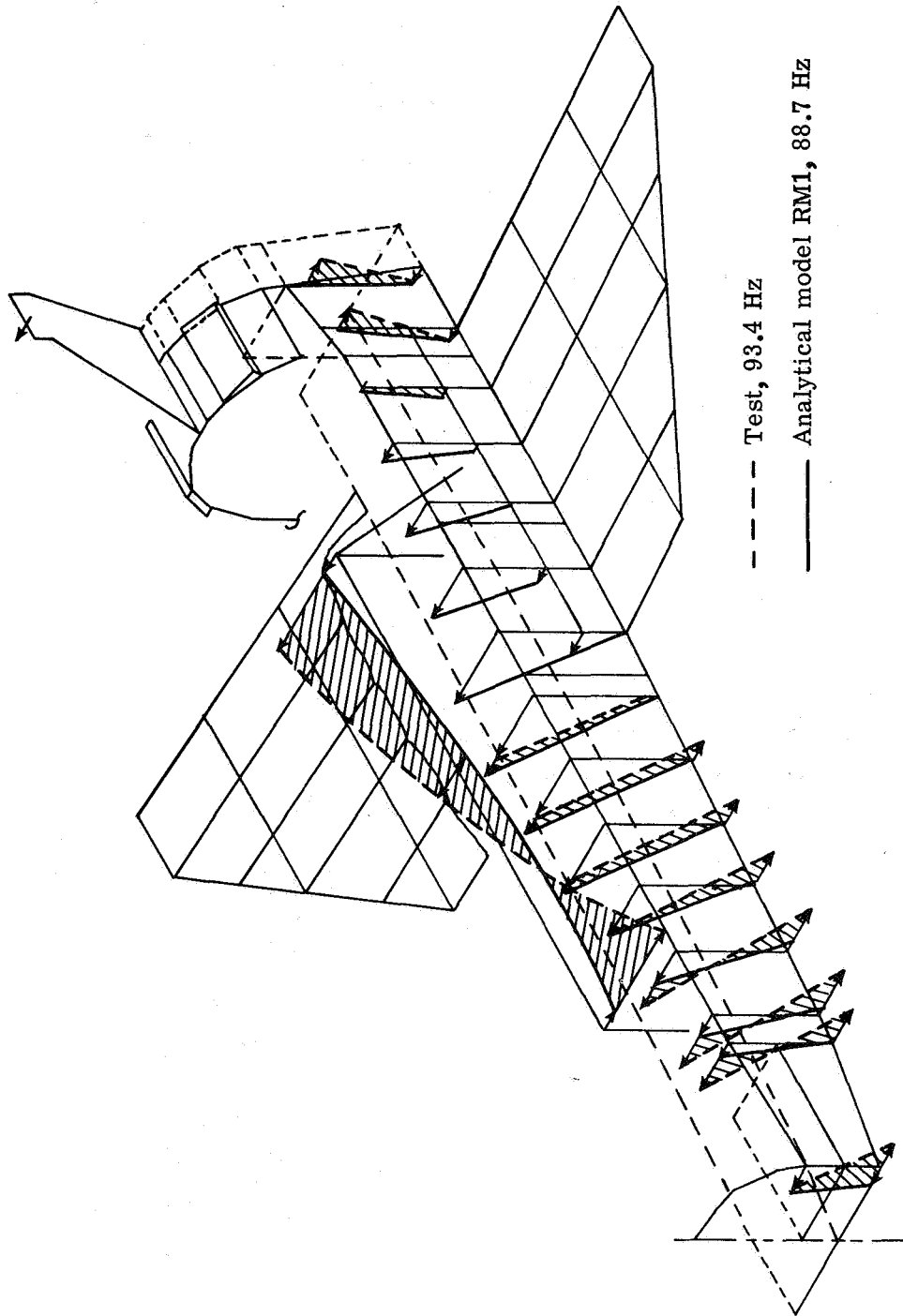
(a) Lateral motion (y-direction).

Figure 32.– Measured and analytical mode shapes of model RM1 for the orbiter fifth antisymmetric mode.

——— Test, 93.4 Hz

——— Analytical model RM1, 88.7 Hz

119

----- Test, 93.4 Hz

——— Analytical model RM1, 88.7 Hz
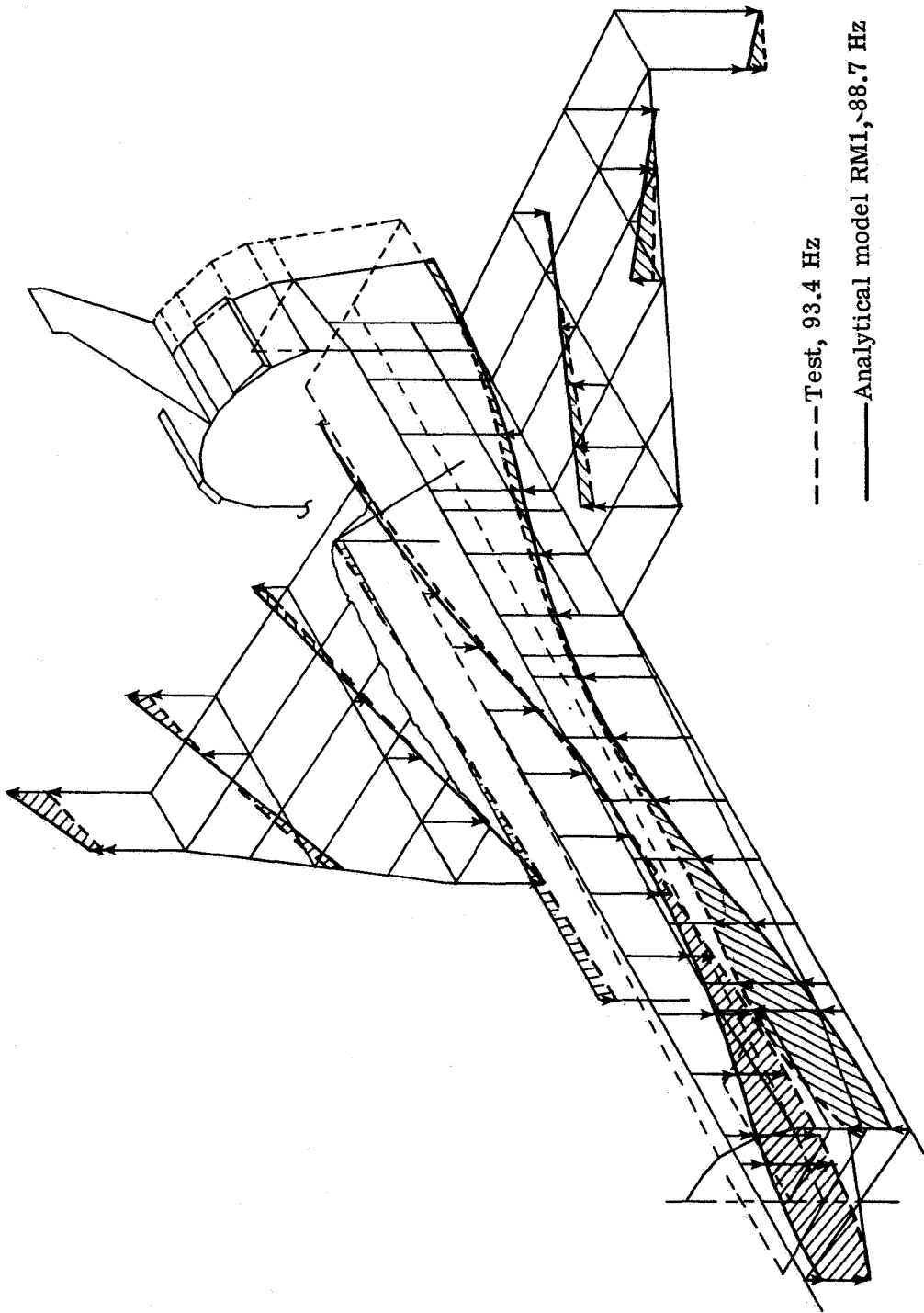
(b) Vertical motion (z-direction).

Figure 32.- Concluded.
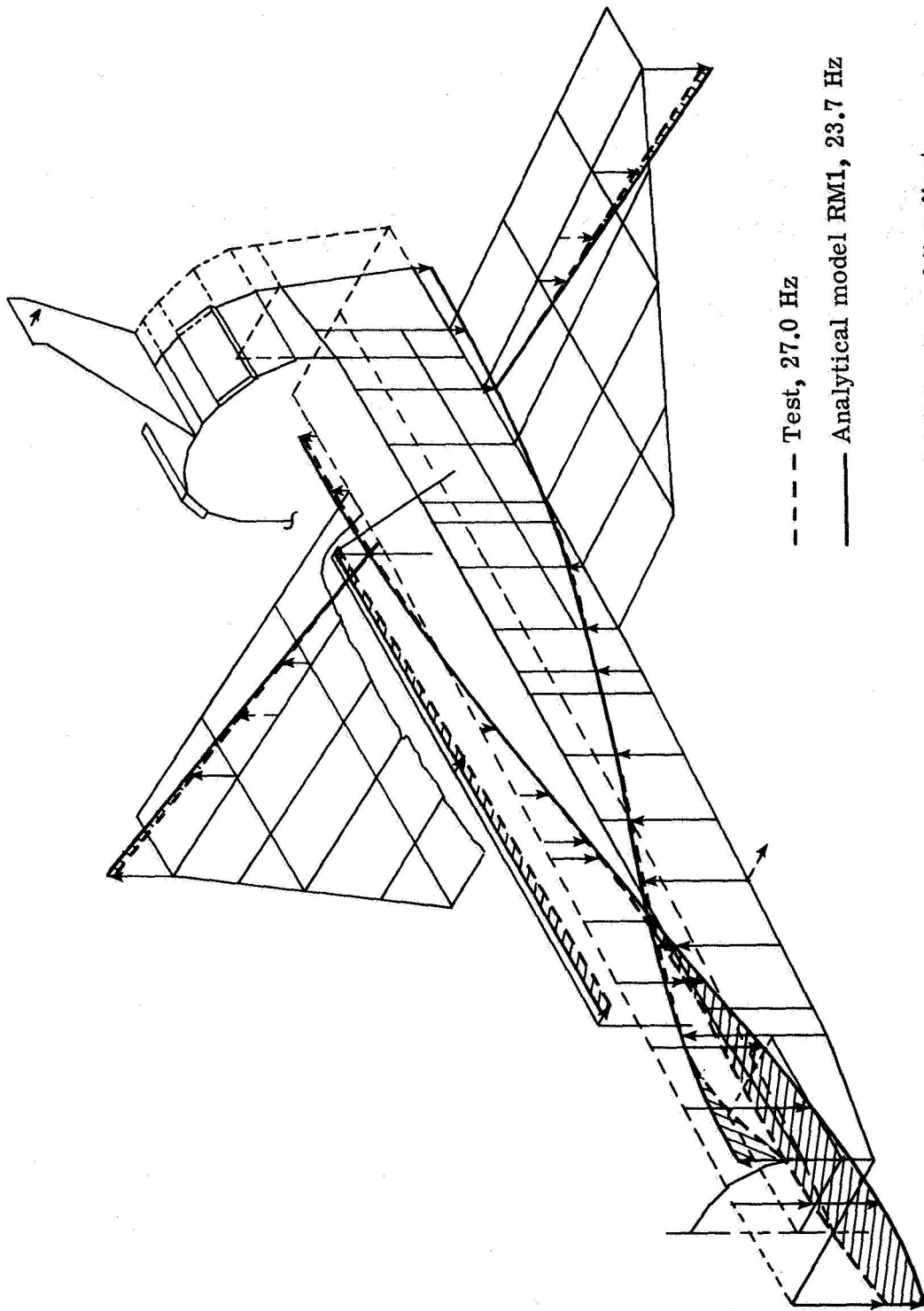
Figure 33.- Measured and analytical mode shapes of model RM1 for the orbiter first torsional mode with the cargo door removed.

----- Test, 27.0 Hz

——— Analytical model RM1, 23.7 Hz
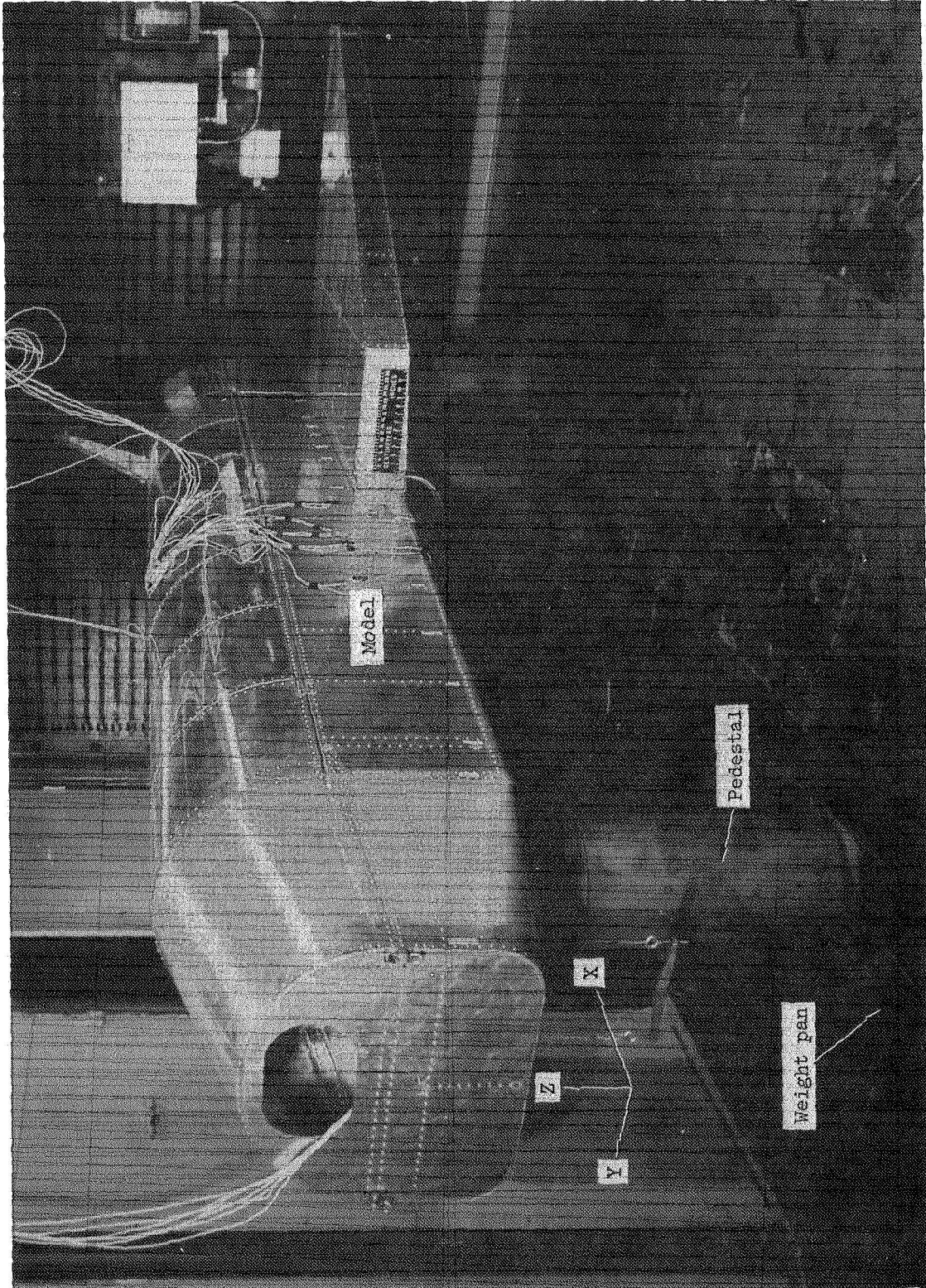
Figure 34.- Support of 1/8-scale orbiter model for static-load tests.

Model

Pedestal

X

Z

Y

Weight pan

L-74-1942.1

122
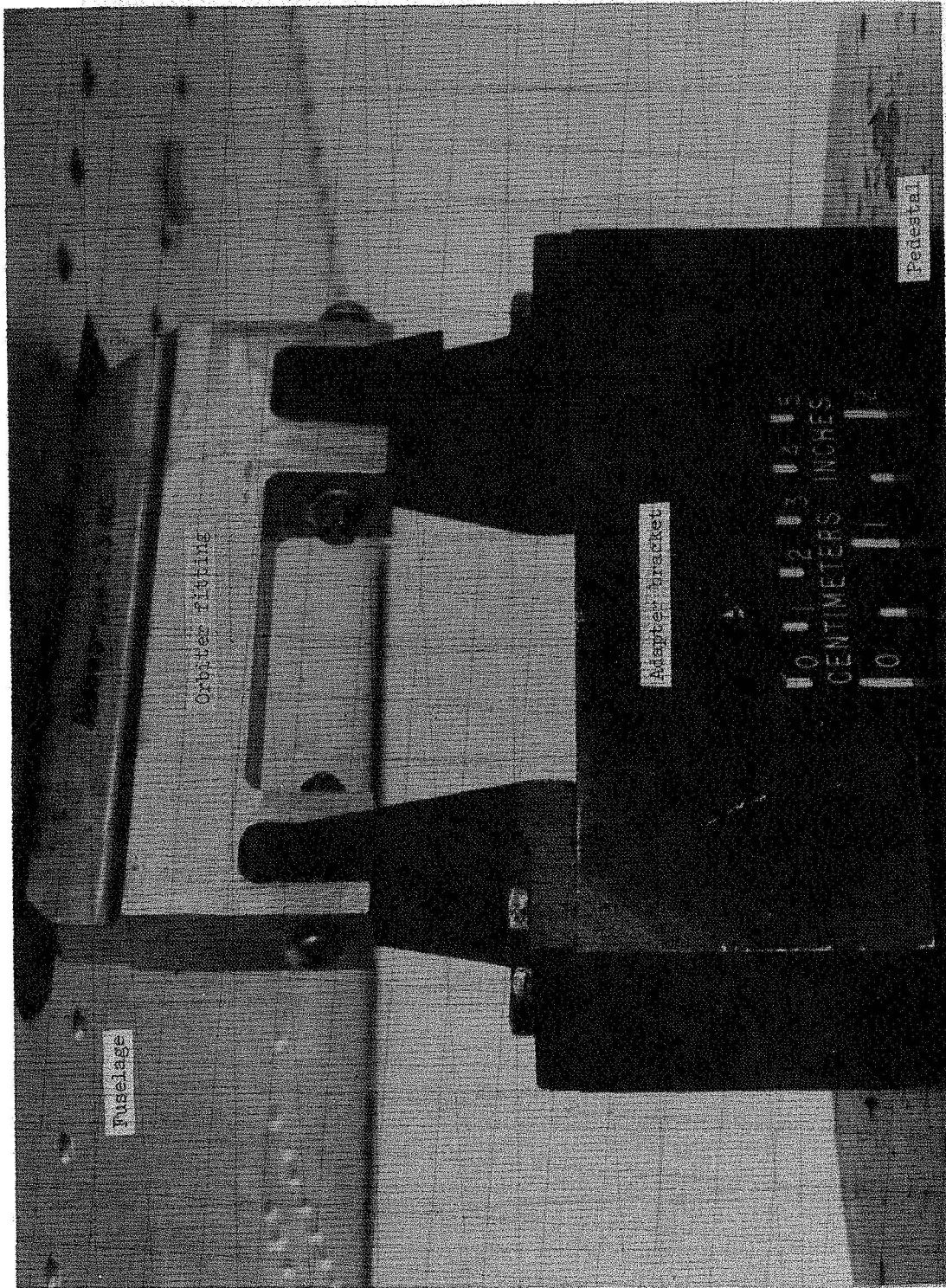
L-74-1945.1

(a) Forward fuselage connection.

Figure 35.- Orbiter-model interstage fittings.

Fuselage

Orbiter fitting

Adapter bracket

Pedestal
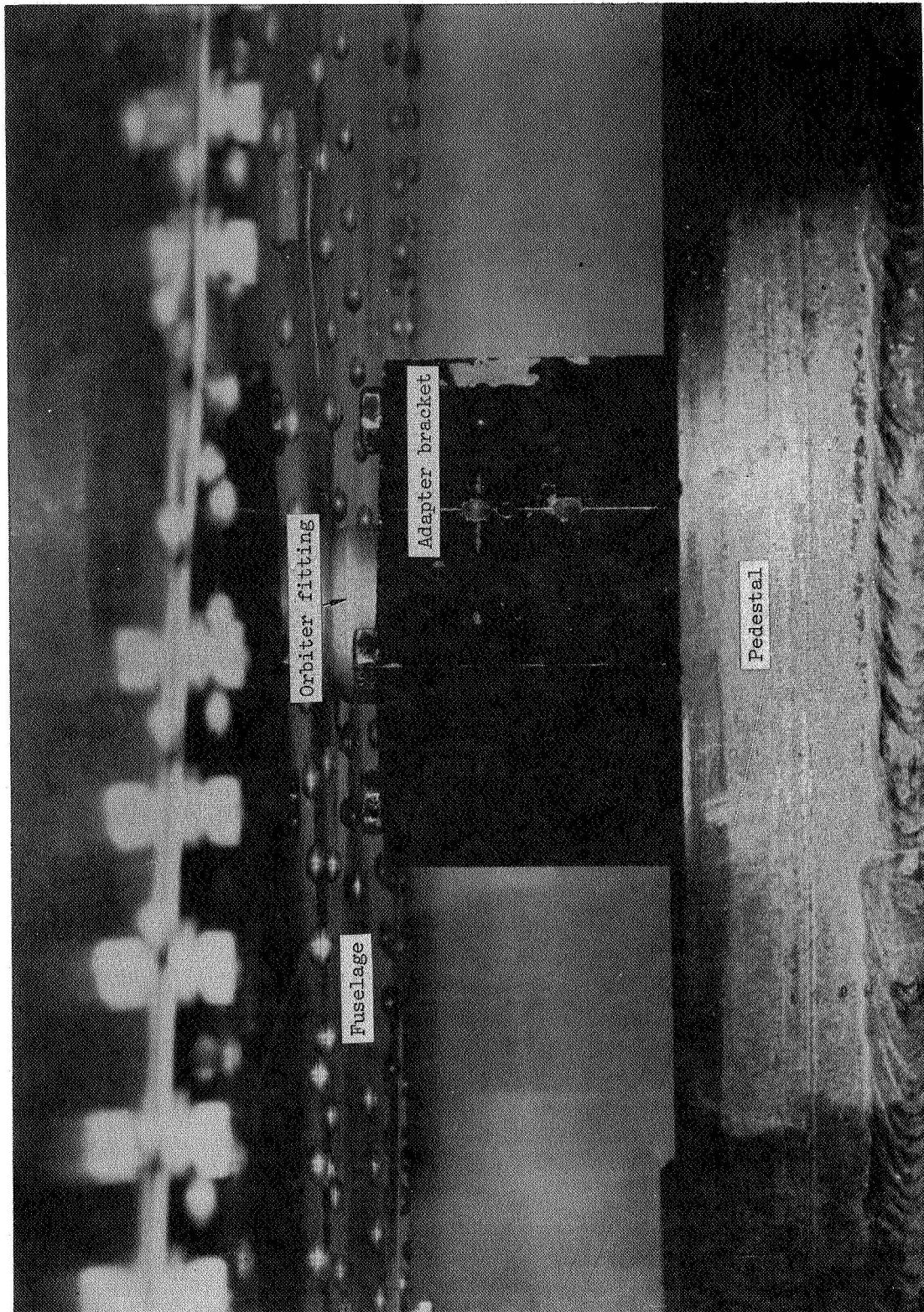
(b) Aft fuselage connection.

Figure 35.- Continued.

Wing

Orbiter fitting

Adapter bracket

Pedestal
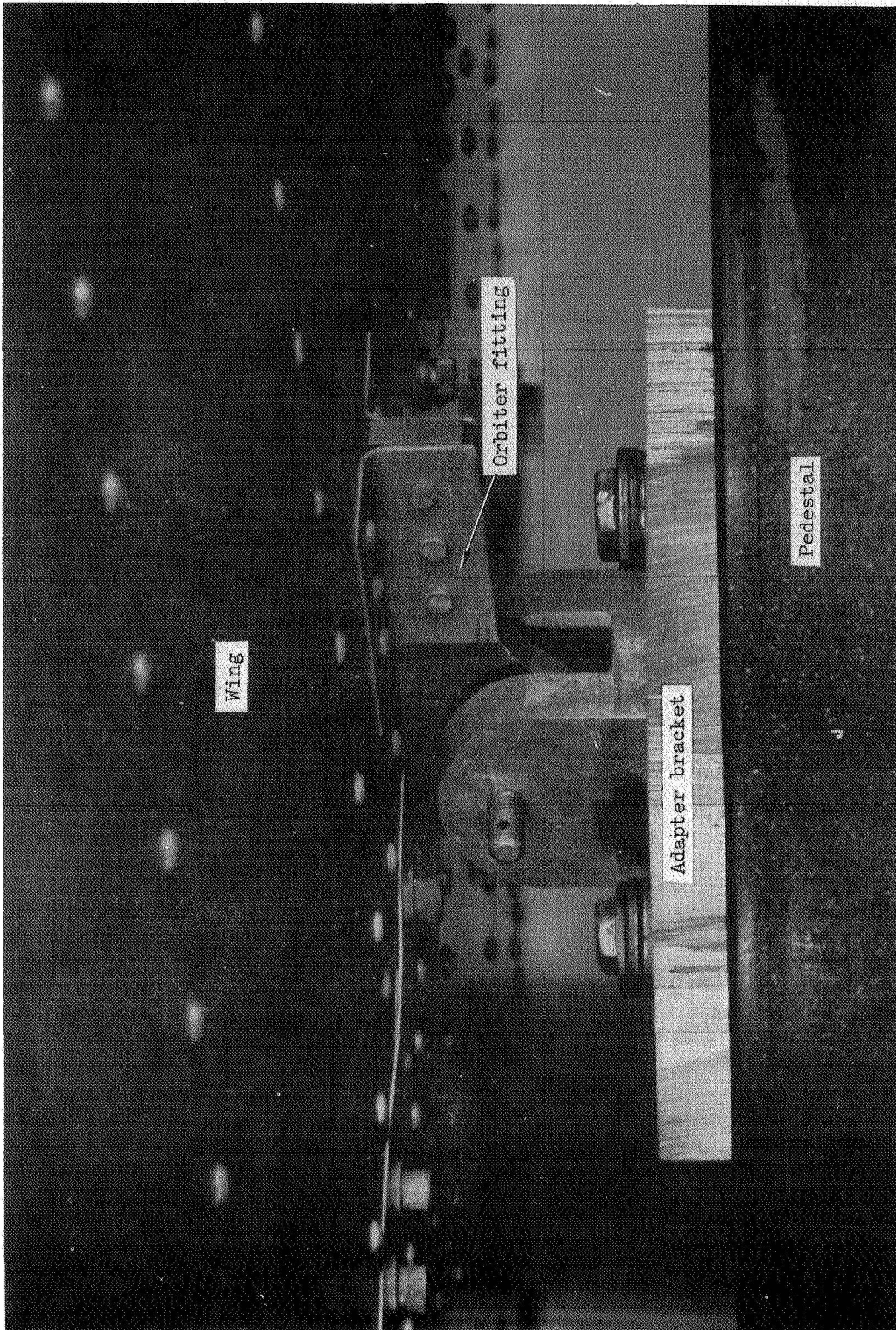
L-74-1943.1

(c) Aft wing connection.

Figure 35.- Concluded.
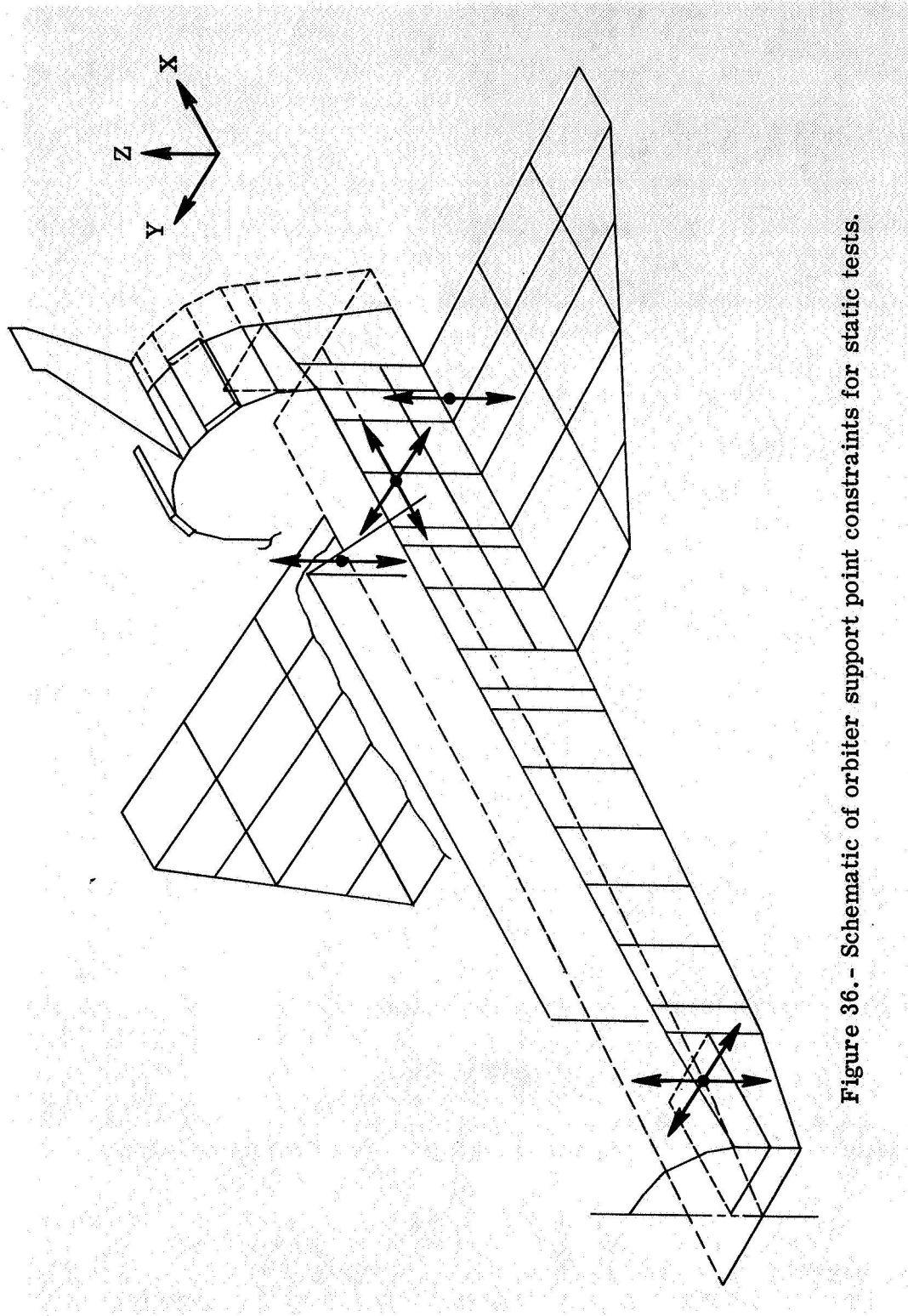
Figure 36.- Schematic of orbiter support point constraints for static tests.
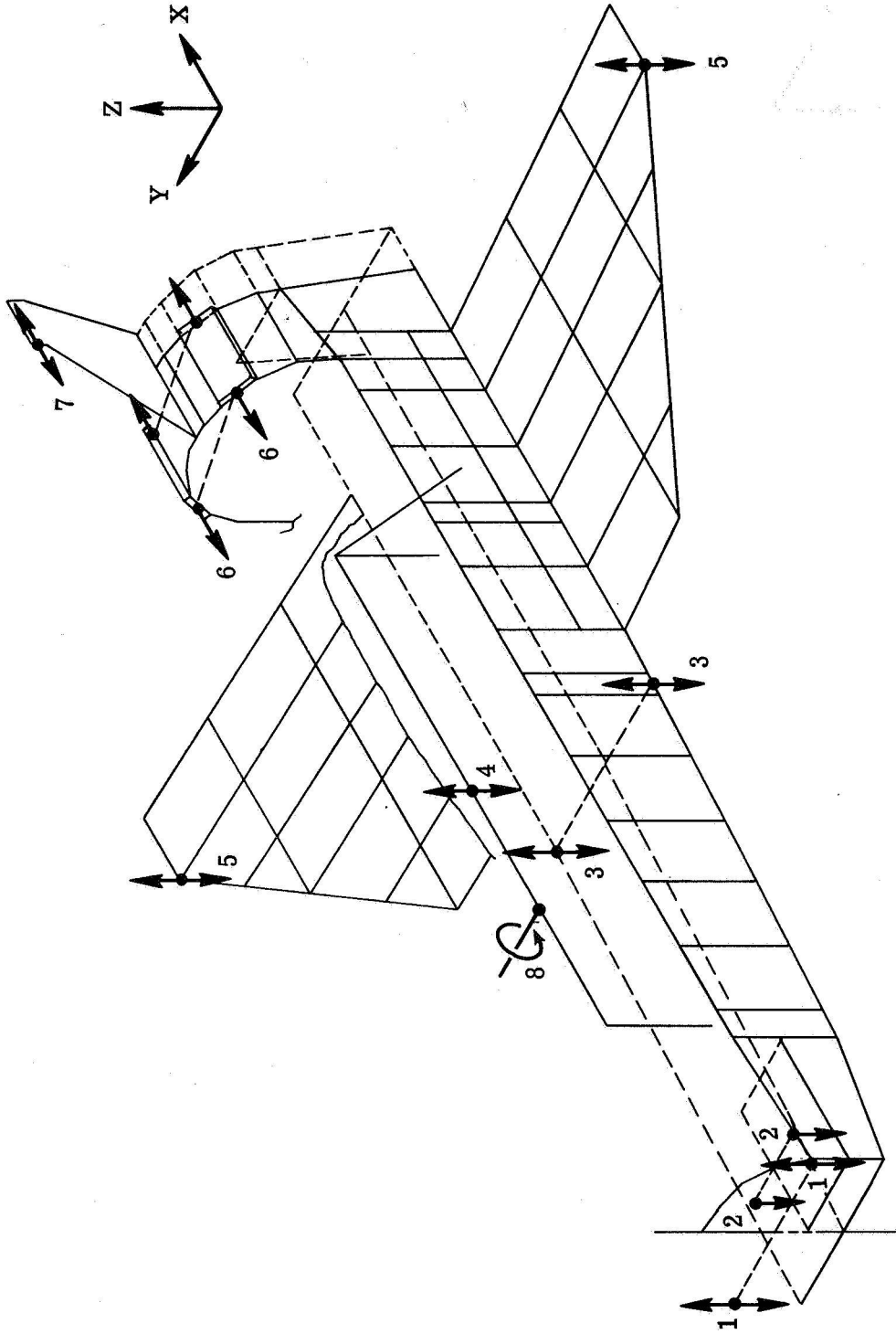
(a) Symmetric.

Figure 37.– Schematic of load application points and loading directions. (See tables IX, X, and XI.)
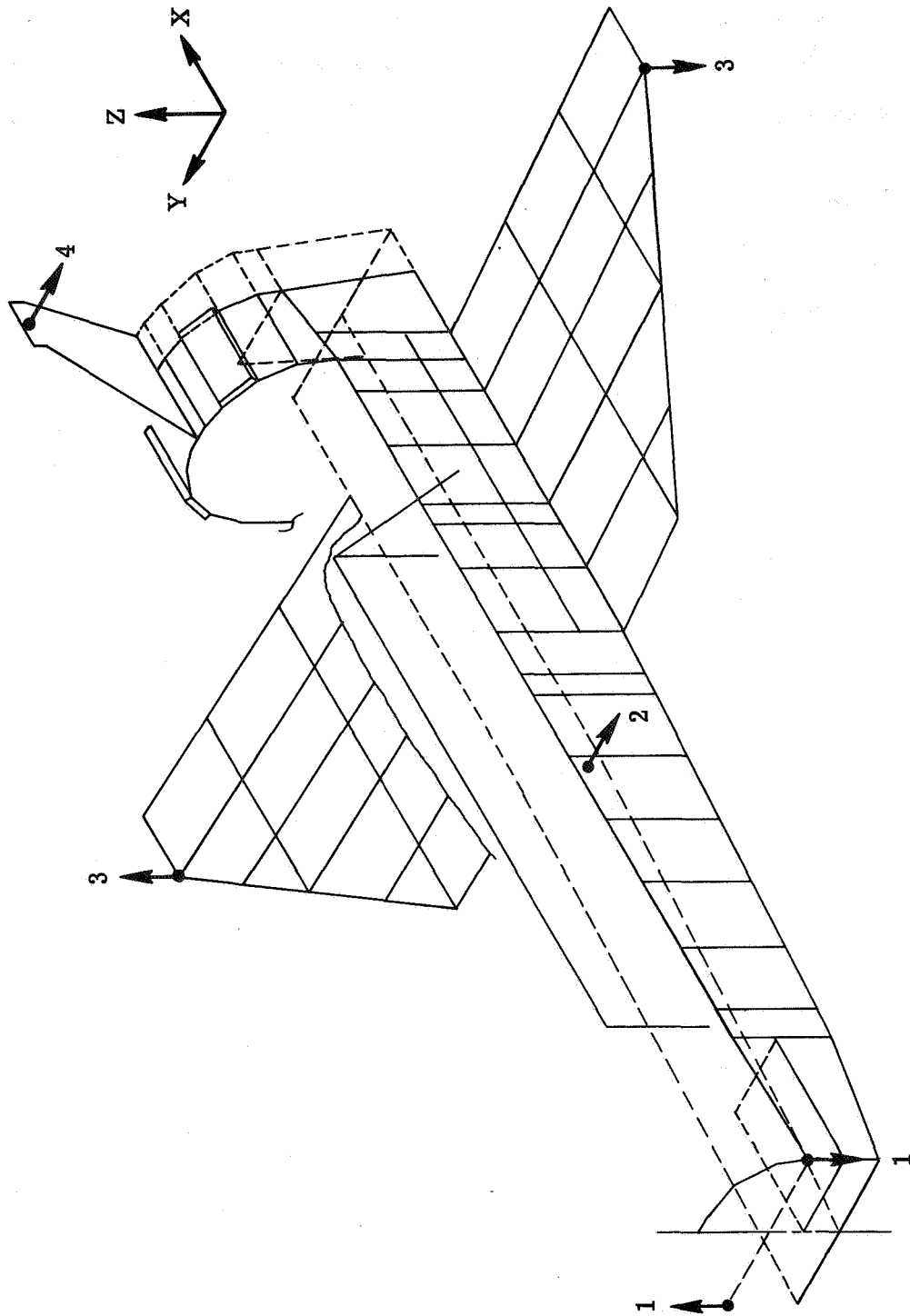
(b) Antisymmetric.

Figure 37.- Concluded.
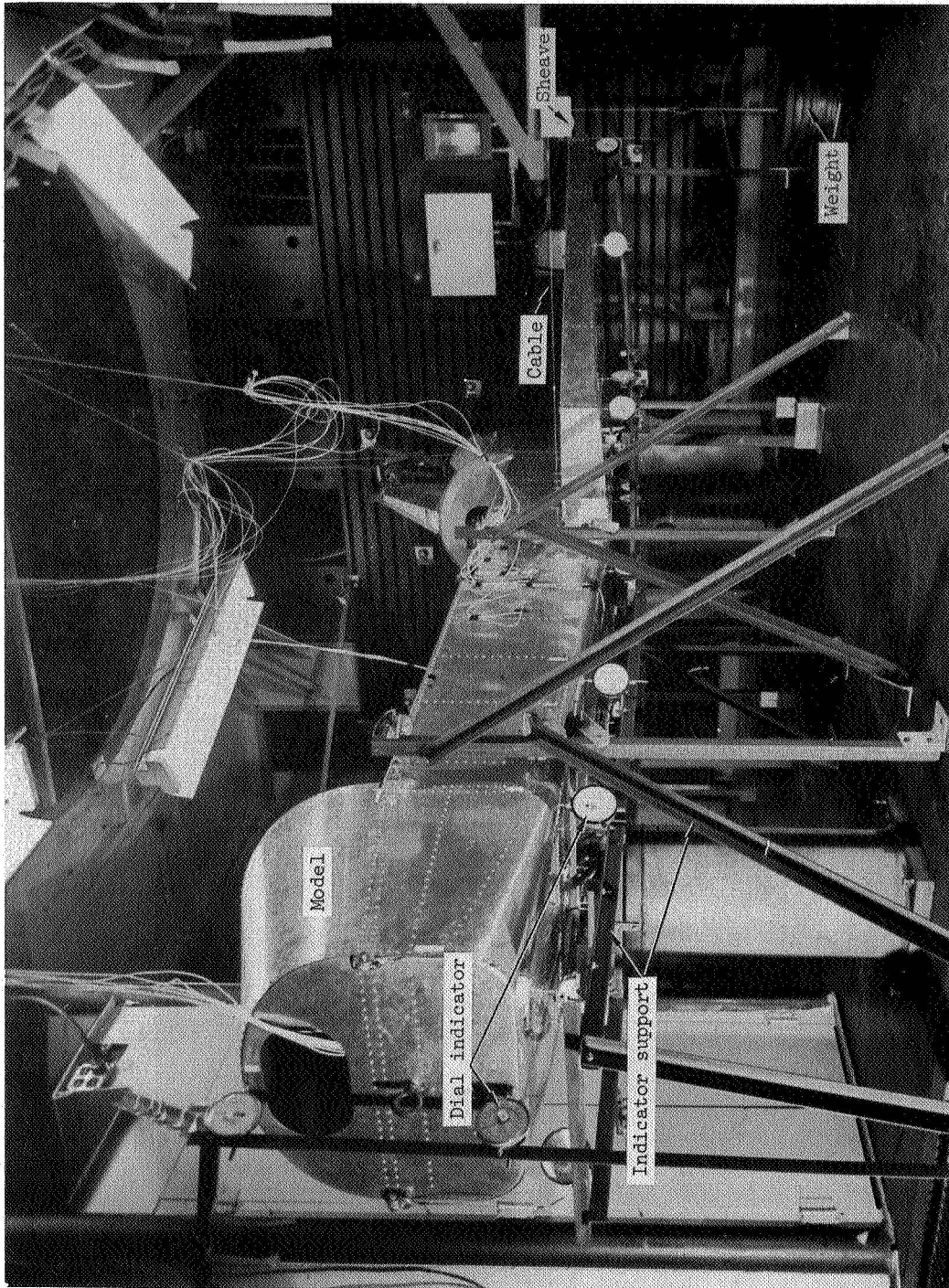
(a) Forward fuselage.

Figure 38.- Typical loading apparatus and dial-indicator setup for static-load tests.

Model

Dial indicator

Indicator support

Weight
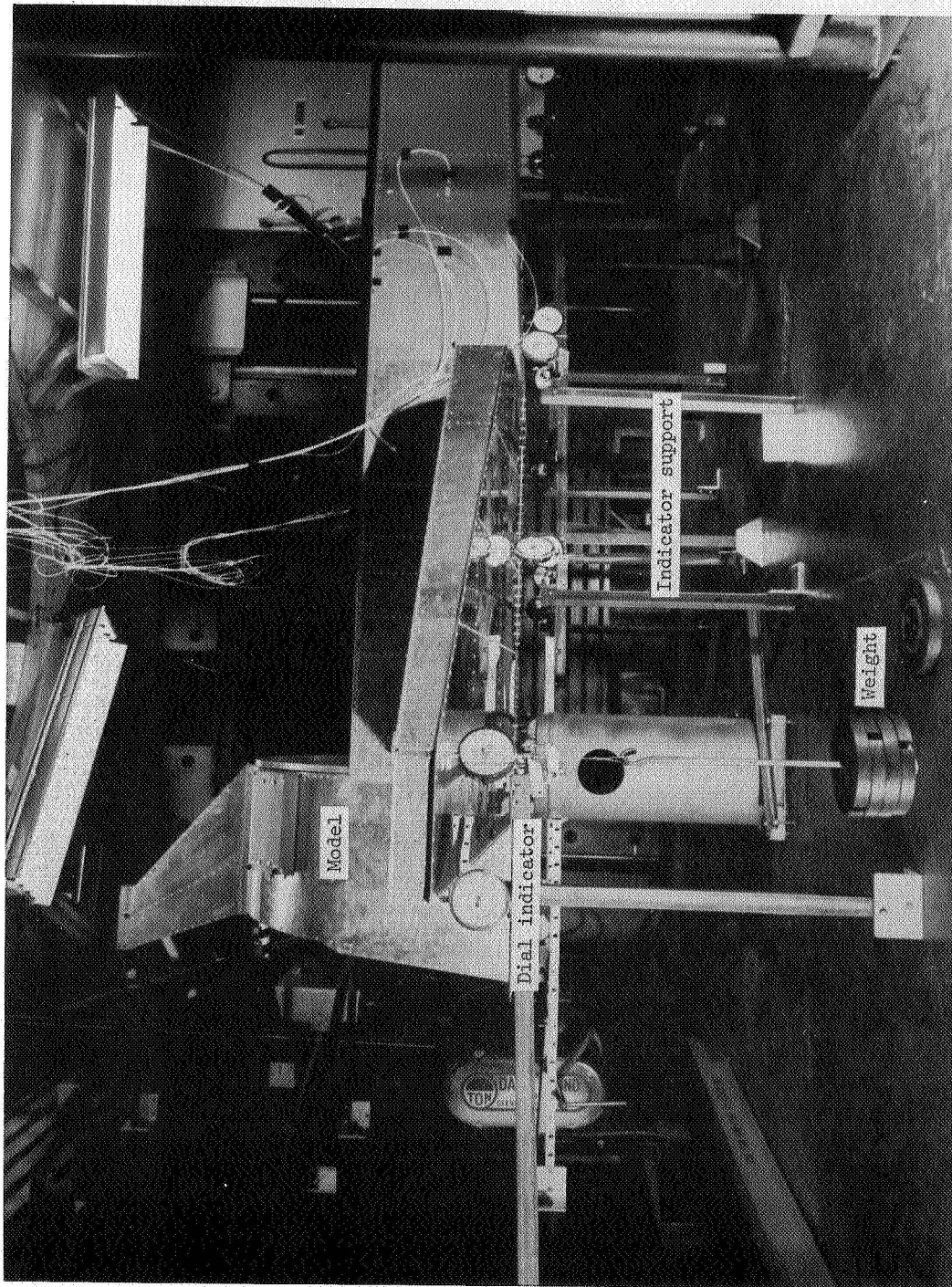
L-74-1526.1

(b) Aft fuselage wing.

Figure 38.- Concluded.
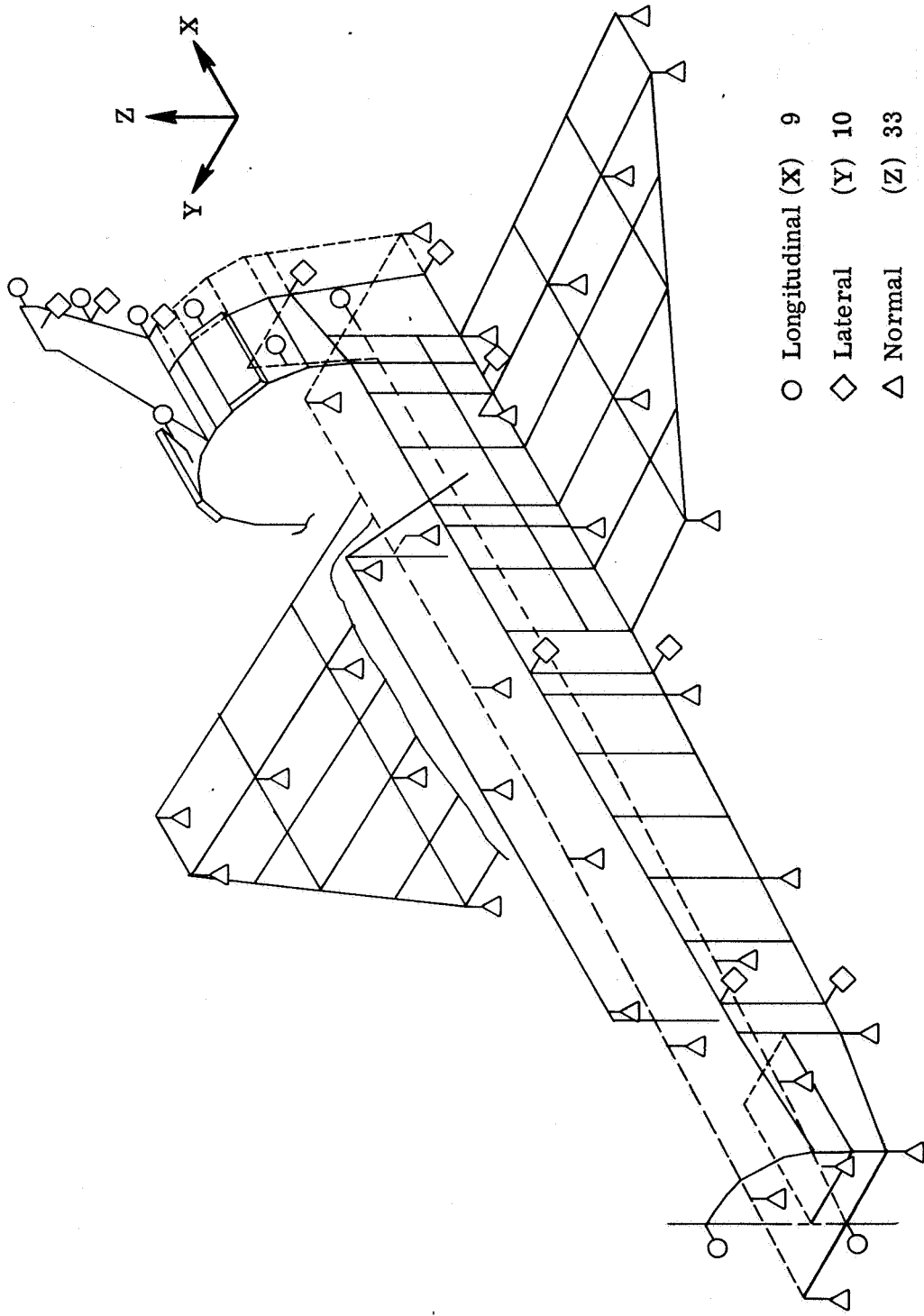
Figure 39.- Schematic of basic dial-indicator locations for deflection measurement.

○ Longitudinal (X)   9
◇ Lateral   (Y) 10
△ Normal   (Z) 33
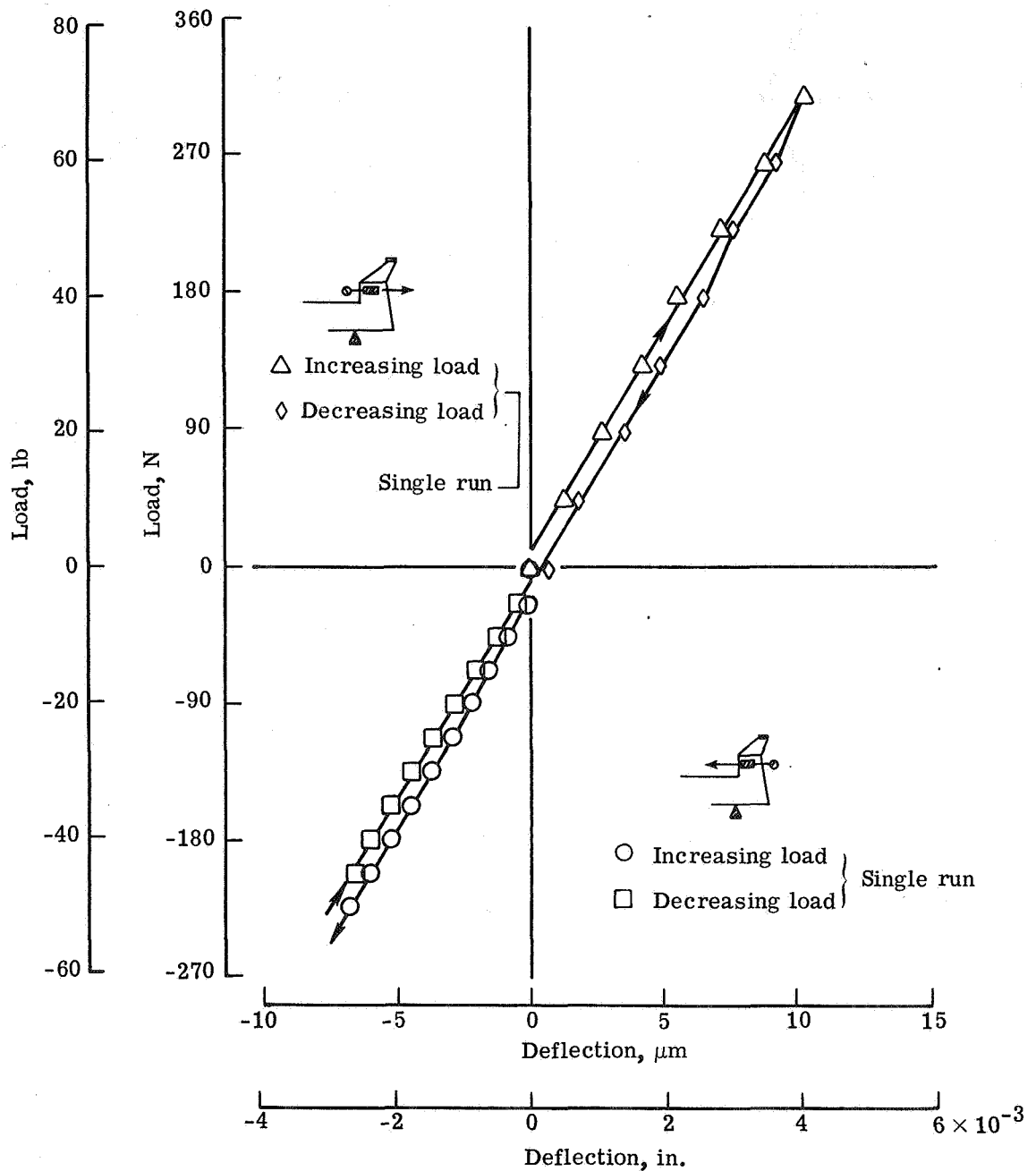
(a) Deflections at loading point.

Figure 40.- Typical static-load deflection curves.
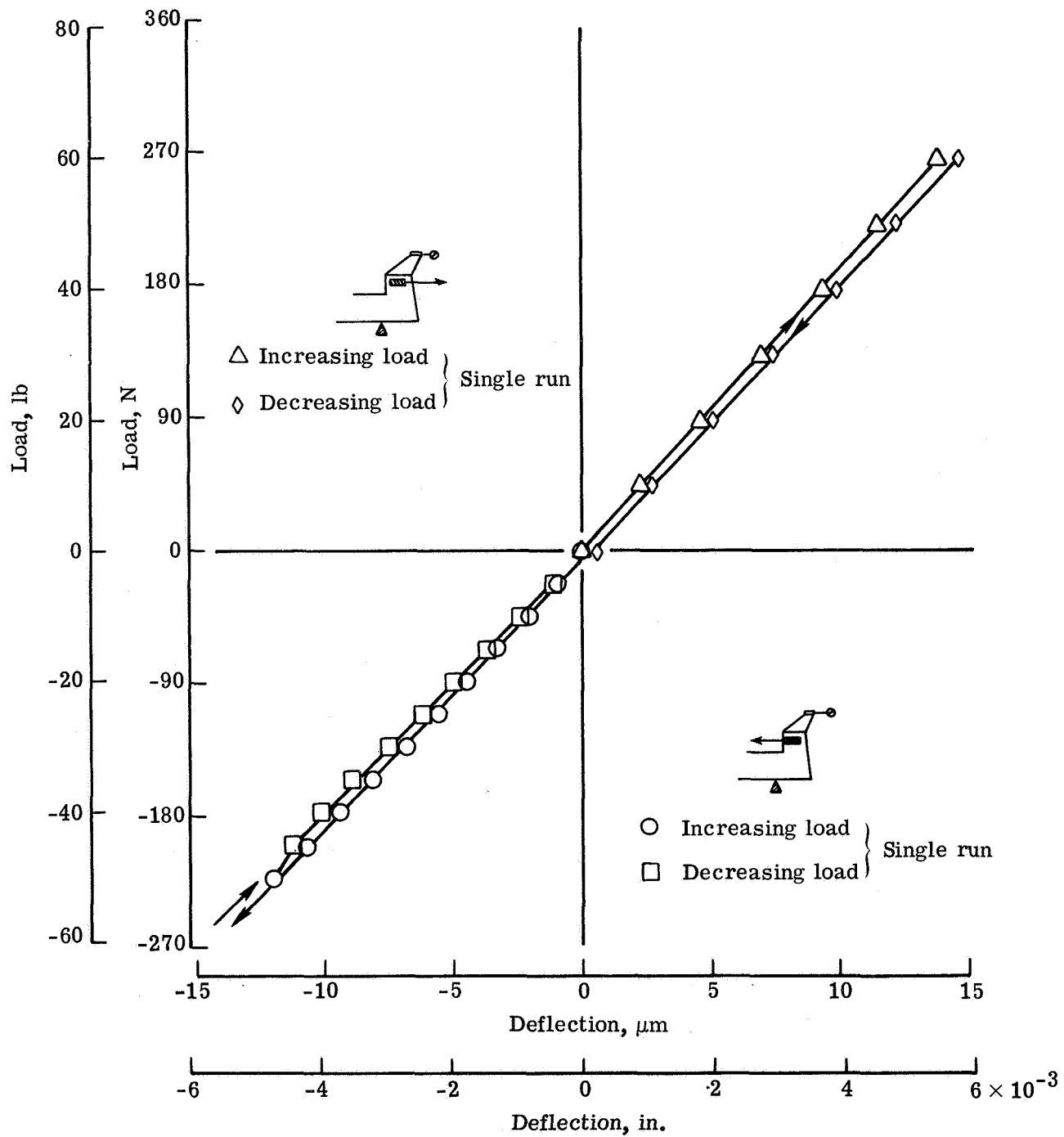
(b) Deflections at fin tip.

Figure 40.- Continued.
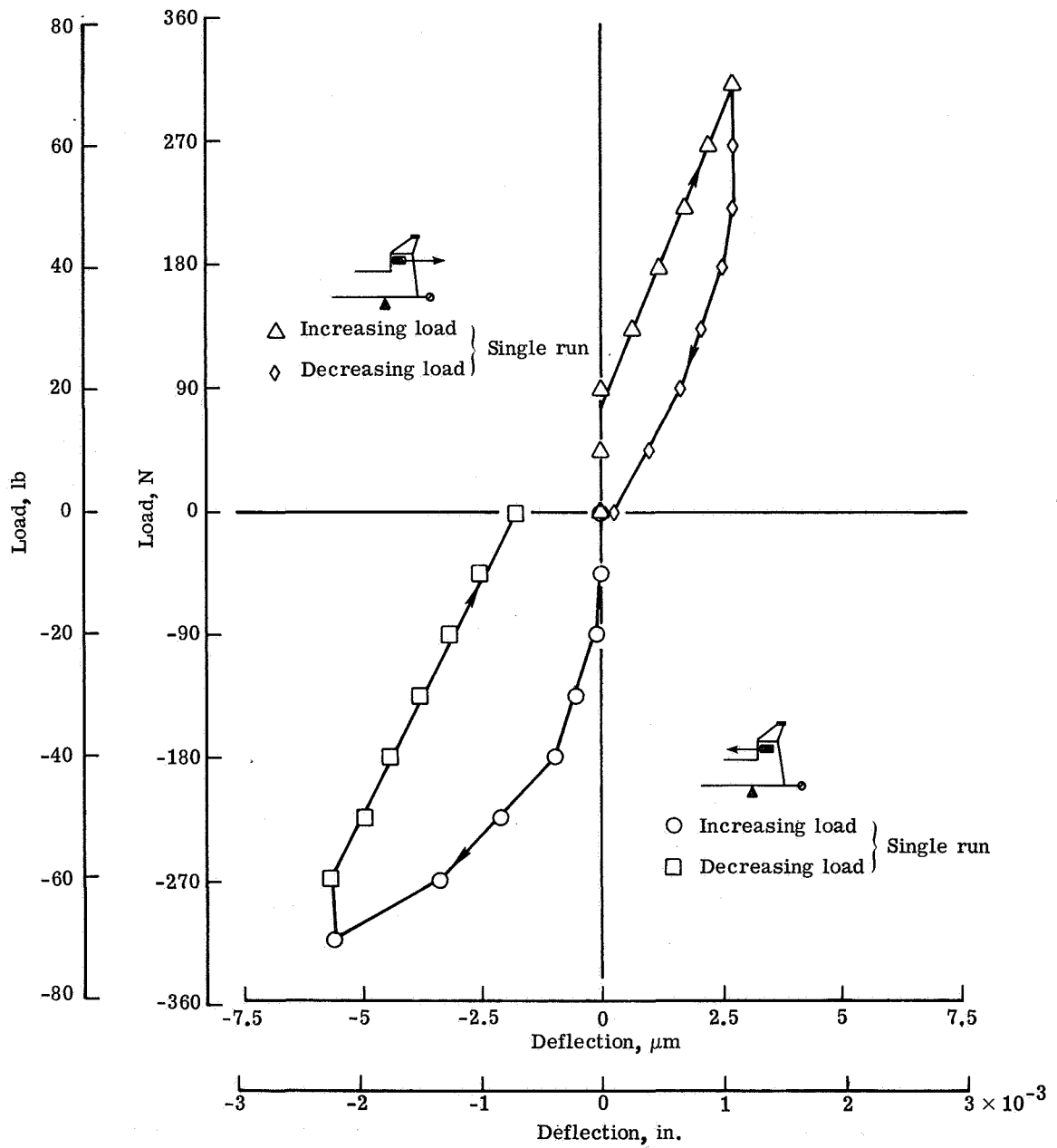
(c) Deflections at lower fuselage.

Figure 40.- Concluded.
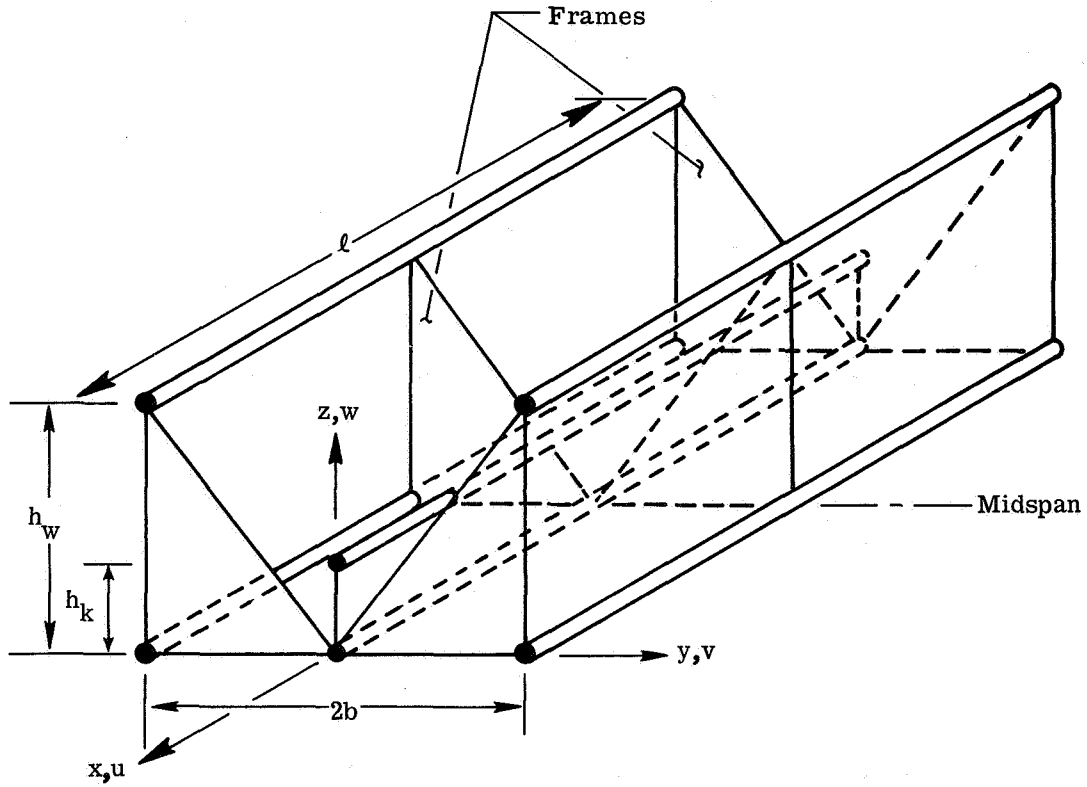
Figure 41.- Simplified fuselage model of appendix D.
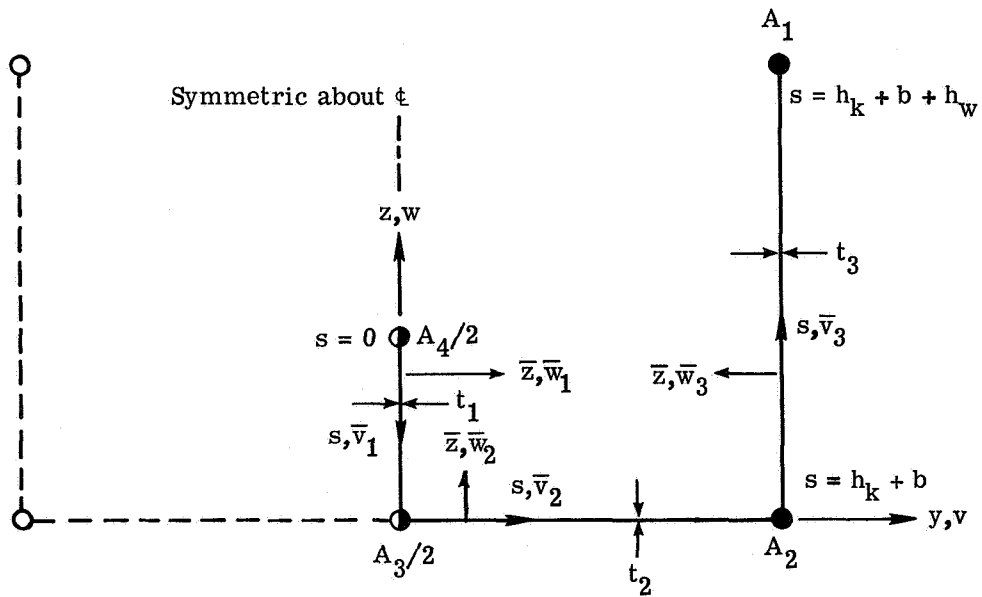
Figure 42.- Local cross-sectional coordinate system of appendix D.

(a) Coarse model.

(b) Refined model.
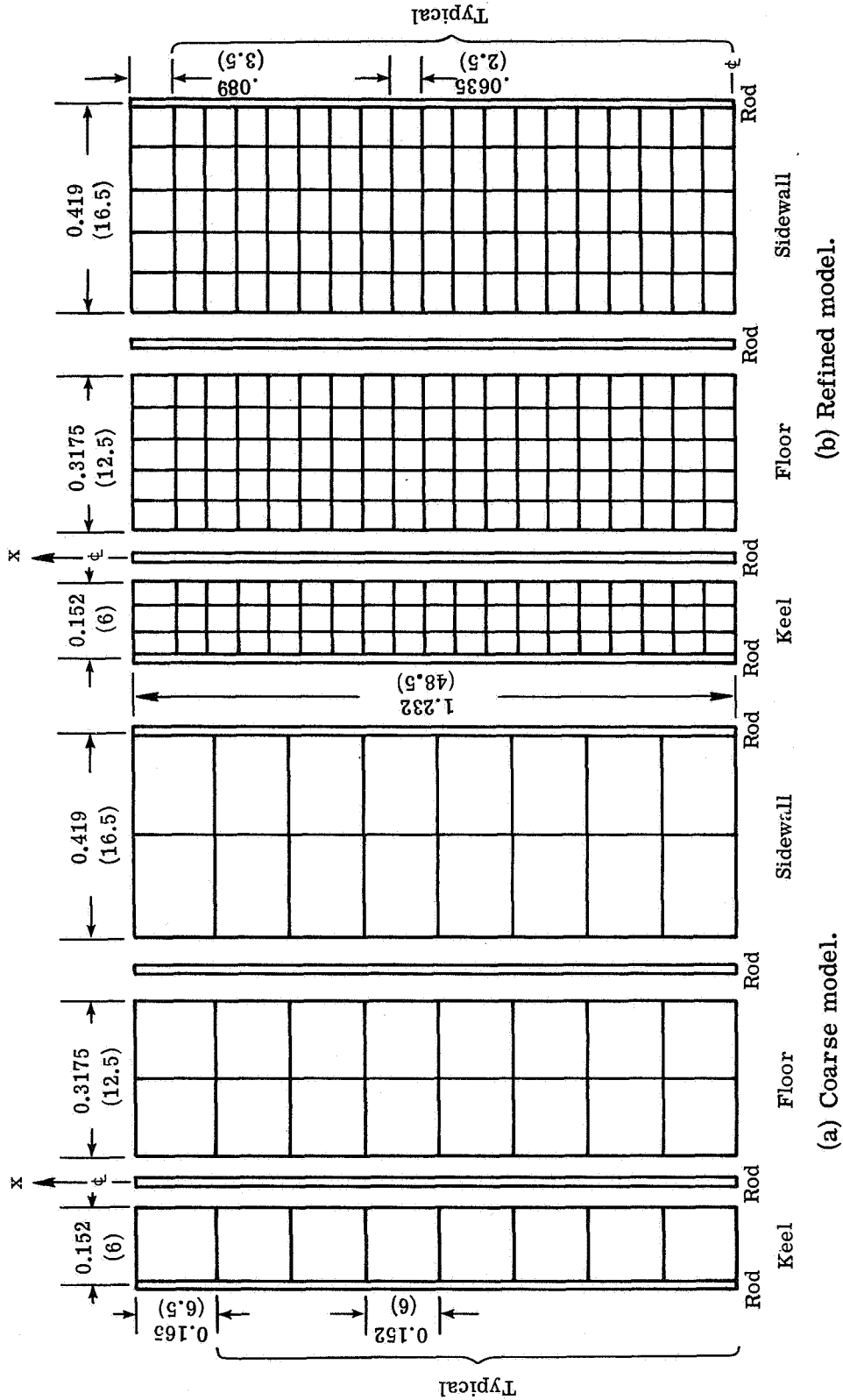
Figure 43.- NASTRAN models of simplified fuselage of appendix D. Dimensions are in m (in.).
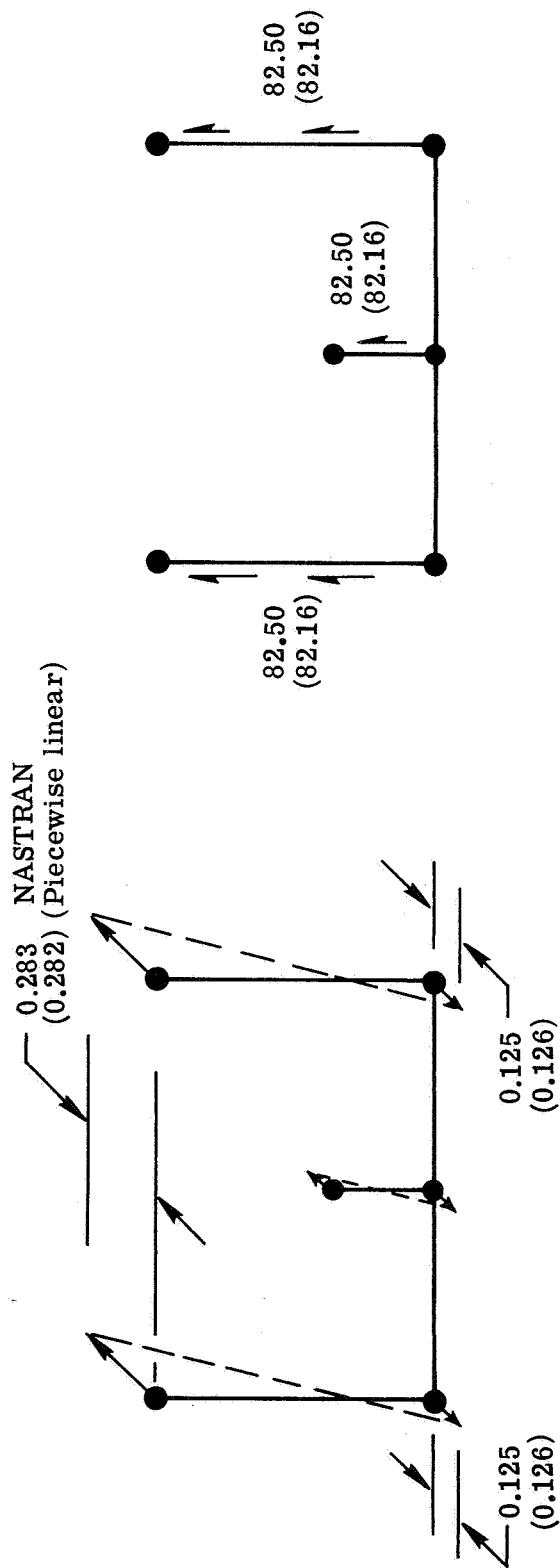
(a) Axial deflections at simple supports, normalized to maximum deflection.

(b) Shearing stresses at simple supports, normalized to maximum deflection, MN/m^2.

Figure 44.- First symmetric lateral bending mode for NASTRAN (piecewise linear) simplified fuselage of appendix D; f = 78.5 (77.8) Hz.
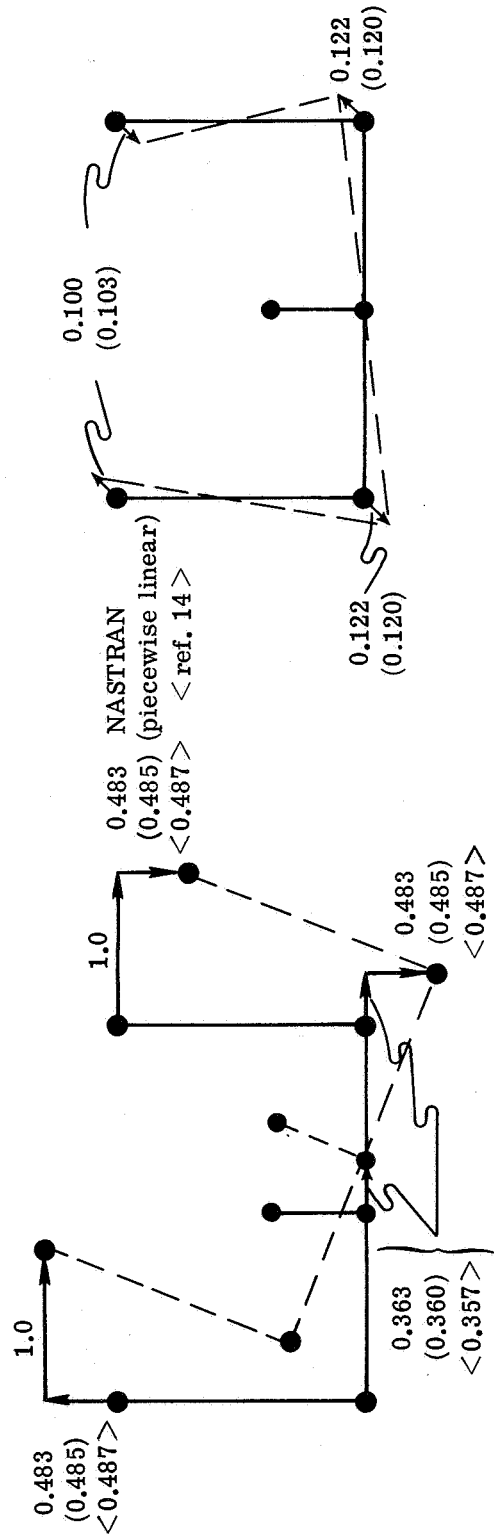
(a) Transverse and lateral deflections at midspan, normalized to maximum deflection.

(b) Axial deflections at simple supports, normalized to maximum deflection.
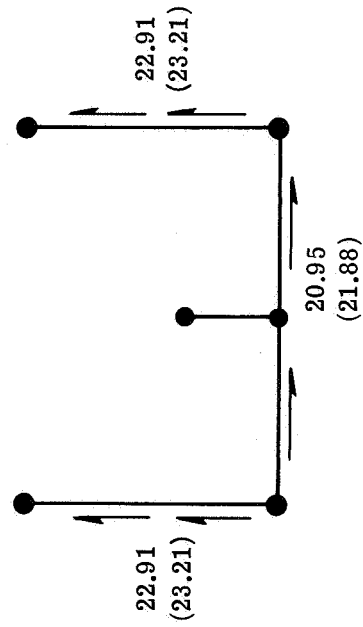
(c) Shearing stresses at simple supports, normalized to maximum deflection, MN/m^2.

Figure 45.- Axisymmetric torsional-transverse bending mode for NASTRAN (piecewise linear) ⟨ref. 14⟩ simplified fuselage of appendix D; f = 51.1 (51.8) ⟨53.1⟩ Hz.
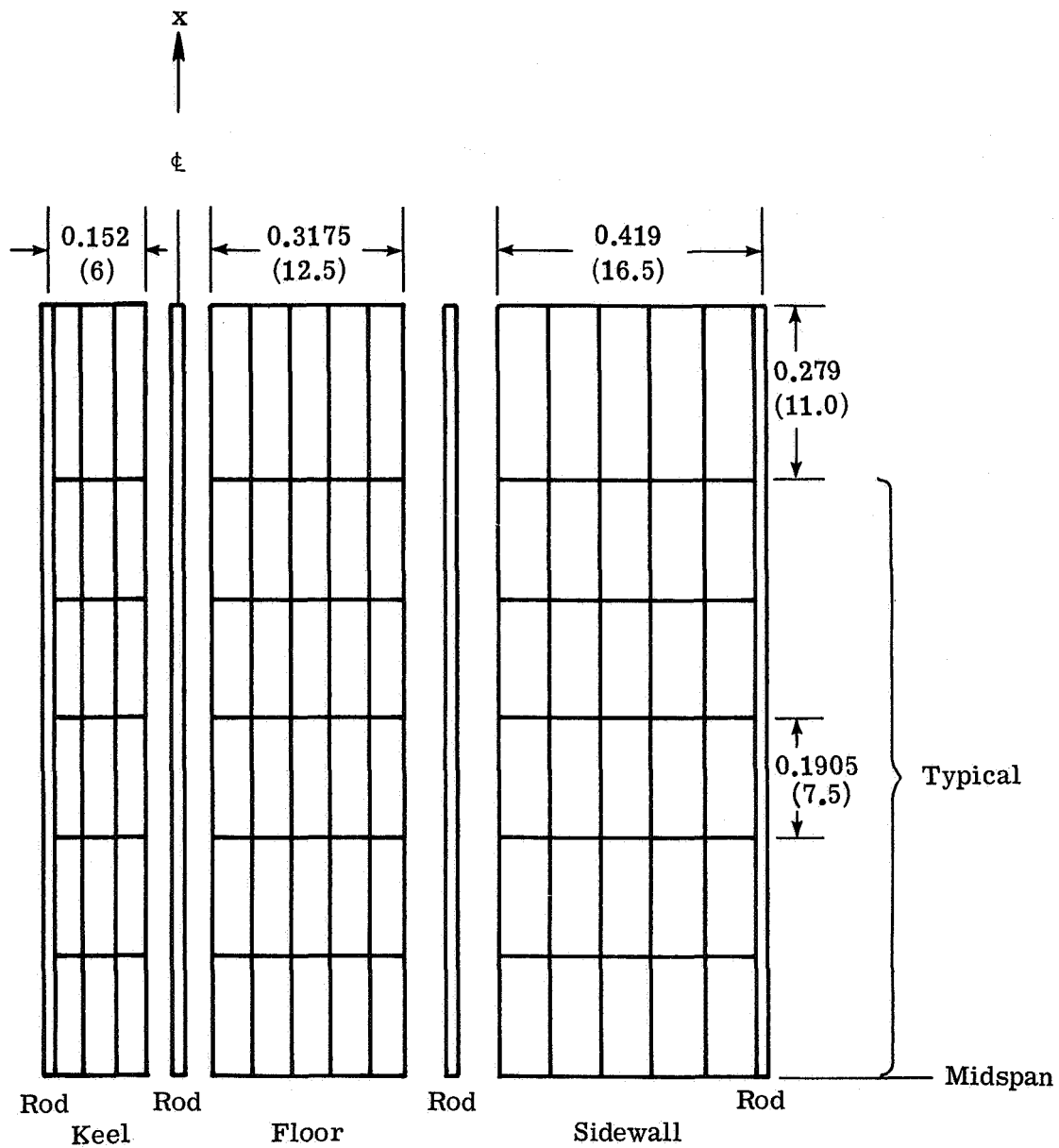
Figure 46.- NASTRAN simplified 1/4-model fuselage of appendix D with high-aspect-ratio QDMEM2 elements. Dimensions are in m (in.).
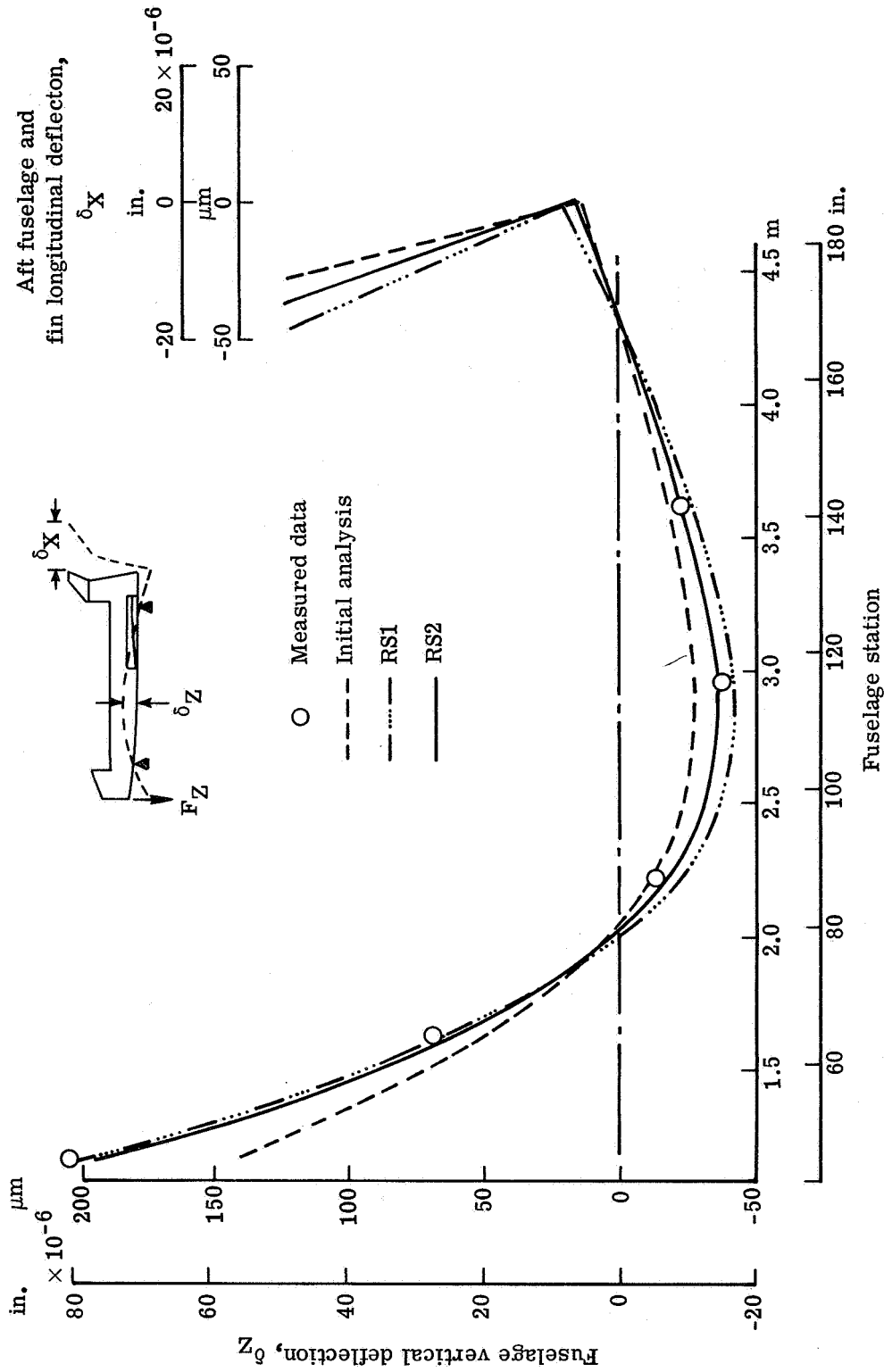
Figure 47.- Comparison of static measured and analytical deflections due to vertical loading at fuselage nose.
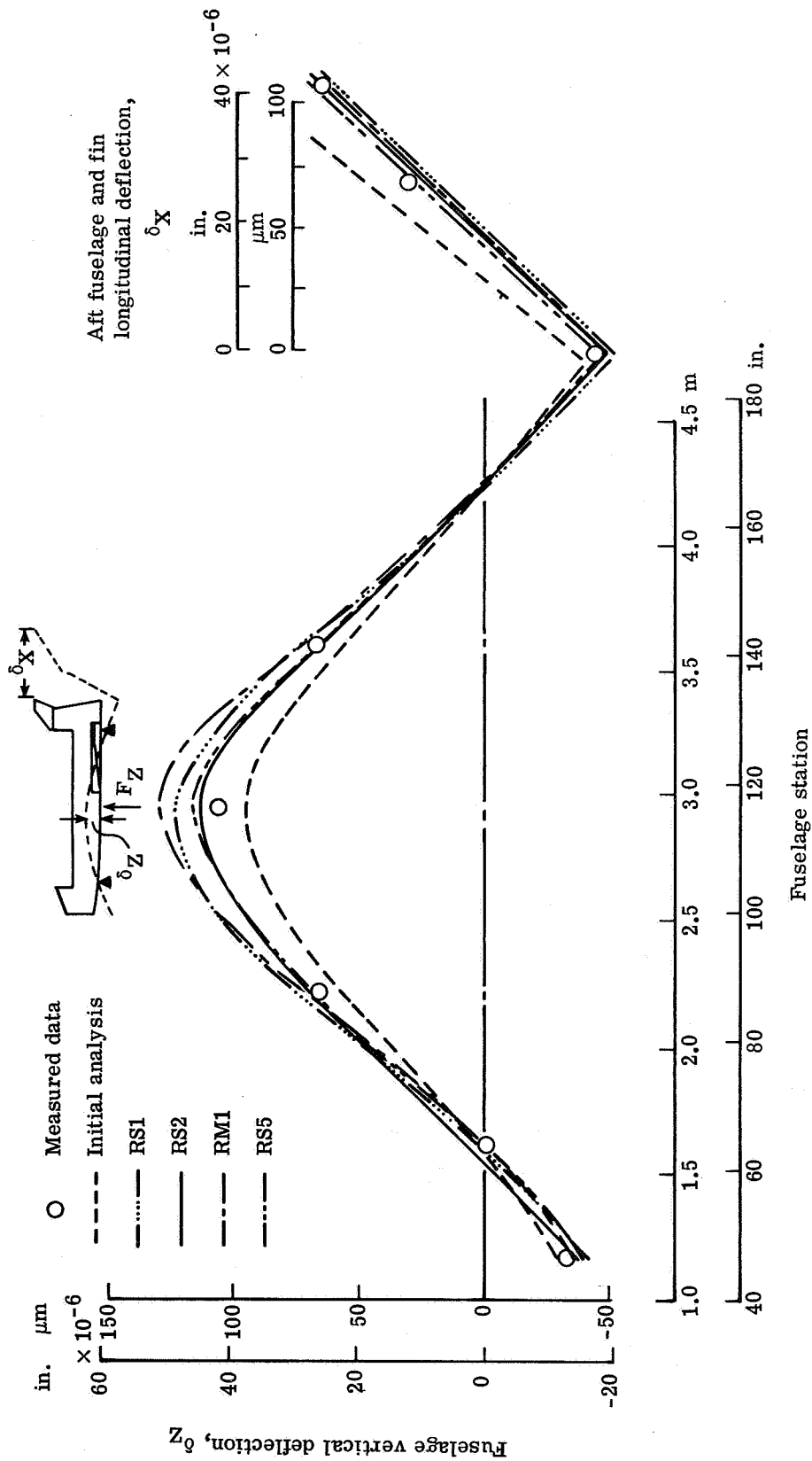
Figure 48.- Comparison of static measured and analytical deflections due to vertical loading at midfuselage.
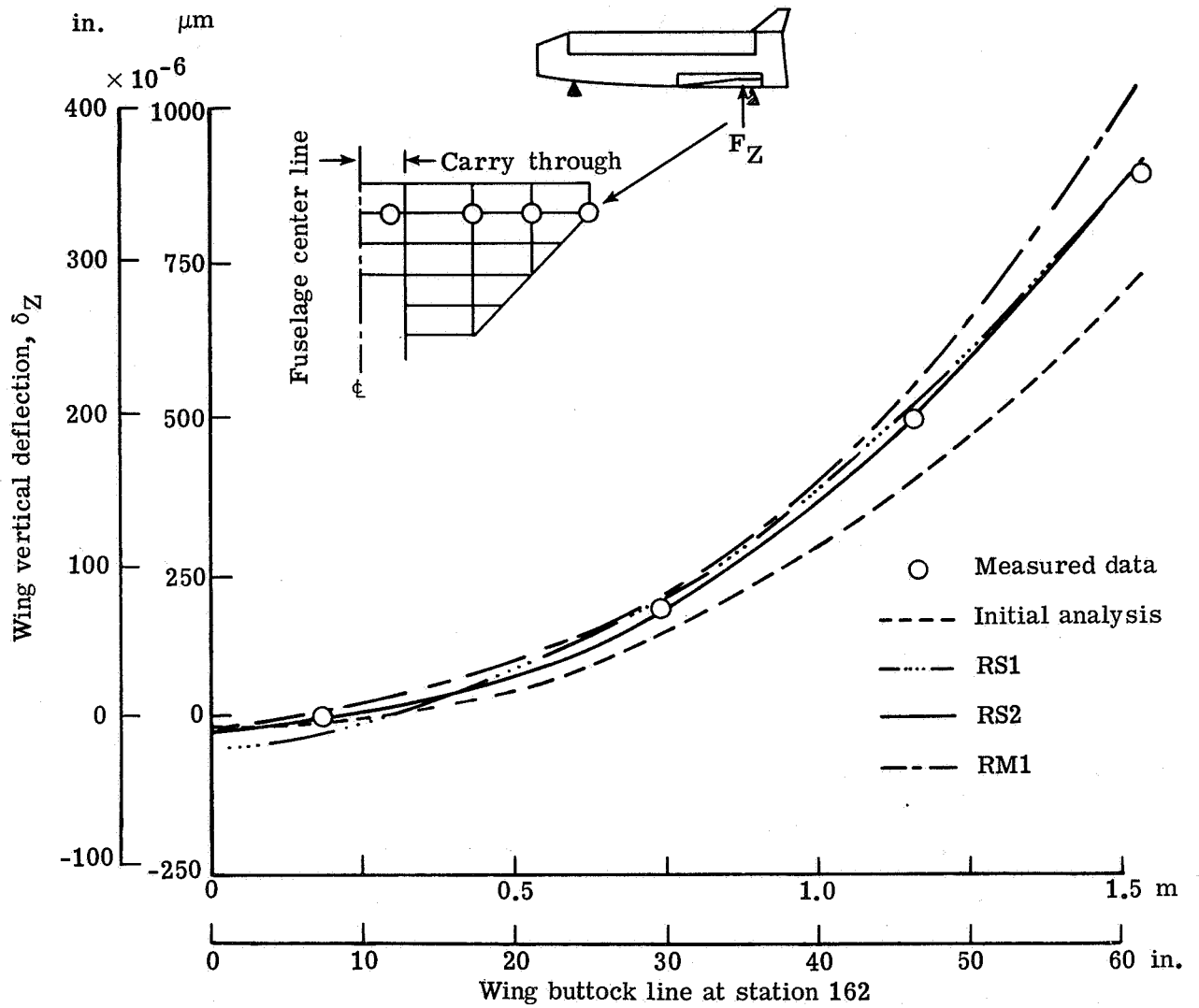
Figure 49.- Comparisons of static measured and analytical deflections for wing tip loading.
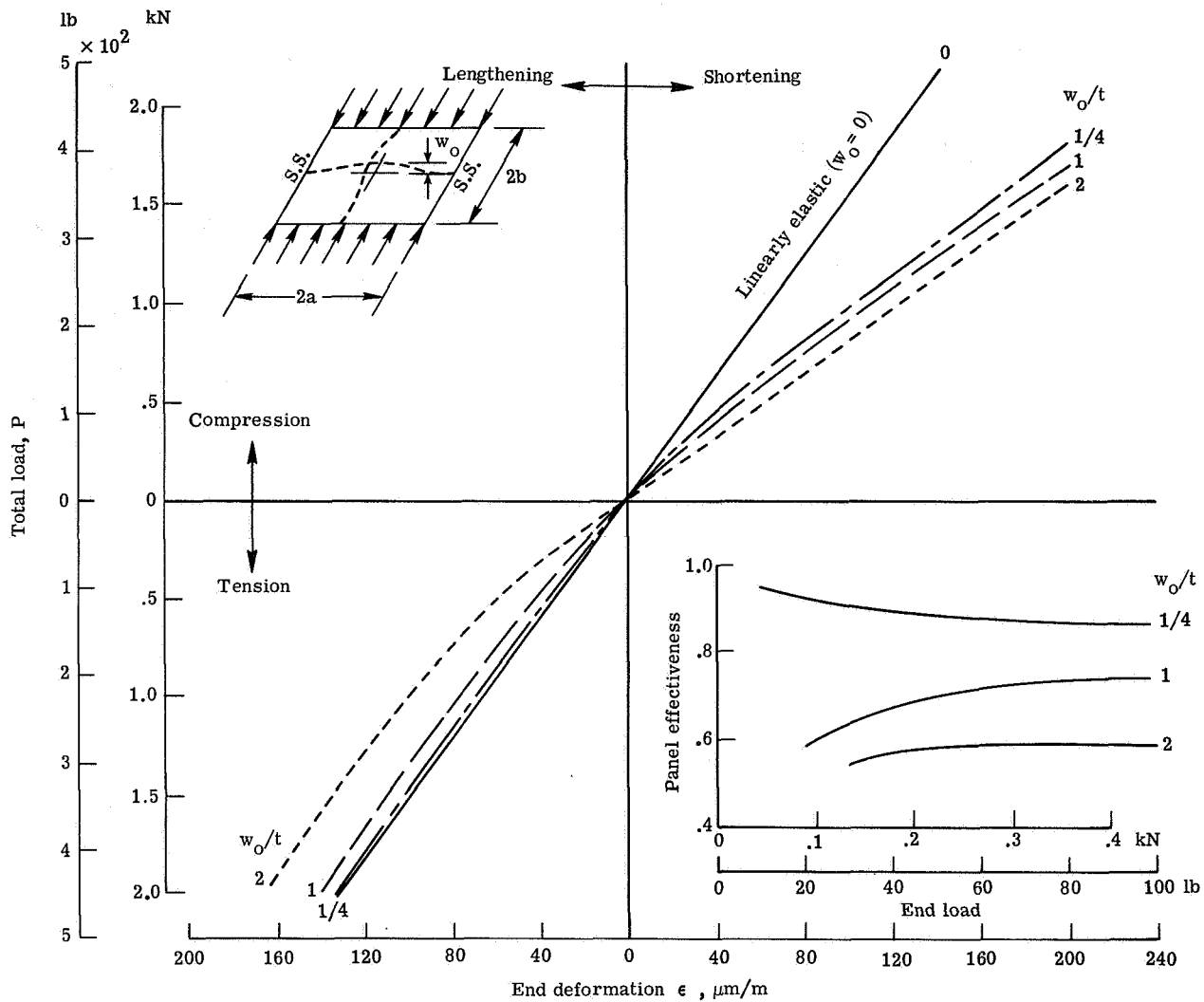
(a) Fuselage bottom surface; typical aspect ratio   a/b = 1.32;
t = 0.635 mm (0.025 in.).

Figure 50.- Analytical panel effectiveness estimates from reference 21, vol. II;
E = 68.95 GN/m^2; ν = 0.3.
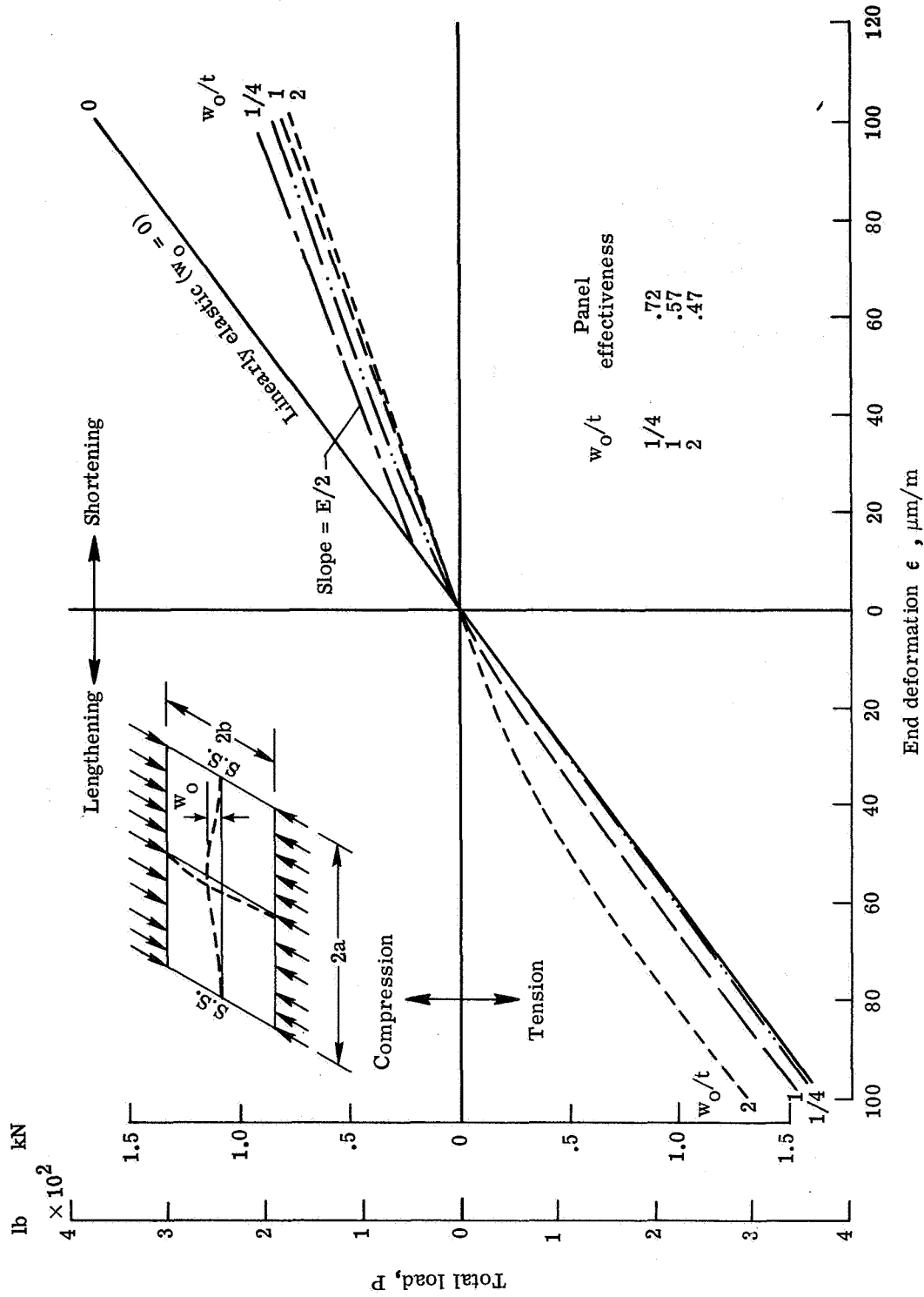
(b) Fuselage sidewall; typical aspect ratio a/b = 1.79; t = 0.635 mm (0.025 in.).

Figure 50.- Continued.
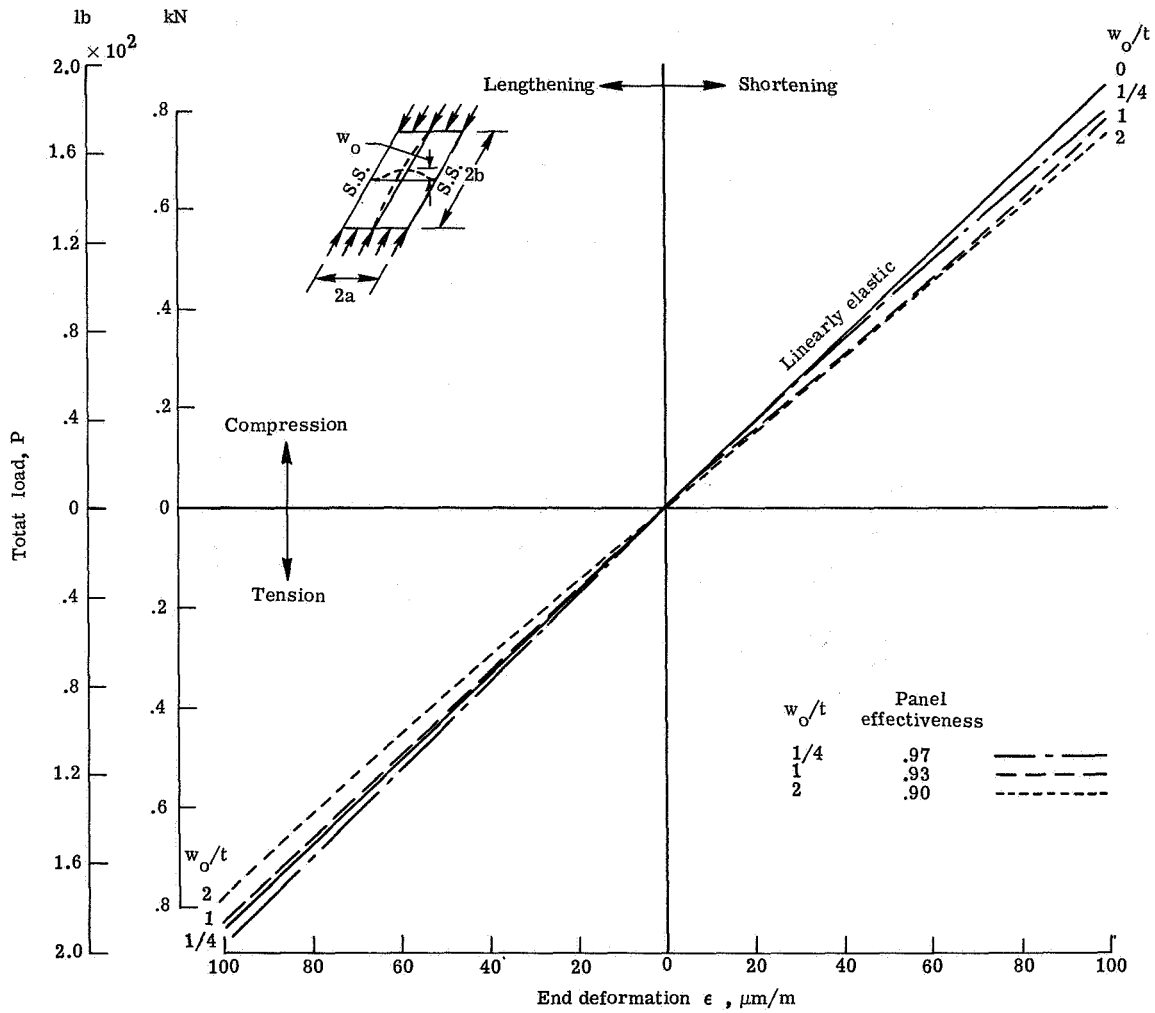
(c) Wing covers; typical aspect ratio a/b = 0.54;
t = 0.508 mm (0.020 in.).

Figure 50.- Concluded.

5.08 cm (2.00 in.)

38.1 cm (15.0 in.)

146.6 cm (57.7 in.)

0.51 mm (0.020 in.)
Aluminum panel

1.02 × 19 mm (0.040 × 0.75 in.)
Aluminum angle stiffeners

5 kg (0.0285 lb–sec^2/in.)
Tip mass

Backstop
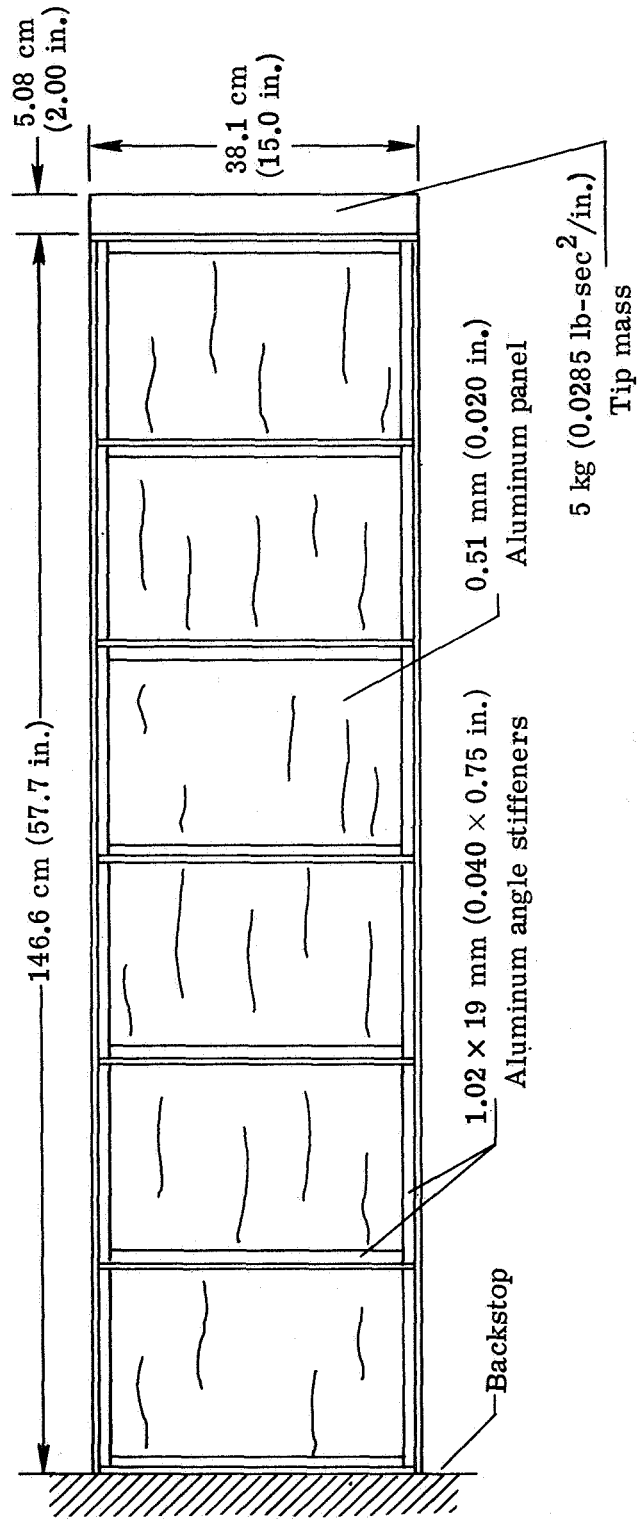
Figure 51.- Simplified panel model for panel effectiveness studies (appendix E).

(a) Flat panel.

(b) Panel deflection of 0.9 mm (0.035 in.).
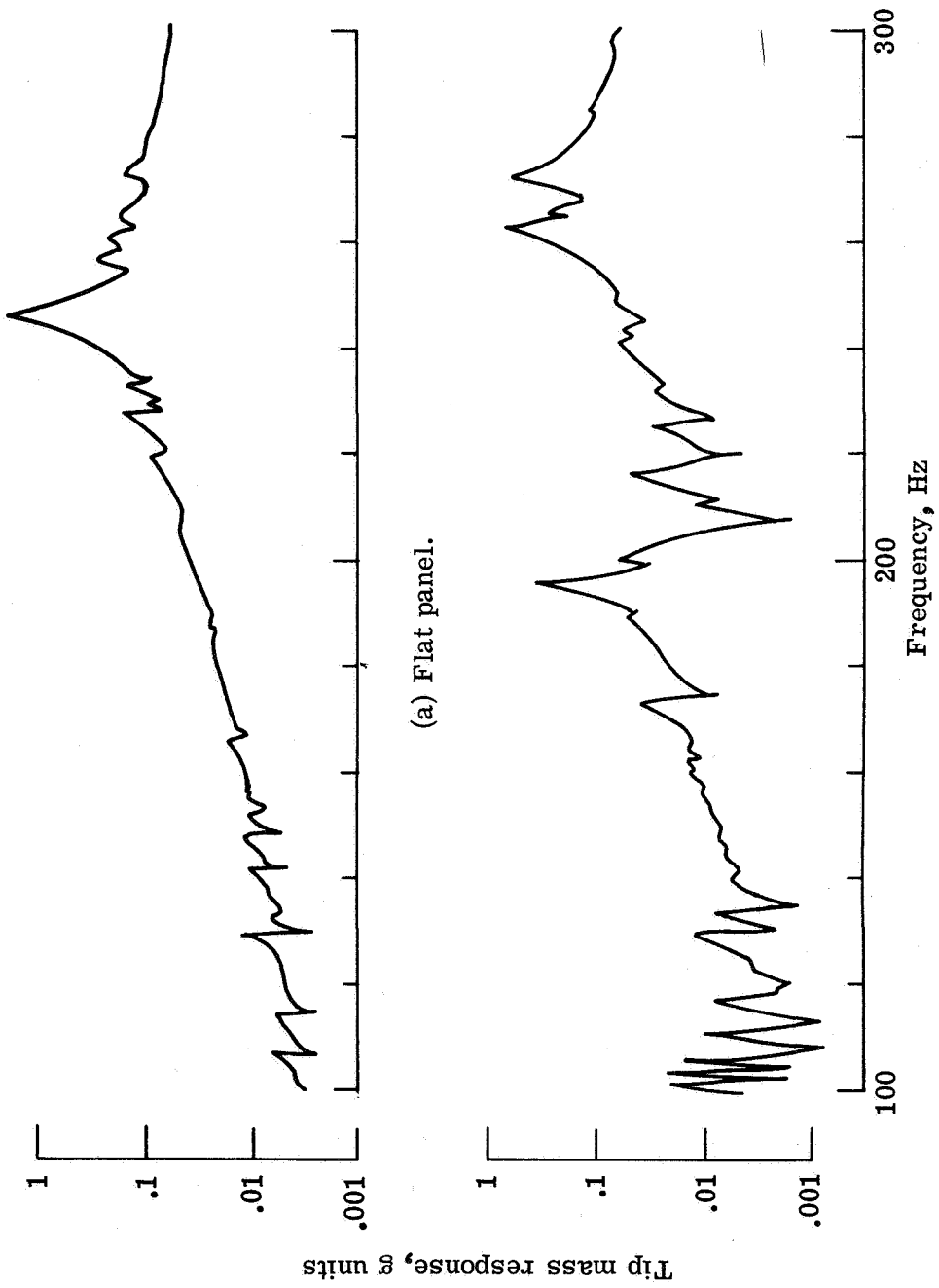
Figure 52.- Longitudinal response of tip mass as function of excitation frequency for various out-of-plane static panel deflections.

147
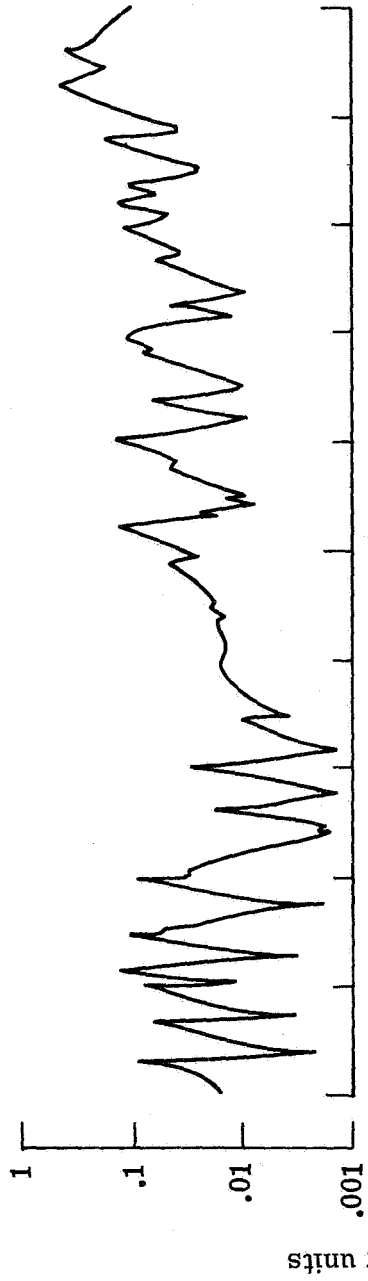
(c) Panel deflection of 1.4 mm (0.055 in.).

Frequency, Hz
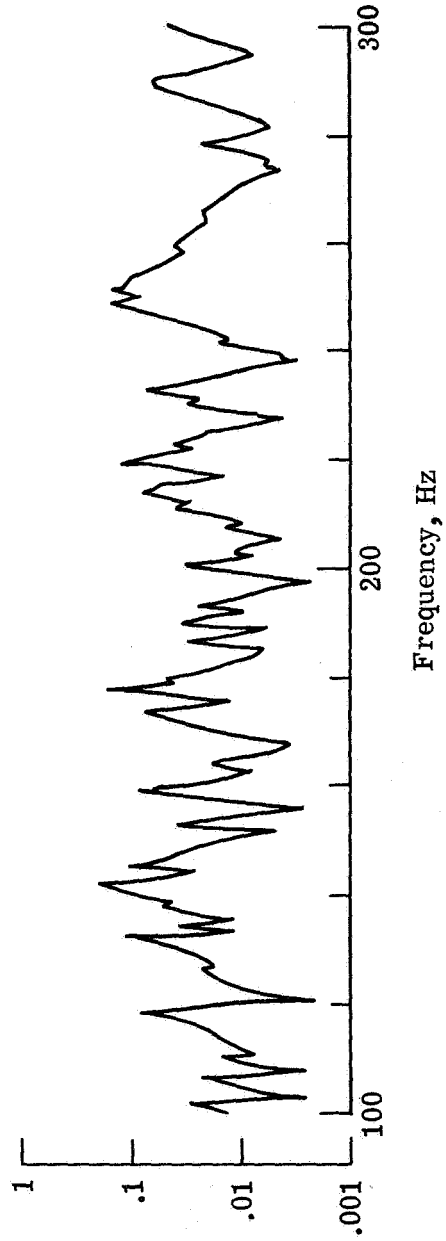
(d) Panel deflection of 1.8 mm (0.071 in.).

Figure 52.– Concluded.

"The aeronautical and space activities of the United States shall be conducted so as to contribute . . . to the expansion of human knowledge of phenomena in the atmosphere and space. The Administration shall provide for the widest practicable and appropriate dissemination of information concerning its activities and the results thereof."

—NATIONAL AERONAUTICS AND SPACE ACT OF 1958

NASA SCIENTIFIC AND TECHNICAL PUBLICATIONS

TECHNICAL REPORTS: Scientific and technical information considered important, complete, and a lasting contribution to existing knowledge.

TECHNICAL NOTES: Information less broad in scope but nevertheless of importance as a contribution to existing knowledge.

TECHNICAL MEMORANDUMS: Information receiving limited distribution because of preliminary data, security classification, or other reasons. Also includes conference proceedings with either limited or unlimited distribution.

CONTRACTOR REPORTS: Scientific and technical information generated under a NASA contract or grant and considered an important contribution to existing knowledge.

TECHNICAL TRANSLATIONS: Information published in a foreign language considered to merit NASA distribution in English.

SPECIAL PUBLICATIONS: Information derived from or of value to NASA activities. Publications include final reports of major projects, monographs, data compilations, handbooks, sourcebooks, and special bibliographies.

TECHNOLOGY UTILIZATION PUBLICATIONS: Information on technology used by NASA that may be of particular interest in commercial and other non-aerospace applications. Publications include Tech Briefs, Technology Utilization Reports and Technology Surveys.

Details on the availability of these publications may be obtained from:

SCIENTIFIC AND TECHNICAL INFORMATION OFFICE

NATIONAL AERONAUTICS AND SPACE ADMINISTRATION

Washington, D.C. 20546